The Effects of Excited States and Energetic Traps on Charge Transport in Disordered Organic Small Molecule Semiconductors.

Khademi, S.

The Effects of Excited States and Energetic Traps on Charge Transport in Disordered Organic Small Molecule Semiconductors

S. Khademi

School of Physics and Astronomy
Queen Mary, University of London

Supervisor – Dr. Theo Kreouzis
Prof William Gillin

May 2013

Submitted for the degree of Doctor of Philosophy

DECLARATION

I declare that all the work contained within this thesis is accomplished by myself during the course of my study at Queen Mary, University of London.

Shamim Khademi

ACKNOLEDGMENTS

This thesis would have been impossible without the support, encouragement and feedback of certain individuals whom have been instrumental throughout the course of my PhD studies. I'm indebted to my parents, Mr Fateh Khademi and Mrs Roya Khademi along with my sister Miss Sahar Khademi for their unfailing support and love specially at times of adverse difficulties. Their unshaken belief in my capacities has truly been a source of inspiration to me at every stage of my life. A few words of acknowledgment do not do justice to the impact that these individuals have had in my life. I wish I can replicate a fraction of care and loving kindness that they have showered upon me throughout the course of my studies in the UK. I would also like to sincerely thank my supervisors, Dr Theo Kreouzis and Prof William Gillin for their patience, support and feedback specially during the early stages of my PhD studies. Their humble attitude to learning and their desire and availability to support their fellow students at all times is truly something to admire. I felt so much at ease by having such individuals as my supervisors and I am very much looking forward to further increase our bonds of friendship in the future. I would also like to take this opportunity to mention my primary school mathematics teacher Mr Geoffrey Stewart without whom my love for science and mathematics would have been almost impossible. And finally I would also like to thank everyone else who have contributed and assisted me throughout my time at Queen Mary, from fellow PhD students to all those wonderful people in the condensed matter group whom are too many to mention. I dedicate this thesis to you!

ABSTRACT

Charge transport is the one the most fundamental concepts in organic semiconductors. The key quantity that characterises this transport behaviour is carrier mobility. The ability to transport carriers in a fast and unimpeded nature in organic devices such as Organic Photovoltaics (OPV) or Organic Light Emitting Diodes (OLED) is a key parameter for building more efficient devices. Significant steps have so far been taken to understand and model this phenomenon, however there are still many questions that need to be answered. One such fundamental question is the role of excited states on the charge transport properties of organic materials which historically has been ignored. This thesis aims to investigate the transport properties of two of the most widely used organic materials, N,N′-bis-[(1-naphthyl)-N,N′-diphenyl]-1,1′-biphenyl)-4,4′-diamine (NPB) and are N,N'-diphenyl-N,N'-bis 3-methylphenyl-1,1'-biphenyl-4,4'-diamine (TPD). We demonstrate how excitons are generated in a single organic layer OLED devices and how traditionally hole transport materials are capable of fast long range electron transport. We provide a comprehensive analysis of the charge transport properties of both materials with respect to the Gaussian Disorder Model (GDM) and demonstrate how both types of carriers can easily be transported in these materials. We then investigate the effects of exciton generation on the transport properties of the materials and propose some numerical modeling to analyse the effects of such excited states and the distribution of energetic traps in our system. We show that the swing of carrier mobility in either direction depends on the interplay and dominance of each mechanism (triplet/carrier interaction and trap filling). We also investigate the effects of

removing excited states from our device by deliberately introducing impurities via doping of a phosphorescent molecule to alter their concentration. Finally we propose some future direction that one can take to model charge transport behaviour in disordered organics based on the experimental work discussed in thesis.

Table of Contents

List of Figures

Bibliography

List of publications

1. S. Khademi, J. Y. Song, P. B. Wyatt, T Kreouzis, W. P. Gillin, *Ambipolar charge transport in "traditional" organic hole transport layers*, Advanced Materials, **2012**, 24, 2278-2283

2. The role of excited states and trap filling on modeling charge transport in organic disordered semiconductors *(in preparation)*

3. Phosphorescent effects on charge transport properties of organics *(in preparation)*

1.0 Introduction to Organic Semiconductors

Before discussing the concept of charge transport, it is important to take a step back and consider some of the fundamental properties associated with organic semiconductors. These materials refer to the class of semiconductors consisting of mainly carbon and hydrogen arranged in a conjugated bond structure. They possess properties associated with a semiconductor such as light absorption, light emission and conduction of charges. For example through the dissociation of a photo-excited electron-hole (e-h) pair or injection from electrodes.

A significant advancement in this field was reached with the development of Organic Light Emitting Diodes (OLED) based on anthracene crystals, first developed in the early 1960s[1]. However, their main drawback was the large operating voltages required to produce luminescence, usually a few hundred volts. It took approximately another 20 years to solve this problem when Tang and VanSlyke managed to create OLED devices by using sublimed small molecule double layer thin-film structures[2]. With this approach electrons and holes were injected into the respective electron/hole transport materials which would then recombine at the interface and decay radiatively to produce luminescence (see section 1.4 for further details). Since then interest in this area has grown considerably with extensive research carried out at the charge transport level to improve the efficiencies of these devices.

Another rapidly growing area is the development of Organic Photovoltaic cells (OPV). Just as with OLED devices, the first major breakthrough was made by Tang and co-workers through the use of a double layer thin film device concept[3], with reported efficiencies of around 1%[4]. Since then many steps have been taken to improve the efficiencies of OPVs both by optimizing the original Tang structure (for example Ref [5]) and by developing new approaches such as polymer/polymer blends[6], polymer/small molecule blends[7], organic/inorganic (hybrid) structures such as polymer/quantum dot structures[8] and dye synthesized cells[9]. The current benchmark efficiency lie around 5-6% with the use of P3HT and PCBM blends[10].

Organic Field Effective transistors (OFET) are also another rapidly growing field that has gained considerable interest in recent years. Today, the performance of such devices shows a promising future for OFET. Mobility values are around 0.1cm^2/Vs for polymer based FETs[11] while the best results are in the range of 1cm^2/Vs using pentacene molecules[12-13].

1.1 Organic Materials and Charge Transport

1.1.1 Small Molecules and Fullerenes

In general, organic semiconductors can be categorized into two classes, low molecular weight materials (small molecules), and polymers. One of the main differences between them is the way in which they are processed. Polymers are soluble and can be prepared by solution processing methods such as spin coating[14], whilst small molecules on the other hand can be

insoluble and are predominantly processed via vacuum sublimation. This section provides a selection of some of the widely used small molecules and fullerenes in organic structures. It discusses some of their physical/molecular properties and a comparison is provided between them and organic polymers in section 1.1.2.

The energy level diagrams in figure 1 define some of the electronic structure parameters relevant to designing organic materials for OLEDs and OPVs.

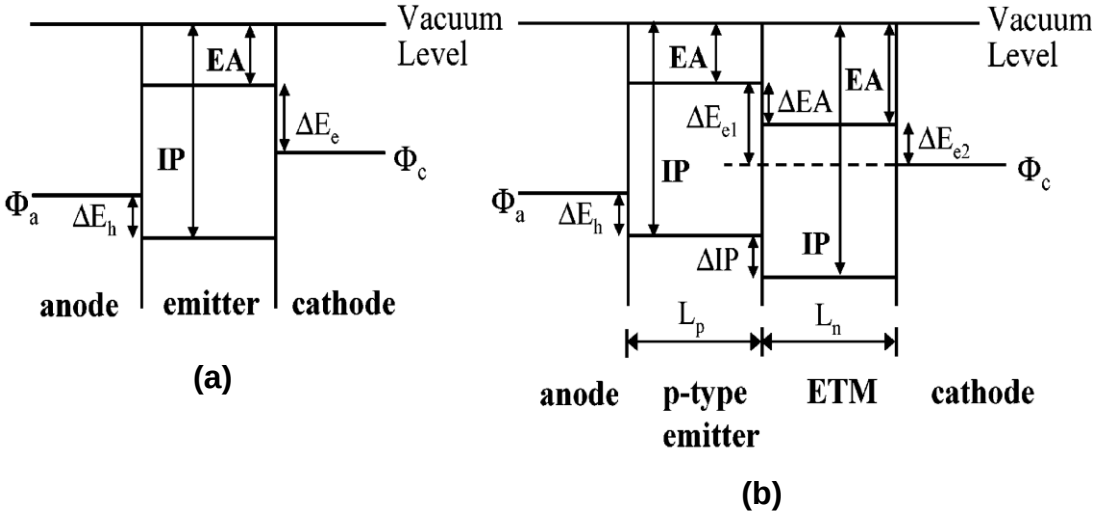

Figure 1. Generic representation of energy levels in OLEDs for (a) single devices and (b) double layers structures.

In a single layer OLED (Figure 1a), the electron affinity (EA) or lowest unoccupied molecular orbital (LUMO) level and the ionization potential (IP) or highest occupied molecular orbital (HOMO) level relative to the cathode work function (Φ_c) and the anode work function (Φ_a), respectively, determine the charge injection into the diode. Large mismatches, thus large barriers for hole injection at the anode $\Delta E_h = (IP - \Phi_a)$ and electron injection at the cathode

$\Delta E_e = (\Phi_c - EA)$, lead to poor OLED performances. For the commonly used indium tin oxide (ITO) anodes (Φ_a = 4.7- 4.8 eV) and cathodes such as aluminum (Φ_c = 4.3 eV), most emissive organic materials have some barrier for hole injection and a particularly large barrier for electron injection as exemplified by N,N'-diphenyl-N,N'-bis 3-methylphenyl-1,1'-biphenyl-4,4'-diamine (TPD)[15] and N,N′-bis-[(1-naphthyl)-N,N′-diphenyl]-1,1′-biphenyl)-4,4′-diamine (NPB)[16] with energy band gaps of 3.05eV and 3eV respectively.

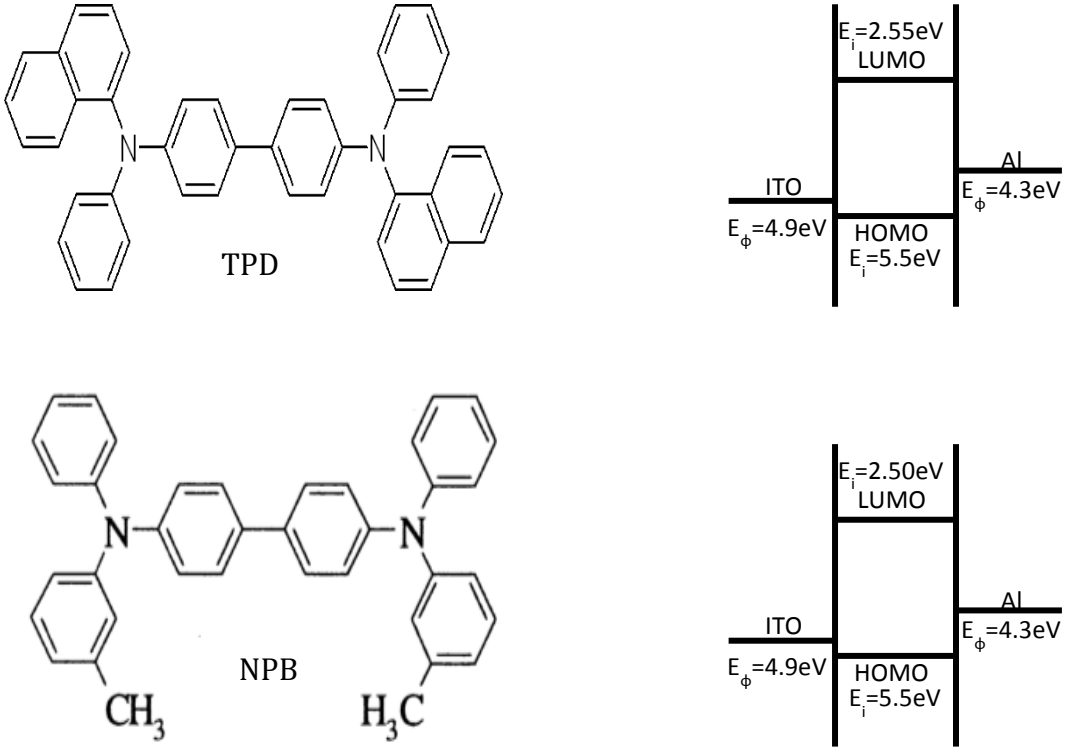

Figure 2. Chemical structures of two of the most studied organic molecular semiconductors studies in this thesis along with their corresponding energy levels and typical electrode work functions, (a) TPD and (b) NPB.

Both materials are extensively used throughout this thesis and are also popular in many OLED structures. They are typically categorized as

disordered hole transport materials (HTM) due to their lack of distinct lattice constants. Their HOMO layers are closely matched to that of PEDOT-PSS hole injection layer electrodes used in OLEDs. Thus making them suitable materials for hole injection and transport. Typical hole mobility in TPD and NPB range between 10^{-4}-10^{-3} $cm^2V^{-1}s^{-1}$.

The introduction of one or more layers of charge transport materials in addition to the emitter layer provides a powerful means to controlling charge injection, transport, and recombination in OLEDs. The presence of an electron transport material (ETM) layer in the two layer OLED configuration based on a p-type emitter not only lowers the barrier for electron injection ($\Delta E_{e2} < \Delta E_{e1}$) but also serves to block holes since the IPs of ETMs are generally large ($\Delta_{IP} > 0$). Similarly an HTM in combination with an n-type emitter such as aluminum quinolate (Alq_3)[17] or polyquinoline[17], can significantly improve OLED performance; in this case, the HTM facilitates hole injection and blocks electrons. Most experiments of charge transport in disordered organics deal with mobility of holes. Data for electron mobility is extremely rare and where exists, very low mobility values are reported[18]. The apparent reason for this low mobility is charge trapping. A high effort is needed to purify organic solids since oxidation predominantly produces electron traps and a relatively smaller concentration of hole traps[18]. However electron transporter such as Alq_3 have gained considerable interest as it is currently one of the few electron transporters that are used extensively is OLEDs. Typical electron mobility values are very similar to TPD and NPB, mainly in the range of 10^{-4}-10^{3} $cm^2V^{-1}s^{-1}$.

Amongst other types of small molecule structures are the oligoacene group. They are predominantly crystalline materials with specified lattice constants consisting of fused benzene rings. Among popular oligoacenes are pentacene[19], TIPS-pentacene[20] and rubrene[21]. These are typically used as HTMs and exhibit much larger mobility values compared to disordered organics such as TPD and NPB. For example recent developments of pentacene have shown mobility values in excess of 5 $cm^2V^{-1}s^{-1}$. Such relatively high mobilities are achieved by having π-conjugated molecules crystallize in a layer of herringbone packing. Such packing gives rise to efficient 2D transport within the stacked organic layer.

Fullerene doped organic semiconductors and their derivatives such as C_{60}[22] and methanofullerene Phenyl-C61- Butyric-Acid-Methyl-Ester (PCBM)[23] have also gained increased popularity in recent years. They have been particularly popular in bulk hetrojunction (BHJ) solar cell technologies. PCBM in particular have gained considerable interest due to its solubility and hence its effectiveness to blend with p-type polymer based semiconductors. They have properties such as fast electron transfer, a low dielectric constant comparable to the organic polymer and high mobilities. Soluble forms of fullerenes such as methanofullerene and PCBM have electron mobilities in the range of (10^{-3} to 0.2 cm^2 Vs^{-1})[23] and show generally n-type semiconductor properties.

1.1.2 Polymers

Organic polymer thin film layers are also very popular in many semiconductor structures. Apart from preparation techniques organic polymers also possess similar properties as small molecules, for example they too can occur as crystalline ordered materials with specified lattice constants, or as amorphous morphologies with energetic sites determined by a specific probability distribution. Another common theme between them is their ability to form π-conjugating structures with alternating C-C single and double bonds (see section 1.2). Some of the most widely used organic polymers are poly(3-hexylthiophene-2,5-diyl) (P3HT)[24], poly[bis(4-phenyl)(2,4,6-trimethylphenyl)amine] (PTAA)[25] and polyfluorene (PFO)[26]. They possess hole mobility values in the range of 10^{-4}-$10^{-3}$$cm^2V^{-1}$ and typically exhibit non-dispersive transport properties at room temperature. Poly[(9,9-di-n-octylfluorenyl-2,7-diyl)-alt-(benzo[2,1,3]thiadiazol-4,8-diyl)] (F8BT)[27] and superyellow[28] are also two other common polymers used in OLED structures. In the case of F8TB it possess similar electron and hole mobilities (10^{-4}-$10^{-3}$$cm^2V^{-1}$).

Spin-coating is the preferred fabrication technique for polymer thin films since it can be done at room temperature and creates films of the required thickness range (typically 100nm). Polymers often decompose when heated, thus thermal vacuum evaporation is often not an option for growth. Also, spin coating can produce very thin films, such as those needed for OLEDs. The procedure can't be used to create thicker films (greater than thousands of Angstroms), but rarely are such thick films used in OLEDs. Another

advantage of spin coating is the ability to fabricate devices on flexible plastic substrates such as polyethylene terephthalate (PET). Such materials may not be suitable for comparable devices based on small molecules due to the need for high temperature fabrication procedures involved. A disadvantage of the spin coating technique however is its inability of patterning. Spin coating creates a large plane of only one emitting polymer. Pixels can be created by patterning the cathode, however all pixels will be the same colour. Another disadvantage is that the process has very little control over thickness precision. Material thickness is only determined after device fabrication and not during material deposition. Nevertheless, spin coating is commonly used in the research field due to their robust ease of production.

Sometimes it can be advantageous to tailor the wavelength of an OLED while using the same emitting polymer. Modifications are possible since the band gap energy of the emitting layer can be radically changed by varying the morphology of the polymer thin film. The length of conjugated segments is the length along the backbone of connected, resonating π^* electron orbitals. If this length is shorter than the conjugation length (the excited state delocalization length) of the fully extended polymer chain (typically > 100 repeat units), the oligomer will have a higher energy band gap and thus a photon of shorter wavelength will be emitted when the electron recombines with a hole. The length of conjugated segments can either be the physical length of a planar polymer chain or planar oligomer, or the length of uninterrupted conjugation between twists and defects in a non-planar polymer chain or long oligomer. For PPP-like polymers (see section 1.6.3 for further details), the conjugation length is approximately 10-15 phenyl groups. Thus, if

the molecule length is greater than 15 phenyl groups, then the emitted photon will have the same wavelength for any fluctuation in molecular weight. However, if the polymer length is less than 10 phenyl groups, the wavelength of the emitted photon will vary depending on the length of the polymer backbone.

1.2 Formation of Ring Type Structures

Semiconductor organic materials typically consist of alternating carbon double and single bonds. The double bonds are responsible for pi (π) bonding within the molecule and occur as a result of the overlap of the wave functions of p orbitals in carbon. This produces carrier delocalization across the entire molecule and leads to the semiconducting properties experienced in organic solids. This process is shown in figure 3.

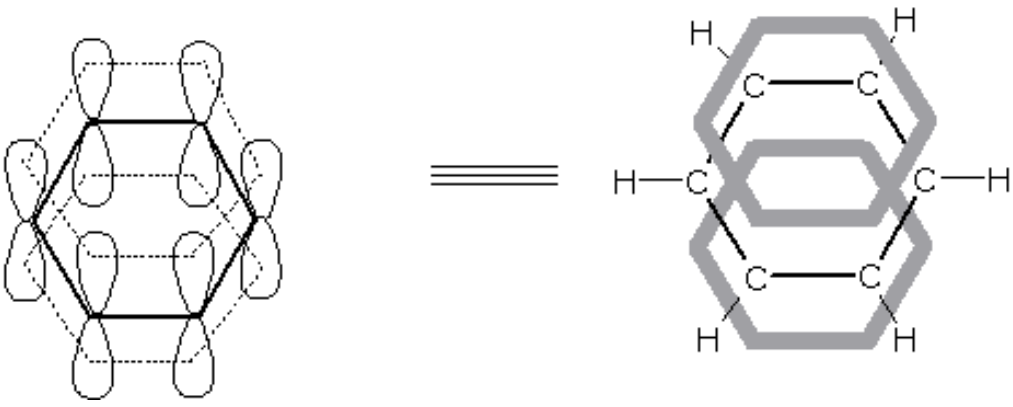

Figure 3. A schematic showing the formation of the Higher Occupied Molecular Orbital (HOMO) and the Lower Unoccupied Molecular Orbital (LUMO) of Benzene.

The structure consists of 6 carbon atoms, each with an atomic configuration of $1s^2 2s^2 2p_x^1 2p_y^1$. In order to form a ring type structure each carbon atom must bond to 3 other atoms (2 carbon and 1 hydrogen). Thus through the process of hybridization and promotion of an electron from the $2s^2$ to $2p_z$, the atomic configuration becomes $1s^2 2s^1 2p_x^1 2p_y^1 2p_z^1$. Such a configuration will now allow each of the sp^2 hybrid orbitals ($2s^1 2p_x^1 2p_y^1$) to form sigma (σ) bonds with two other carbon atoms and a hydrogen atom. The remaining p_z^1 orbitals will be arranged perpendicular to the newly formed sigma bonds. Hence this will result in an overlap of each of the p_z orbitals in carbon with its immediate neighbors resulting in the formation of pi (π) bonding, spread over the entire carbon ring. Thus the electrons are no longer held between just two carbon atoms, but are said to be delocalized i.e. spread across the entire ring.

1.3 Basic Properties of Organic Semiconductors

The properties of organic semiconductors can best be understood in terms of organic molecular crystals and their comparison with the properties of inorganic semiconductors. In inorganic semiconductors strong covalent bonding between the atoms leads to the formation of very wide conduction and valence bands, usually in range of several electronvolts (eV). Transitions between these bands control optical absorption. Strong electronic coupling between adjacent atoms also ensures a high degree of carrier mobility typically of the order of 10^3 cm^2/Vs. On the other hand in crystalline organic semiconductors strong chemical bonding is confined to the molecular level

only, whilst intermolecular coupling is governed by weak Van der Waals forces. The result is the formation of narrow molecular orbitals, usually a few tenth of an eV wide[29]. Carrier mobility is also low compared to inorganic semiconductors as a direct result of weak intermolecular coupling. Typical mobility values range between 0.1-20 cm^2/Vs[30] although for disordered materials it is significantly lower, around 10^{-4} to 10^{-3} cm^2/Vs[31].

Another important property of organic semiconductors is their ability to generate Frenkel type excited states. Due to their low dielectric constant (~2 to 4), once excited states are created, they tend to have a very high binding energy (~0.5eV)[32] resulting in a small coulomb capture radius (~0.1nm). This means that excited states are usually confined to individual molecules and require an additional energy to fully dissociate. In comparison inorganic semiconductors tend to exhibit dielectric constants values of greater than 10, which means that once an electron is excited to the conduction band it's effectively a free charge carrier. It is only at very low temperatures when Wannier type excitations are observed. However, even in these cases the binding energy is much weaker (~10meV) and hence the e-h capture radius is much larger than organic materials, typically greater than 10nm.

1.4 Polarons, Bi-polarons and Frenkel Type Excitons

Polarons and bipolarons are associated with the process of addition and removal of electrons from molecules or a chain of molecules. In an organic polymer chain, it is usually energetically favorable to localize the charge that appears on the chain and to have, around the charge, a local

distortion (relaxation) of the lattice. This process causes the presence of localized electronic states in the gap due to a local upward shift $\Delta\varepsilon$ of the HOMO and downward shift of the LUMO (see figure 4b). Considering the case of oxidation, i.e. the removal of an electron from the chain, we lower the ionization energy by an amount $\Delta\varepsilon$. If $\Delta\varepsilon$ is larger than the energy E_{dis} (distortion energy) necessary to distort the lattice locally around the charge, this charge localization process is favorable relative to the band process where delocalization occurs across the entire molecular structure. We then obtain the formation of what is called a polaron. In chemical terminology, the polaron is just a radical ion (spin ½) associated with a lattice distortion and the presence of localized electronic states in the gap referred to as polaronic states.

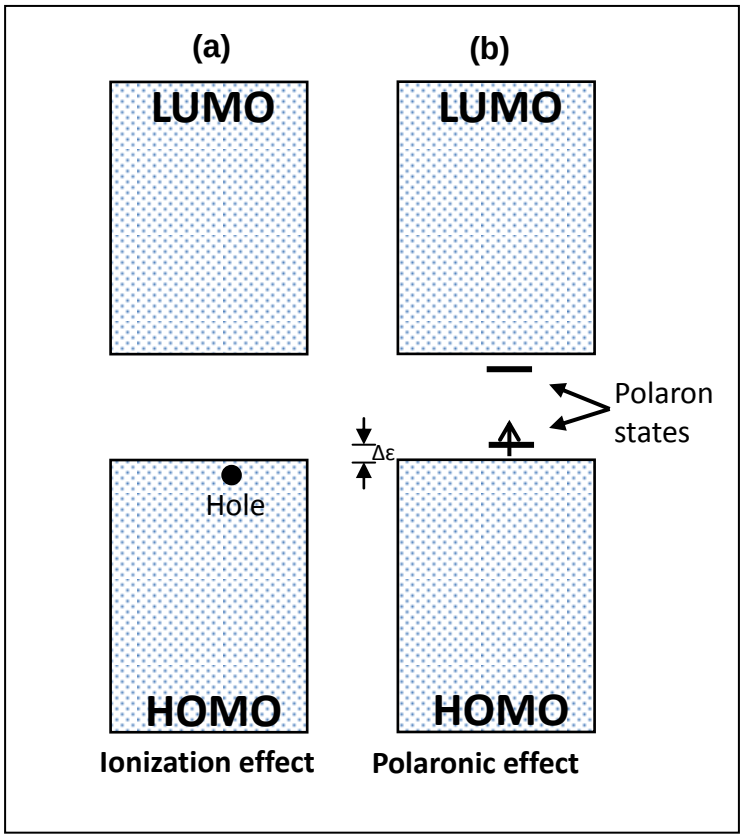

Figure 4. Schematic representation of the ionization effect (a) and the formation of polarons (b).

This analogy can be extended further by considering the condition when a second electron is removed from the chain. In this case we can have two outcomes; we can either take a second electron from the polaron states, or we can take the electron from anywhere else on the chain, in which case we have two polarons. In the former case, we have a bipolaron formation. A bipolaron is defined as a pair of like charges associated with a strong local lattice distortion. The formation of a bipolaron implies that the energy gained by the interaction with the lattice is larger than the coulomb repulsion between the two charges of same sign confined in the same location. The electronic band structure corresponding to the presence of two polarons and that of one bipolaron is depicted in Figure 5.

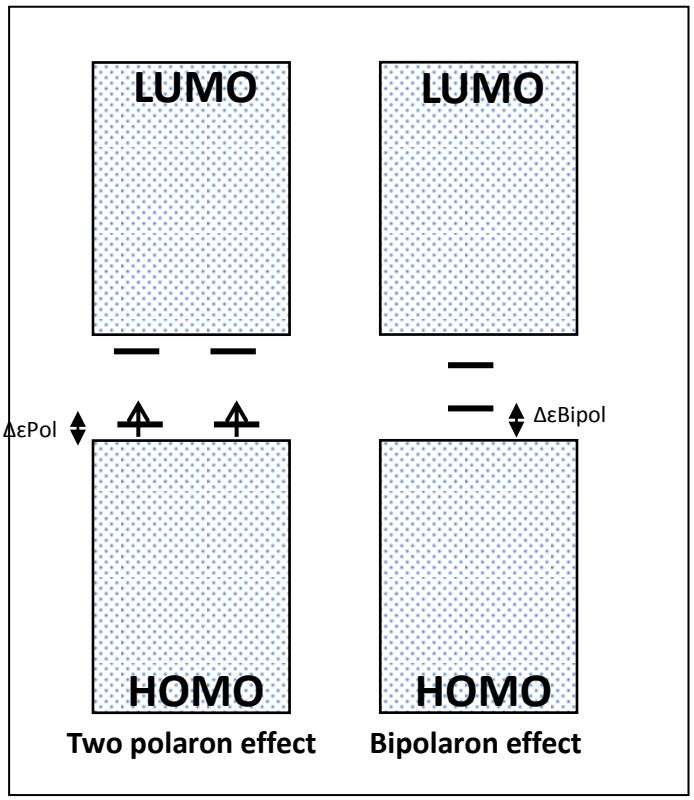

Figure 5. Schematic representation of the formation of a polaron (a) and bi-polarons (b).

Since the lattice relaxation around two charges is stronger than around only one charge, E_{dis} for the bipolaron is larger than E_{dis} for the polaron and the electronic states appearing in the gap for a bipolaron are further away from the band edges than for a polaron. Polarons and bipolarons in OLED and OPV devices are usually associated with charge injection or extraction in the semiconductor as shown in figure 6.

Excited states or excitons are also a popular feature of organic semiconductors and can either be generated optically as in OPVs or electrically as seen in OLEDs. Optical excitation promotes an electron from HOMO to LUMO thus producing an exciton or an e-h pair. Electrical excitation refers to the process of injection of electrons and holes into the organic material. Once the carriers are within the capture radius of each other, they recombine to form an exciton. The generation of excitons via injection and absorption in OLEDs and OPVs are shown schematically in figure 6.

(a)

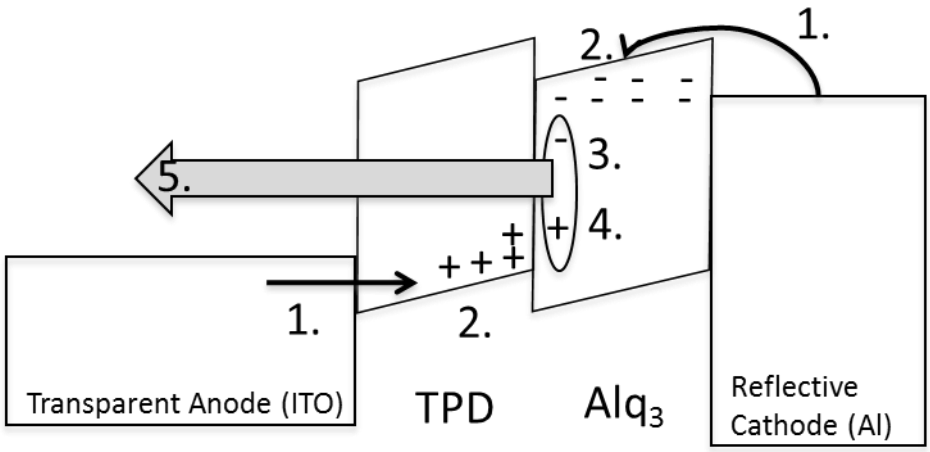

1. Charge Injection
2. Charge Transport
3. Exciton Formation
4. Radiative Exciton Recombination
5. Light Emission

(b)

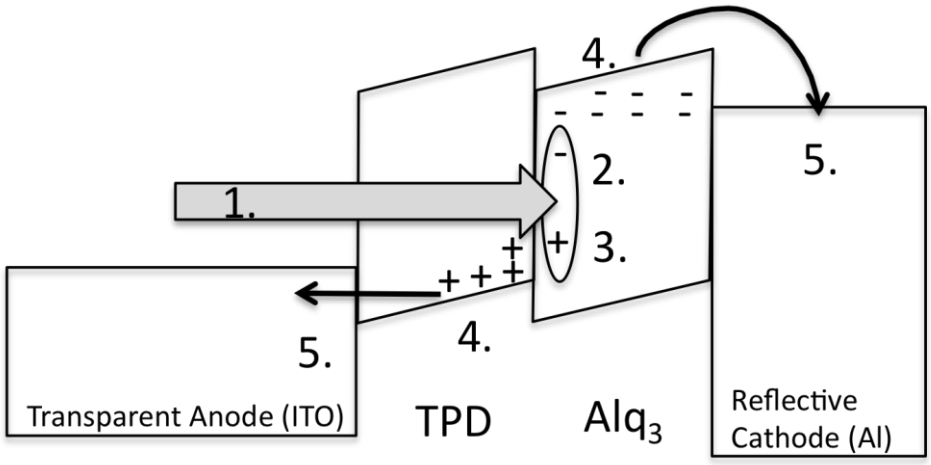

1. Light Absorption
2. Exciton Generation
3. Exciton Separation/Charge Generation
4. Charge Transport
5. Charge Extraction

Figure 6. General operation principle of an OLED (a) and OPV (b).

In general OLED and OPV efficiencies are dominated by the generation or dissociation of excitons. They are typically grouped into two categories depending on their spin configuration. Singlets refer to excitons with anti-parallel electron spin with zero net spin angular momentum while triplets correspond to excitons with non-zero net spin angular momentum as shown in figure 7. Singlets can decay radiatively with time scales in the range of nanoseconds but triplet radiative transitions are usually forbidden unless through phosphorescence decay[33-34]. In this case transitions are potentially allowed directly from the triplet excited state (T_1) to the singlet ground state (S_0) as shown in figure 8. This process usually occurs when a heavy metal such as iridium is incorporated into the organic[35]. Excitons generated in this manner tend to occupy energy levels on both the organic and the metal. This type of arrangement enhances the coupling between the exciton's spin and its motion resulting in enhanced spin orbit coupling. As a result, a triplet can undergo a phase change from M_s=0 in the triplet state (see figure 7) to M_s=0 in the singlet state, or even experience an entire spin flip. Thus transitions to the singlet ground state are now possible, and depending on the wavelength of the energy released in this process, light emission can be observed in the form of phosphorescence.

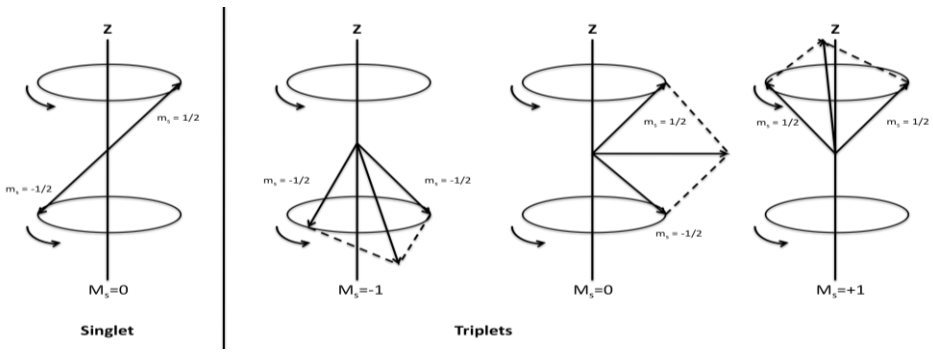

Figure 7. Spin characteristics of excited states illustrating the spin configuration of singlets and triplets. M_s represents the total angular spin.

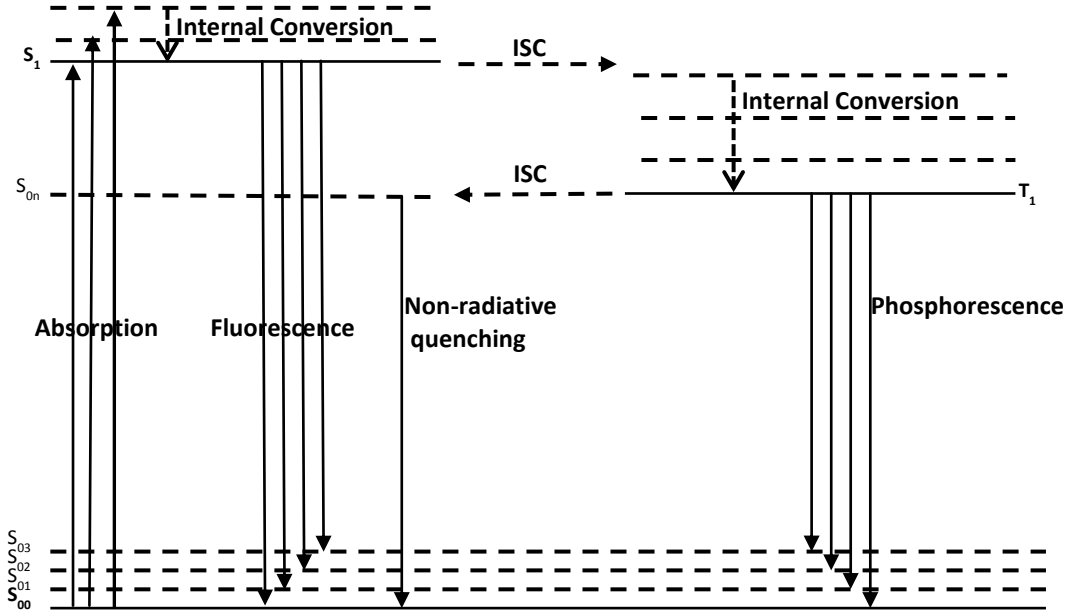

Figure 8. Jablonski diagram of some photophysical transitions. Dotted lines illustrate exciton vibrational modes and ISC represents Intersystem Crossing between the two states.

Triplet decay time are usually much longer than singlets, typically a few microseconds. Thus when it comes to OLEDs, with no phosphorescent material, the concentration of singlets ultimately determines the device efficiency. This concentration relies on the random spin injection of charge carriers into the corresponding transport layers of the device via the electrodes. Hence for electroluminescence devices the ratio of singlet to triplet formation is typically 1:3. This means that the maximum possible efficiency for OLEDs is 25%. It should be noted that this ratio can only be applied to the generation rate. The steady state populations are very different as triplets have lifetimes of at least 1000 times more than singlets.

Singlets are also the dominant exciton in OPV devices. Triplet generation is forbidden due to conservation of spin angular momentum. Thus as in OLEDs devices the concentration of singlets play a key role for determining device efficiency. However equally important is the dissociation

and transport of singlets to their respective electrodes. Generating a large concentration of singlets without being able to transport the dissociated carriers to the electrodes is a futile project.

1.5 Electron-Hole Injection

Charge injection is one of the fundamental concepts for determining organic semiconductor efficiency. In OLEDs, the hole current is limited by injection, and the electron current is strongly influenced by the presence of traps owing to metal-organic interactions. In order to enhance carrier injection the selection of efficiently electron-injecting cathode materials and the use of appropriate surface treatments of anodes are of great importance. This section discusses some of the principles determining charge injection in organics and some methods for optimizing this behaviour.

1.5.1 Injection Barriers and Recombination Current

As discussed in section 1.4, when an electrical potential difference is applied between the anode and the cathode such that the anode is at a more positive electrical potential with respect to the cathode, injection of holes occurs from the anode into the hole-transport layer (HTL), while electrons are injected from the cathode into the electron-transport layer (ETL). The injected holes and electrons each migrate toward the oppositely charged electrode, and the recombination of electrons and holes occurs near the junction in the luminescent ETL. Upon recombination, energy is released as light, which is

emitted from the light-transmitted via the anode and substrate.

The energetic barrier in a double layer structure should be designed to facilitate hole-injection from the HTL into the ETL and to block electron injection in the opposite direction in order to enhance the probability of exciton formation and recombination near the interface region. As shown in Fig. 1, the HOMO of the HTL is slightly above that of the ETL, so that holes can readily enter into the ETL, while the LUMO of the ETL is significantly below that of the HTL, so that electrons are confined in the ETL. The low hole mobility in the ETL causes a buildup in hole density, and thus enhance the collision capture process. Furthermore, by spacing this interface at a sufficient distance from the contact, the probability of quenching near the metallic surface is greatly reduced.

1.5.2 Dipole Layers, Organic-Metal Interfaces

Organic-metal interfaces are one of the most important features for determining efficient carrier injection into the organic. Dipole regions between the interfaces of the two layers can arise as a result of the perturbation of the metal surface electron density tail related to the presence of the adsorbed (chemisorbed or physisorbed) organic molecules. An interface dipole with its negative pole pointing toward the organic layer and its positive pole toward the metal increases the metal work function i.e. decreases the fermi energy and increases the HOMO energy of the organic layer by adding a electrostatic energy. As a result, the hole injection barrier is reduced. Accordingly, reversing the direction of the interface dipole reduces the electron injection

barrier. Thus, work function increase/decrease is associated with an improvement of hole/electron injection. Because the metal work function is affected, that is, the interface dipole is created, by adsorbing an organic layer; a proposed improvement route for charge injection is to chemisorb molecular species on the metal surface. Thus careful attention must be given to the effect of dipole regions when determining injection barriers.

1.5.3 Fowler Nordheim Tunneling

Fowler Nordheim (FN) tunneling is the process by which electrons tunnel through a potential barrier, rather than escaping over it as in thermionic or photo emission. It occurs because the wave function of an electron does not vanish at the classical turning point, but decays exponentially into the barrier (where the electron's total energy is less than the potential energy). This is shown schematically in figure 9.

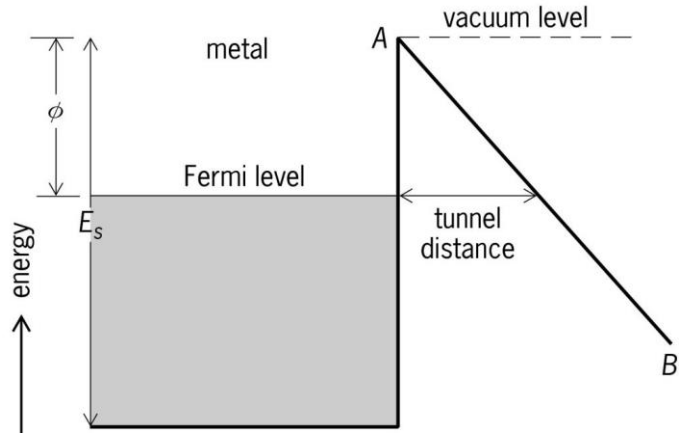

Figure 9. Schematic of Fowler Nordheim tunneling. At the presence of electric field, the potential outside the metal will be deformed along the line AB, resulting in a triangular barrier through which electrons can tunnel.

Thus there is a finite probability that the electron will be found on the outside of the barrier. A strong electric field lowers the barrier and makes it sufficiently penetrable, that is, relatively thin and low. The FN equation quantifies this effect by observing the tunneling current density (J) through the active layers of the material at the presence of an applied electric field E .

$$J = \frac{q^3 E^2}{8\pi h \Phi_b} \exp\left(- \frac{4\sqrt{m^* \Phi_b^3}}{3\hbar q E} \right) \quad \textbf{(1)}$$

Where q is the elementary charge, $\hbar$ is the reduced Planck's constant, Φ_b is the potential barrier height at the electrode-active layer interface and m^* is the effective mass of the injected electrons.

1.5.4 Thermionic Injection

Thermionic injection can be regarded as the evaporation of electrons owing to their thermal excitation. To leave the emitting body, the electrons must overcome the potential barrier at the boundary of the body. When the body is at low temperatures, the number of electrons with enough energy to overcome the barrier is small. As the temperature increases, the number of such electrons rises, and the thermionic injection increases. Just as FN case the principal quantity characterizing bodies with respect to thermionic injection is the saturation thermionic current density J at a specified temperature. Such a characteristic can clearly be seen in TPD like materials[15]. For thermionic emission by uniform (with respect to the work function) emitters into a vacuum in the absence of external electric fields, the quantity J is given by the Richardson-Dushman equation.

$$J = AT^{2}(1-\bar{r})\exp\left(\frac{-e\Phi}{kT}\right) \quad \textbf{(2)}$$

Where A is a constant of the emitter, T is the temperature of the emitter in Kelvin, $\bar{r}$ is the average coefficient of reflection from the potential barrier at the boundary of the emitter for thermo-electrons with different energies, $e\Phi$ is the work function, and k is the Boltzmann constant.

1.5.5 Image Force Barrier Lowering

It can be shown that the electric field in a semiconductor is identical to that of the carrier itself and another carrier with opposite charge at equal distance but on the opposite side of the interface. This phenomenon is referred to as the image charge. Image charges build up in the metal electrode as carriers approach the metal-semiconductor interface. The potential associated with these charges reduces the effective barrier height. This barrier reduction is of interest since it depends on the applied voltage and leads to a voltage dependence of the reverse bias current.

1.6 OLED Structures and Operation

1.6.1 Introduction

The principle of operation of OLEDs is very similar to inorganic LEDs and was briefly touched upon is section 1.4. Efficient device operation not only depends on the choice of molecules with appropriate electronic and optical properties, but also on the design of the device structure. Figure 10

presents different OLED structures for producing electroluminescence. Figure 10(a) shows electroluminescence can be achieved with a simple single layer device, however the performance is poor since electrons and holes can reach the opposite contact and excitons can be quenched at the electrodes. The two layer structure (figure 10b) introduces a separate hole transport layer. Holes are injected into emitter and electron transport layer and recombine with electrons near the surface. The three layer structure as shown in figure 10c, confine both charge carriers and excitons within the emissive layer, however the energy barriers at the interfaces can still impede the transport of electrons and holes from the electrodes to the emitter layer. The complex multilayer structure presented in figure 10d aims to overcome this issue by providing a separate hole injection (HI) and transport layers to form a staircase path for holes. A similar layer structure is used for electrons. The hole blocking layer prevents holes from penetrating into the electron transport layers whereas the electron injection layer has an intermediate LUMO energy to enhance the electron injection from the cathode. Another approach for overcoming the energy barriers at the interfaces is to use a two layer structure with doped emissive layer. This can alter the LUMO energy level of the emissive layer to facilitate a more efficient electron transport. However having dopant materials will inevitably increase intermolecular quenching due to reduced carrier mobility.

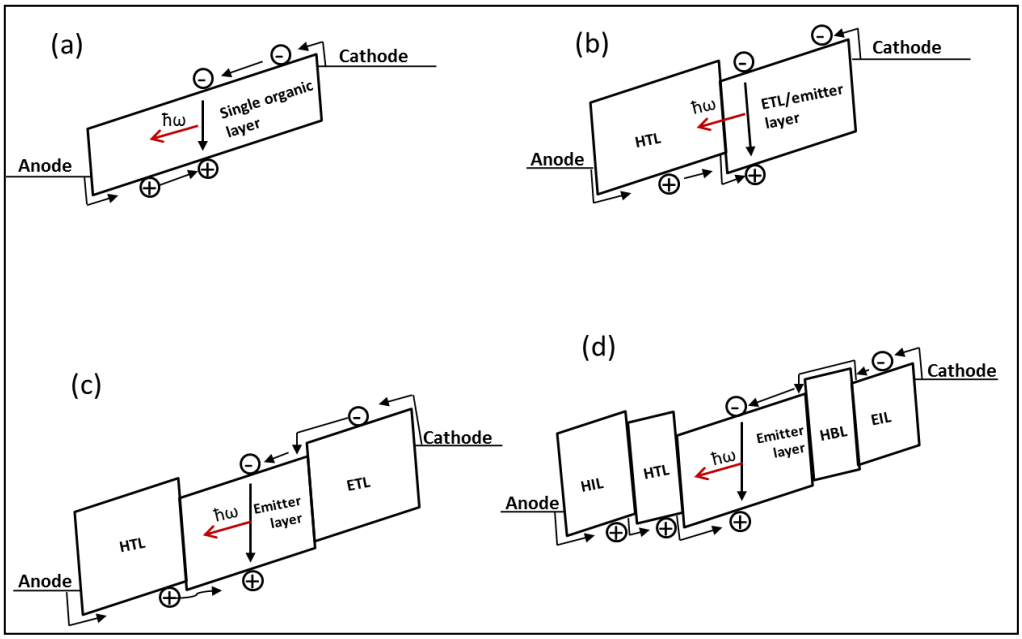

Figure 10. Layered sequence and energy level diagrams for OLEDs with (a) single layer, (b) double layer, (c) three layer and (d) multilayer structure with separate hole and electron transport layers.

1.6.2 Phosphorescence Organic Light Emitting Diodes (PhOLEDs)

As discussed in section 1.4 electroluminescence in OLEDs result in the formation of statistically distributed singlets and triplets. Due to the spin configuration of each type of exciton it is clear to see that the ratio of signlets to triplets is 1:3. The efficiency of OLEDs is typically dependent on the concentration of singlets generated as they are the primary source of excitons that can decay radiatively. Phosphorescent dyes incorporated into the OLEDs as hetro-junction blends can be used to overcome the efficiency limit imposed by the unavoidable formation of triplet excitons. Among some of widely used phosphorescent materials in OLEDs include Iridium, tris[2-(2-pyridinyl-κN)phenyl-κC], $Ir(PPY_3)$[36], and Tris[1-phenylisoquinolinato-C2,N]iridium(III),

$Ir(piq)_3$[37], to name a couple. Such phosphorescent materials or triplet emitters as they are commonly known can provide a mechanism where radiative decay from triplets can occur resulting in higher quantum efficiencies of the device.

The criteria for selecting a suitable phosphorescent material is that the energy of the lowest lying triplet state of the host material should be larger or at least comparable to that of phosphorescent guest. This will prevent the back energy transfer from guest to host and facilitate the exothermic energy transfer from host to guest. Thus the triplets that are generated have their electrons occupy both the organic and the emitter material. Thus each electron is subject to a different degree of spin-orbit coupling. As a result the total angular momentums of each electron (S_1 and S_2) precess at a slightly different rate and hence the magnitude of the combined angular momentum vector (S_1+S_2) will fluctuate between $M_s=\pm 1$ and $M_s=0$ resulting in the radiative decay of a triplet exciton to a singlet S_0 ground state.

Efficient and stable red and green-emitting phOLED are well known with high internal quantum efficiency around 100% and external quantum efficiencies in the range of 20-25%.. The realization of high performance deep blue phOLED however remains a challenge, because of the lack of efficient host molecules for blue emitters. Blue emitting phOLED host materials should have a high triplet energy which normally means a high band gap. The conjugation length present in the host molecules influences the triplet energy. It is found that a large conjugation length decreases the triplet energy, whereas a short conjugation length leads to a high band gap resulting in high driving voltage[38]. Thus, the development of efficient host materials for the

blue emitters is a challenging task compared to host materials for red and green emitters.

1.6.3 Polymer OLEDs

Polymers are also a common feature in OLEDs. The most commonly used polymers in OLEDs are poly(p-phenylenevinylene)[39] (PPV) copolymers and poly(9,9-dioctylfluorene)[40] (PFO) copolymers, which can emit electroluminescence across the entire visible spectrum from red to blue. The structures and properties of such materials are discussed further in section 1.1.2. One of the widely used polymers for promoting hole injection is poly(3,4-ethylenedioxythiophene)–poly(styrene)[41] known as PEDOT:PSS which has been found to be useful in a hybrid OLED architecture combining both the advantages of polymer LED and multi-layered small molecule OLED. PEDOT:PSS is an aqueous gel. The hydrated gel particles are formed by PSS interlinked by PEDOT chains. PEDOT:PSS acting as a HTL can smooth the ITO surface, reducing the probability of electrical shorts, decreasing the turn-on voltage and increasing the lifetime of the device. One of the potential drawbacks of using PEDOT:PSS is its acidity which could get as low pH as ~3.

Polymer blends such as 2-(4-biphenyl)-5-(4-tert-butylphenyl)-1,3,4-oxadiazole[42] (PBD) and polyvinylcarbazole (PVK)[43] are also a common feature in tunable OLEDs. In such materials each component of the blend emits at a different energy. The colour is tuned by varying the applied voltage, higher voltages result in more emission from the higher excitation

energy (toward blue emitting) polymer, while also resulting in higher overall brightness due to increased current injection into the device. The thickness and the concentration of each can also be varied to achieve the desired light output.

1.6.4 Conventional, Inverted and Metal Oxide OLEDs

Conventional OLEDs consist historically of a transparent conductive anode, typically ITO coated glass covered by an organic multilayer for selective carrier transport and light emission. The cathode contact is employed by evaporation of a low work-function metal, such as Ca, and Al or by incorporating an injection layer such as LiF, forming an opaque electrode on top. Using this device architecture the emitted light is coupled out through the bottom contact making chip OLED integration with silicon-based driver electronics rather impossible. Especially for high resolution full colour displays an active matrix addressing scheme involving amorphous silicon, polycrystalline silicon or complementary metal-oxide-silicon (CMOS), technology is desirable. To overcome this it is necessary to develop a highly efficient OLED structure that allows emission via the top contact, thus the need for a top-emitting OLED where light is observed from the top cathode, or an inverted top-emitting OLED where a transparent anode is used as the top electrode (in an inverted OLED the cathode is at the bottom and the anode is on top of the organic layer(s)).

To enter successfully the general lighting market, OLEDs require a strong reduction in the cost of the devices as well as high performance levels.

In this respect, it is of particular importance to be able to generate electroluminescence from devices using air-stable charge-injection interfaces. Although some examples exist, these devices rely on the presence of ionic charges to generate a dipole across the metal-light-emitting-layer interface and their reported lifetimes are low[44]. Metal oxides are, in principle, promising candidates that may lead to good charge injection as they combine properties such as high transparency, low resistance, and air stability. Recently, there have been reports about the use of metal oxides as charge injection layers. They range from ultrathin layers on the anode side to nanostructured layers on the cathode side of the devices[45]. The use of a hole-blocking metal-oxide material on the anode side modifies the device efficiency by adjusting the charge balance in the device[46]. A more beneficial use of the metal-oxide layer is as an alternative cathode material. The use of an unreactive metal oxide as the cathode is appealing as this would allow the preparation of OLEDs requiring no, or only simple, encapsulation. This would significantly reduce costs and, therefore, increase the feasibility of the use of OLEDs in display and especially lighting applications[46].

1.6.5 Light Out-coupling

A large proportion of the light produced by OLEDs is trapped inside the OLED due to the effects of total internal reflection particularly at the substrate/air interface[44]. The majority of light emitted at angles away from the vertical cannot come out of the OLED as they see the interface with air as a mirrored surface. A surface structured out-coupling film enables these

waveguided modes to be emitted by changing the incident angle. Each OLED device has its own unique emission profile. To maximize the out-coupling efficiency it is important to use an out-coupling structure designed to work with the precise characteristics of the OLED.

The integration of a micro-structured optical film on the surface of the OLED enables more options than simply improving device efficiency. By modifying the surface microstructures, the direction and intensity of the light emitted by the OLED can be manipulated to create a variety of effects. For example the out-coupling optical features can be modified to provide additional light redirection so that the same film can make the OLED comply with anti-glare standards for office fittings, provide an asymmetric light pattern, or give a two beam strip emission. In this way, a single OLED design, coupled with different surface films, can produce a range of lighting products.

1.6.6 OLED Efficiency and CIE Coordinates

OLED efficiency is typically determined from the ratio of electrical power supplied to a device and the optical power output that escapes the glass substrate. It can be divided into internal efficiency that is number of generated photons per injected electron and the optical output coupling efficiency which is the percentage of the generated light that is able to escape from the device via the glass substrate. The latter depends strongly on the refractive index of the emitting layer, refractive index of the substrate and the reflectivity of the cathode. In a thick device (relative to the wavelength of light) and in the absence of scattering effects the theoretical equation for

determining the external quantum efficiency (η) of an OLED is given by Eq. (3).

$$\eta = \xi \gamma r_{st} \eta_{pl} \quad \textbf{(3)}$$

ξ is the out-coupling efficiency, γ , is the recombination efficiency, r_{st} is the ratio of singlet to triplet excitons formed from the recombining charge carriers, and η_{pl} is the photoluminescence (PL) quantum yield.

In terms of device characterisation, the main efficiency parameters that are used are either lumens per watt (lm/W), the power efficiency or luminous efficacy, or candelas per amp (cd/A), the current efficency.cd/A is a measure of the intensity of light emitted for a given electric current and is calculated by E_{ff}=L/J, were L is candela per meter square, (cdm^{-2}) and J is the current density. Efficiency given in terms of lm/W is very similar to cdm^{-2} except that in this case the underlying measurement is power and is given by E_{ff}=L/W, where L represents luminous flux (lumens) and W is electrical power in watts.

CID Coordinates

A good illumination source can be fully described by a simple set of parameters. The colour of the light source is given by its CIE chromaticity coordinates (x,y) as shown in figure 11. The CIE coordinates of a light source of given energy and spectral shape will fall within the area of the curve. Summing light at all wavelengths uniformly gives the white or neutral point, found at the center of the diagram (coordinates = 0.33, 0.33). Thus, mixing light from two or more sources can be used to generate white light and such a technique can be used to measure the purity of the observed light. Mixing light

from blue, red and green OLED sources can give light that will be perceived by the observer as white. Many organic small molecules for red[47], green[48] and blue emitters[49] have been synthesized. Recently, high efficient and pure red fluorescent and green OLEDs have been developed with CIE x, y coordinates and electrical efficiencies of (0.67, 0.23)[47] and 11 cd/A and (0.29, 0.64)[48] and 21 cd/A, respectively. However, the colour purity and efficiency of the blue-light emitters are still lower than the requirements for balancing with red and green emitters for full colour displays. Therefore, improvements in the blue emitting performance are necessary, particularly for large display applications.

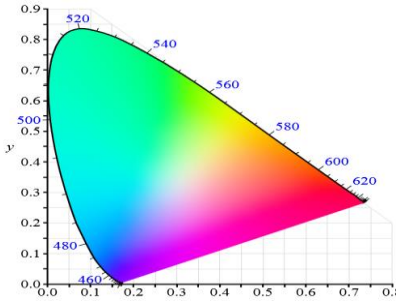

Figure 11. A typical CIE chromatic diagram[47]

1.6.7 OLED Fabrication Techniques

OLED fabrication techniques can broadly be categorized into two groups depending on the primary type of material used for fabrication. Small molecule OLEDs are typically fabricated using vacuum sublimation. A detailed review of this process is provided in section 4.0. OLEDs incorporating polymers however can be solution processed using spin coating, doctor blading, inkjet printing and drop casting. This section aims to give a brief overview of each process.

Drop casting and spin coating are very similar in the sense that both involve dropping a few drops of solution processed polymer onto a substrate. In the case of drop casting, once the polymer solution is dropped onto the substrate it is briefly heated for the solution to evaporate leaving behind the required polymer. It is very simple technique and produces very little material waste, however it does limitations when it comes to a large surface area, material thickness is very hard to control and it produces poor uniformity.

Spin coating was discussed in detail in section 1.1.2. In general it is very similar to drop casting except that in this case the solution is dropped onto a spin coater providing a high spin revolution. Although this provides good uniformity, just as the drop casting method there's no control over thickness and produces a level of material waste.

Doctor blading is another technique used for polymer OLED fabrication[14]. This method involves spreading the material through a moving blade onto a stationary substrate. It provides good uniformity and is very efficient in covering large areas. However one major disadvantage of this technique is that it requires micrometric precision of blade regulation.

Inkjet printing is one of the most advanced techniques used for polymer fabrication[14]. Droplets of organic semiconductor solution are deposited onto the substrate. Film morphology can accurately be controlled via a variety of parameters such as air pressure, solution viscosity, evaporation rate and nozzle-substrate distance. This provides a technique where materials can be deposited in a layered structure covering large areas with great precision.

1.7 Excitons and Charge Transport

Investigation into the effects of excitons on free charge carries was first studied theoretically by Ern and Merrifield[50]. They showed that assuming that triplets are the dominant exciton type, the net result of a triplet-polaron interaction is the quenching of the triplets as shown in Eq. (4).

$$T_1 + D_{\pm 1/2} \overset{k_1}{\leftrightarrow} (T_1 ... + D_{\pm 1/2}) \overset{k_2}{\rightarrow} D_{\pm 1/2} + S_0^* \qquad \textbf{(4)}$$

In this equation $D_{\pm 1/2}$ is a polaron and $(T_1 ... + D_{\pm 1/2})$ is an intermediate pair state. The result of this process shows that the pair state can decay into a vibrationally excited singlet state (S_0^*) and a free charge carrier with a rate constant k_2. The left hand side of the equation represents the back scattering from the pair state with a rate constant of k_1.

The work of Ern and Merrifield is pivotal to this thesis as it shows that that triplet excited states can interact and potentially even block the transport of carriers within an organic semiconductor. Since the operation of OLEDs demands the generation of excess triplets (a simple calculation shows that a typical TPD OLED can generate ~10^9 triplets/cm^3, see section 12.2.1 for further details), a triplet/polaron encounter becomes increasingly likely. So far the role of such excited states on charge transport has been widely ignored, however if one can experimentally prove the existence of such effects, it can have widespread implications in device modeling. For example in recent years organic magnetoresistance (OMR) models such as the one proposed by Desai *et al*[51] or other transport models such as the one suggested by Song *et al*[52] are solely dependent upon the assumption that such interactions readily occur in devices, but very limited attempt has been made to experimentally

investigate them. By studying the effects of excited states on carrier mobility, this thesis endeavors to show that not only these effects do indeed exist but the simple act of generating them has profound implications on the level of importance that excited states can have on charge transport. We show that by generating excited states we also contribute to trap filling of energetic traps indigenous to the device, and it's the interplay of these two mechanisms that determines the degree at which excited states impacts the transport properties of free charge carriers. Both processes occur simultaneously and both have significant impact on carrier mobility. A more comprehensive analysis of this concept is given is section 9.5.

2.0 Material Purification

Prior to device fabrication, materials must undergo a careful purification process to remove impurities associated with the material. Impurities can act as energetic traps to incoming carries thus limiting the mobility performance of the material under test. Both materials used in thesis, NPB and TPD are typically purchased from Sigma Aldrich with manufacturer's purity concentration of 99.7% and both materials are carefully purified via a vacuum sublimation process prior to any mobility measurement. A schematic of the purification process is given in figure 12.

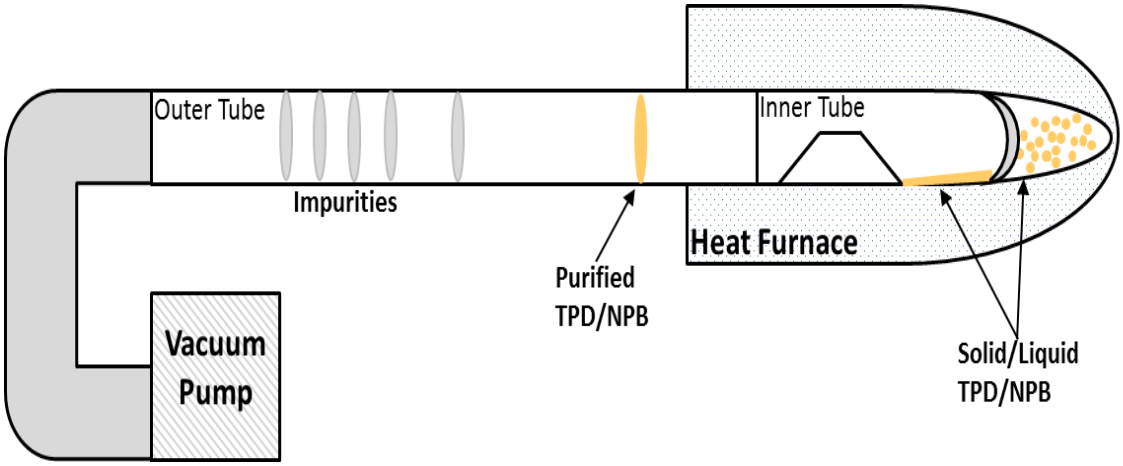

Figure 12. Schematic representation of material purification

As shown in figure 12, the purification apparatus consists of two parts, a long 40cm outer tube and a shorter 7cm inner tube. Both tubes are made from Pyrex glass. Typically 100mg of the required material is placed inside the inner tube. A thin filter paper is placed after the material is inserted to provide positional support and to prevent any material suction into the vacuum pump. The inner tube is then inserted into outer tube and pumped down. Finally the outer part of the tube containing the material is placed inside a heat source where periodic temperature steps are applied. The remainder of the tube is kept outside the heat source exposed to room temperature. The pressure in the tube is typically kept in range of $3\text{-}9\times10^{-6}$mbar.

A constant temperature increase is applied to the material and any impurities are observed on the outer tube as condensed precipitates. NPB and TPD boiling temperatures are in the range of 290°C and 310°C for both materials. Thus any precipitation outside this range would correspond to material impurity. The temperature is increased until all the material is evaporated. A record is kept of the position and temperature of the purified material where it later extracted.

3.0 Charge Transport Techniques

In general the main parameter that is associated with charge transport is the mobility (μ) of charge carriers as a function of electric field and temperature. Mobility of carriers is given by Eq. (5).

$$\mu = \frac{v_d}{E} = \frac{d}{Et} = \frac{d^2}{Vt} \quad \textbf{(5)}$$

v_d is the drift velocity, E is the applied electric field, d refers to the thickness of device, t and V correspond to the transit time of carriers and applied bias respectively.

There are several methods that can be utilized to determine the mobility. This section aims to give a comprehensive overview of some of the most common techniques used throughout this report.

3.1 Time of Flight (TOF)

3.1.1 Theory

TOF was first introduced by Kepler[53] and Leblanc[54]. In this method the organic material is sandwiched between two electrodes, one of them semi-transparent. A voltage is applied between the two electrodes giving rise to an electric field. The material is then irradiated by a short laser pulse in the proximity of one electrode to generate singlet excitons as shown figure 13. The effect of the electric field is to assist exciton dissociation and produce free charge carriers that drift to the opposite electrode depending on the direction

of the applied field. The carrier drift produces a current that is sensed as a voltage drop across a resistor placed in series with the sample.

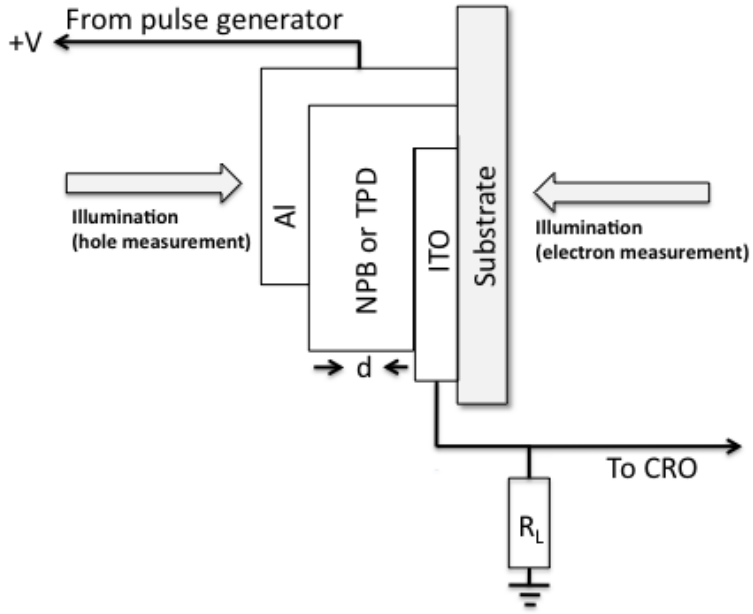

Figure 13. Schematic diagram of TOF experiment representing carrier transport with Al and ITO illuminated for hole and electron transport respectively.

3.1.2 Determination of Device Thickness

Determining the correct film thickness is one of the key pre-requisites for a successful TOF measurement. As light penetrates the sample, charge carriers are generated both at close proximity of the semi-transparent electrode and within the bulk of the device, resulting in a spatial distribution of carriers within the sample. This means that the distance travelled by carriers is no longer equal to the device thickness. Thus we require a device thickness that is large compared to the penetration depth (∂) of the laser. To determine the material thickness, we need to first evaluate the penetration depth. The

penetration depth is derived from the Beer-Lambert law as shown in equations 6.1-6.4.

$$I = I_0 e^{-\alpha x} \quad \textbf{(6.1)}$$

Or $$I = I_0 e^{-x/\partial} \quad \textbf{(6.2)}$$

Where I_0 is the intensity of the incident light, I is intensity of transmitted light through the sample of thickness x and α is the extinction coefficient.

Thus by converting to $\log_{10}$ and rearranging we have:

$$1/\partial = \ln(I_0/I)(1/x) = \frac{\log(I_0/I)}{x \log e} = 2.3\log(I_0/I)(1/x) = (2.3OD)/x \quad \textbf{(6.3)}$$

Where OD is $\log(I_0/I)$ representing optical density or absorption.

Therefore:

$$\partial = \frac{x}{2.3OD} \quad \textbf{(6.4)}$$

Figure 14a and 14b represent the absorption spectrum (or optical density) and the corresponding penetration depth of NPB and TPD respectively for wavelengths ranging from 200-450nm. Both materials were deposited via vacuum sublimation on a quartz substrate with a constant deposition rate of 2.5Å/s and a final thickness of 250nm.

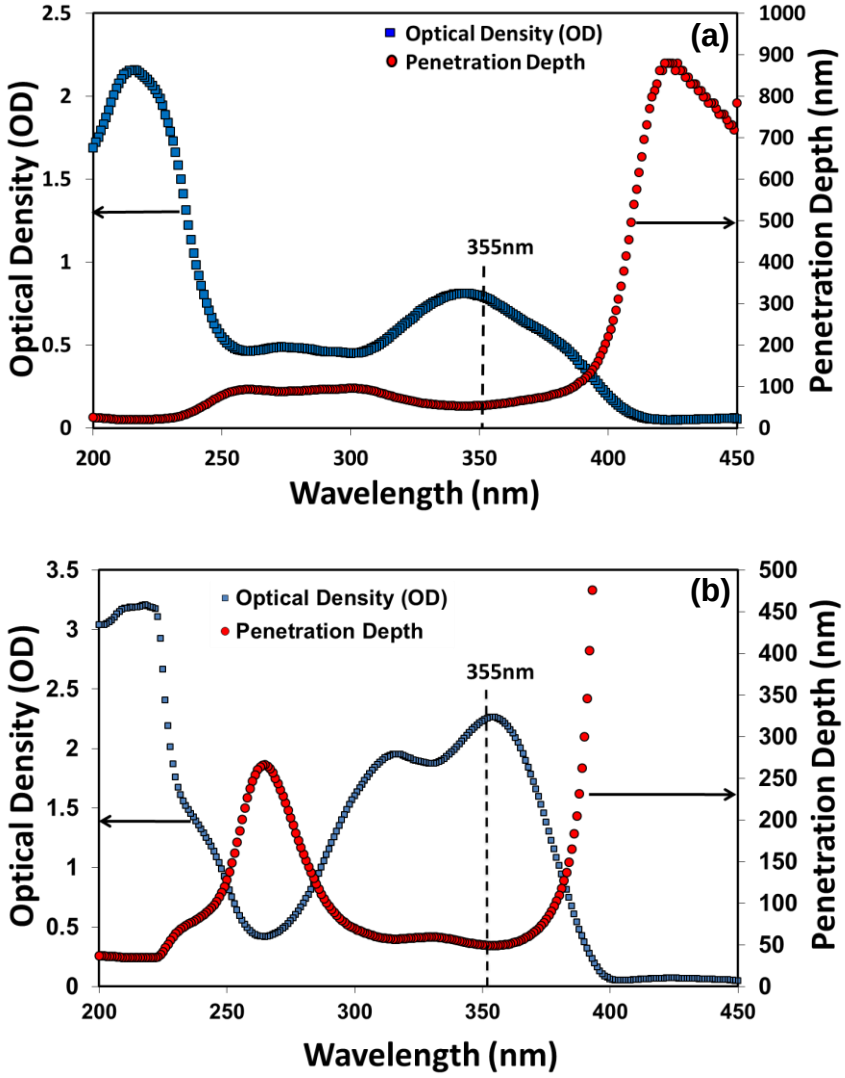

Figure 14. Optical Density and penetration depth spectra of (a) NPB and (b) TPD

Once the penetration depth of the material is evaluated, the ideal thickness sample is believed to be at least 10 times the penetration depth[55]. It is evident from figures 14a and 14b that the penetration depths for the two materials are 56.6nm and 49.2nm. Hence the device thickness should be at least ~600nm for NPB and ~500nm for TPD.

3.1.3 TOF Experimental Procedure

All TOF measurements were performed in a modified Linkam hot stage (TMS 94) under a constant flux of nitrogen (0.5 litres/minute) at temperatures ranging 233K to 300K. A photograph of the hot stage is shown in figure 15.

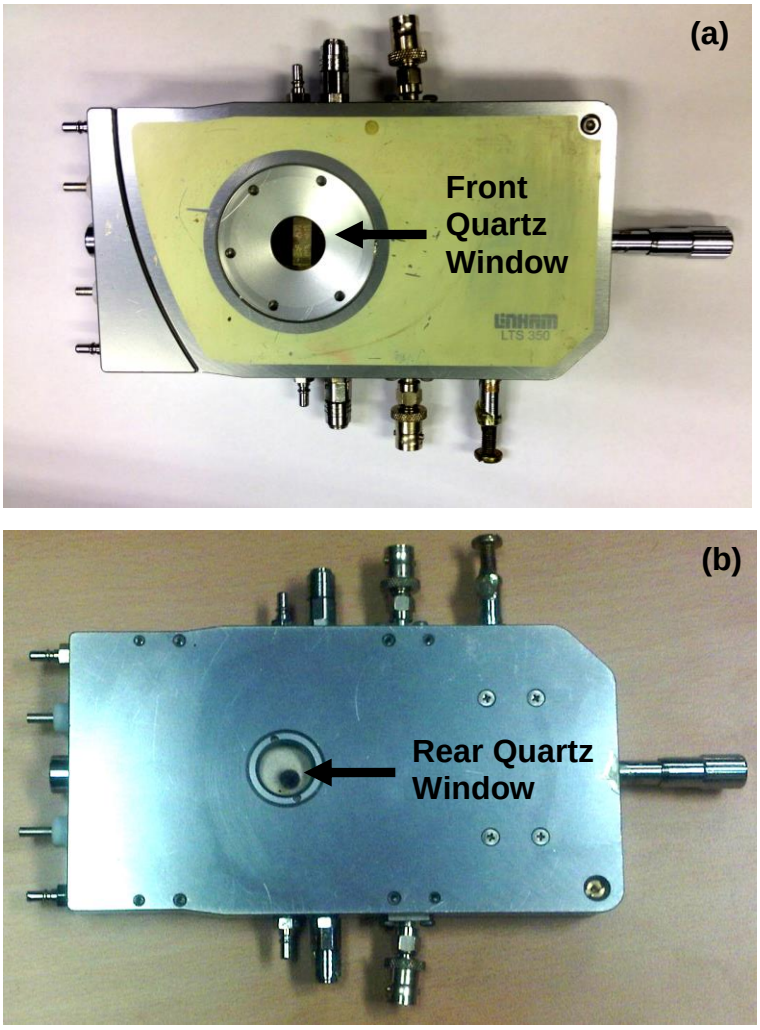

Figure 15. Front (a) and back (b) view of hot stage showing the respective illumination for hole and electron mobility measurements.

The sample is typically placed at the centre of the hot plate with the organic facing up. Thin metal wires and conducive silver paste are used to provide a contact for each of the electrodes. The wires are then soldered to

the BNC connectors to supply the required input/output connections. The input BNC is typically used to provide an applied electric field whilst the output allows the display of photocurrent signal on the oscilloscope. The choice of carrier transport to be resolved is made by altering the illuminated electrode (namely, Al for hole transport and ITO for electron transport). The Al electrode is semi-transparent to allow light transmission to the organic and is typically has a thickness of 50nm. It is important to note at this point that careful alignment of the sample with respect to the incident light is crucial for getting acceptable signal to noise ratios. It is not so much an issue for holes as the dimensions of the Quartz window allows for the entire sample to be illuminated. For electrons however, the incident light must pass through a much narrower aperture as shown figure 15b, thus alignments are made to ensure that irradiation occurs in the organic/ITO region. For temperature dependent measurements a liquid nitrogen cryogen is used to measure photocurrent signals below room temperature and a heated hot stage for higher temperatures.

Typical TOF experimental setup is shown in figure 16. A frequency-tripled Big Sky ND:YAG laser with wavelength of 355nm, pulse width of 5ns and a maximum output pulse energy of 20mJ is used to generate charge carriers for both electron and hole mobility measurements. A pulse generator provides the bias in the form of 4ms duration pulses at a repetition rate of 5 Hz, this is synchronized such that the laser output occurs 140μs after the pulse is applied. This delay ensures that the capacitive displacement current has decayed to zero before any photocurrent measurement is carried out. The samples are reverse-biased with the Al electrode positive for both hole and

electron measurements in order to minimize the dark current through the device. That current through the sample as a function of time is sensed as the voltage drop across a load resistor, the choice of which is further discussed in section 3.1.4. Each photocurrent is averaged to 256 laser pulses to provide a smooth signal with minimum noise.

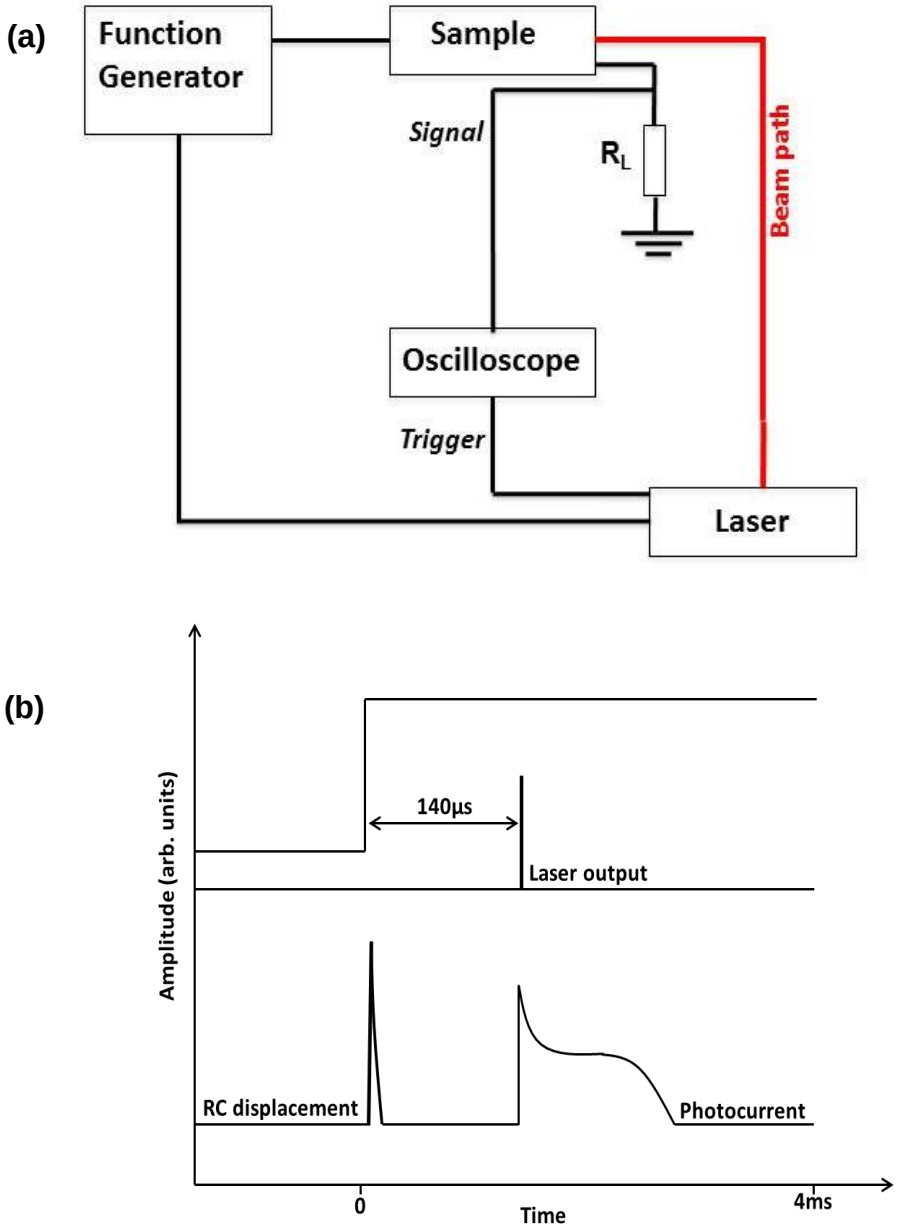

Figure 16. TOF experimental setup illustrating the experimental arrangement (a) and a typical non-dispersive output signal observed as a result of a laser pulse (b).

3.1.4 TOF Photocurrents: Non-Dispersive Transport

In general TOF results can be categorized into two groups, dispersive and non-dispersive. An example of a non-dispersive hole photocurrent typically observed in organic materials is shown in figure 17.

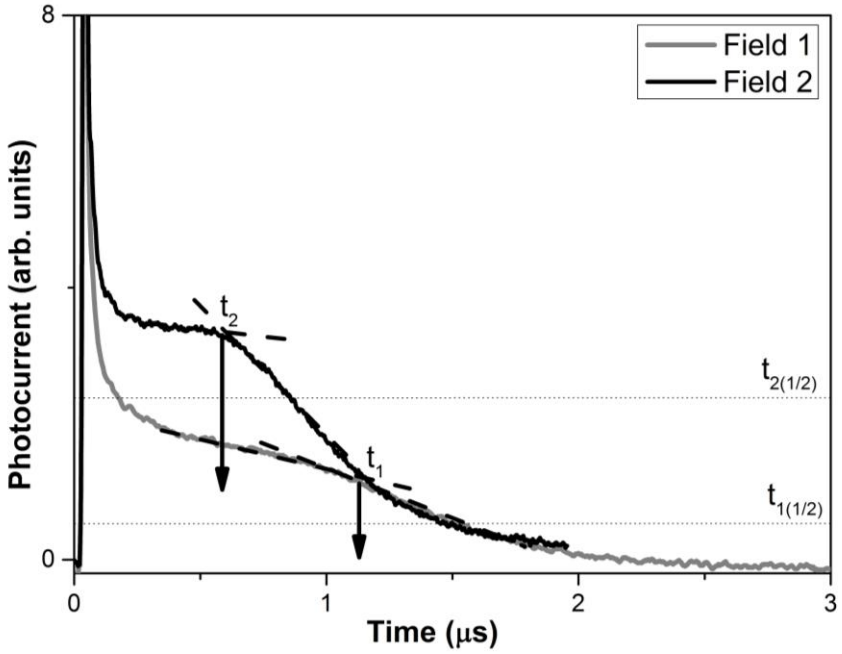

Figure 17. Typical TOF non-dispersive photocurrents at two separate electric fields for a typical 500nm TPD sample. Field 2 >Field 1. The fastest transit times are indicated by an arrow for each photocurrent. $t_{1/2}$ represent average transit time where $t_{1/2}$ is taken as the time to half plateau height.

In figure 17 the initial spike is related to carriers being harvested at the closest electrode i.e. illuminated electrode. In the case of TPD and NPB electrons are extracted at the Al electrode leaving behind holes to traverse the sample towards the ITO contact. An applied electric field assists this transportation. The subsequent flat plateau corresponds to the charge carriers

moving with a constant average drift velocity. The fact that a constant drift current is observed shows an absence of deep hole traps. The current remains constant until the leading edge of the carriers reaches the opposite electrode at time $t = t_t$ (transit time). The duration of this current depends upon the strength of the field and the level of disorder in the system. Finally, a transient region is seen where the signal drops to zero with a large tail. This effect is known as diffusion broadening and depends on three factors (see section 3.1.5), all of which have a direct impact on the mobility. To recover the transit time, straight lines are fitted either sides the flat plateau region and the intersection of these two lines is chosen to be the transit time. Hence by obtaining equations for both lines, the transit time is recovered by solving the two equations simultaneously.

3.1.5 Parameters Affecting TOF Photocurrents

Energetic Disorder

Depending on the degree of disorder and where within the Density of States (DOS) the charge carriers are generated, free carriers take different routes to get to their final destination. The effect of disorder is explained in more detail in section 5.1.

Absorption depth

There will always be a finite absorption depth where most of the incident light in absorbed resulting in a finite width of the sheet of charges, thus resulting to carriers being generated at different locations within the sample.

Charge traps

Charge trapping is caused by both the degree of impurity within the material and also self-trapping of carriers as a result of a broad energetic distribution. See section 9.5.1 for further analysis on site distribution energies in disordered organics. Both effects can severely affect carrier mobility and should be accounted for when analyzing transport properties of organics. Carriers can be captured in shallow or deep trapping energy levels lying within the band-gap of the organic material. Shallow traps tend to have lifetimes in the nanosecond and microsecond range and carriers can be thermally released by phonons and still contribute to the photocurrent[56]. On the other hand carriers captured in deep traps have very long lifetimes, typically a few milliseconds[57] and usually decrease the magnitude of both the photocurrent and the mobility of carriers[56]. This means that the purity of material is crucial when measuring charge transport properties. Having an impurity of even 1% could have significant impact on the mobility values and the diffusion broadening[58] of the photocurrent.

3.1.6 Conditions for TOF

In order to accurately determine the mobility of charge carriers, three conditions must be met; width of the RC time constant, absorption depth of laser and the avoidance of space charge current[59]. This section gives a brief overview of each effect.

RC constant

The system under test is effectively a plate capacitor and would have an associated RC time constant. The RC response must be much faster than the transit time to ensure that there is no interference with carrier signal. This can be achieved by tuning the terminating resistor appropriately. A 50Ω resistor is usually sufficient to provide both a fast RC drop and a good signal to noise ratio. Measuring sample capacitance before test is also important for evaluating the total charge across the sample. Typical sample capacitances for both materials are in the range of 0.20-0.3nF.

Absorption and penetration depth

Figure 14a and 14b show the absorption spectrum for TPD and NPB for wavelengths ranging from 200-450nm. As discussed earlier light penetration depth must be much smaller than the sample thickness. Otherwise, the assumption that carriers can traverse the whole of the sample does not hold. Typically the thickness of the sample is made at least ten times the penetration depth[53].

Space charge

To ensure accurate transit times, the total charge created by photo-generated currents must be less than the stored charge across the sample given by $Q = CV$. In the case where light intensity is too high a distinctive peak is observed across the flat region of the signal for non-dispersive photocurrents. This behaviour corresponds to the excess of charge within the system and distorts the inflection point arrival time of the carriers. The

presence of excess charge carriers can also alter the shape of the photocurrent signal so as to make it difficult to determine the nature of the transport, i.e. dispersive or non-dispersive. More crucially however, an excess of charge can change the uniformity of the electric field across the sample, resulting in inaccurate mobility calculations.

For dispersive photocurrents, space charge regions cannot be resolved via simple observation of photocurrent signals as no distinctive feature is observed even with a double logarithmic plot. Thus comparison of photo-generated charge and sample charge is always important to determine if space charge is present. Total photo-generated charge can be easily evaluated by integrating the area underneath a photocurrent signal. Typical photo-generated charge is in the range of 10^{-15} - 10^{-12} C depending on the strength of the applied electric field and the intensity of the laser. This value is at least an order of magnitude less than the capacitatively stored charge on the sample at a certain bias.

The field uniformity can also be affected by the presence of deep charge traps. Carriers trapped in deep energy levels produce an internal electric field which contributes to the space charge build in the system[60-61].

3.1.7 TOF Photocurrents: Dispersive Transport

Carriers in a photo-generated sheet can move with a very broad distribution of drift velocities resulting in almost featureless photocurrent transients as shown in figure 18a. This behaviour is referred to as dispersive transport and is due to a broad distribution of shallow traps and/or the level of

spatial disorder in a system. The latter corresponds to the mean intersite distances and is discussed in more detail in section 5.1. On average it has been shown that an increase in spatial disorder would increase the dispersive nature of photocurrent signals in TOF[62-63]. A theoretical model based upon such a system where there is an exponential distribution of shallow traps and thus a constant drop in average drift velocity with time can be represented in the form of the Scher-Montroll dispersive law[64]. In this model, Scher and Montroll demonstrated that the overall hopping rate of carriers can be modeled in relation to a single dispersion parameter as opposed to a Gaussian distribution (see section 5.1). This was achieved by averaging the hopping rate across the entire lattice structure. The final results of this model as a function of time (t) and dispersion parameter (α) are shown in equations 7 and 8.

$$I(t) \propto \frac{1}{t^{(1-\alpha_1)}} \Rightarrow I(t) \propto t^{-(1-\alpha_1)} \qquad \text{For } t < t_t \qquad \textbf{(7)}$$

$$I(t) \propto \frac{1}{t^{(1-\alpha_2)}} \frac{1}{t^{2\alpha_2}} \Rightarrow I(t) \propto t^{-(1-\alpha_2)} \qquad \text{For } t > t_t \qquad \textbf{(8)}$$

Scher and Montroll assume an exponential distribution of charge traps, thus they conclude that $\alpha_1 = \alpha_2$. However, it should be noted that in most disordered organic systems such an assumption is not entirely accurate. The distribution of charge traps is still a debatable topic and requires further analysis.

With these equations in mind one can now determine the carrier transit time in dispersive transport systems. A double logarithmic plot of the current-time graph will now clearly indicate the inflection point of the fastest carriers. The

transit time is evaluated as the intercept of the asymptotes to the double logarithmic graph as shown in figure 18b. It is important to note that for this model to be valid, the pre and post transit slopes must follow a gradient that is less steep than -1 to a gradient that is more steep than -1, thus in reality $\alpha_1 \neq \alpha_2$

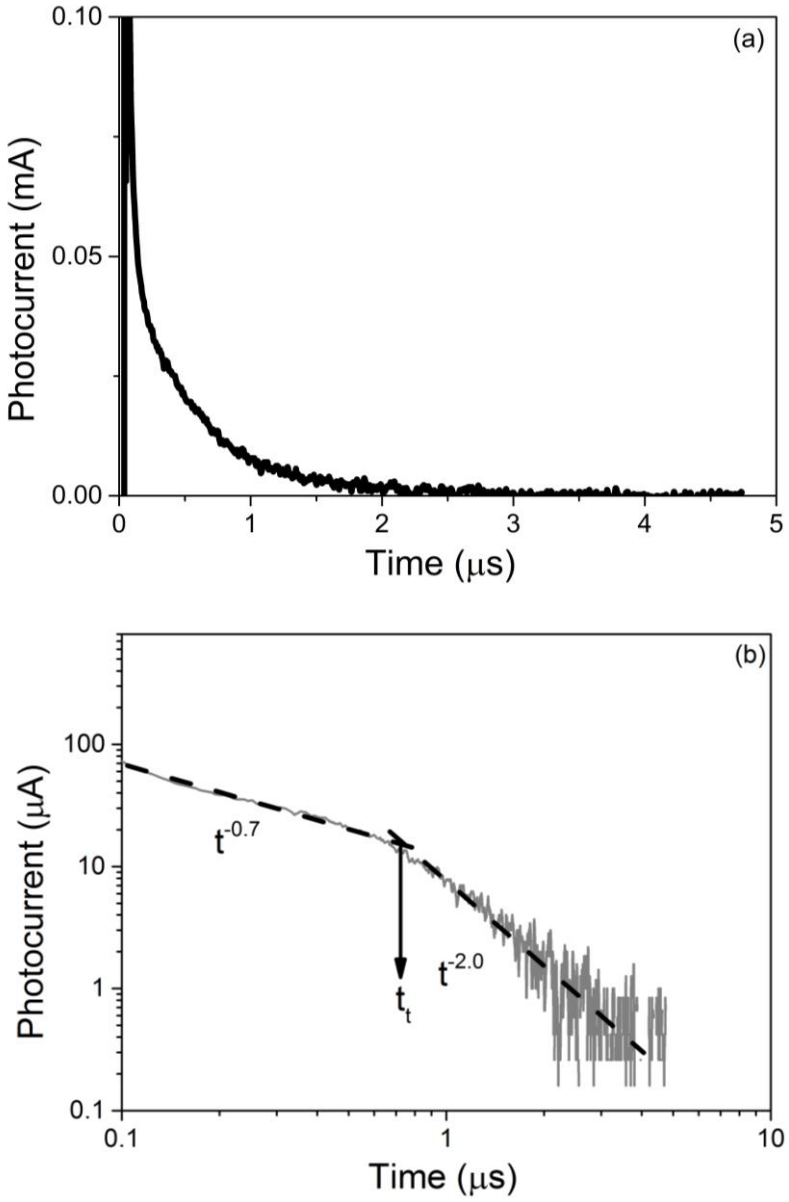

Figure 18. Typical TOF dispersive photocurrent plotted with linear scale (a) and a double logarithmic scale (b). The transit time is determined by the intersection of asymptotes as shown from the arrow in (b).

3.2 Dark Injection (DI) Space Charge Limited Current Method

This technique is similar to TOF in which one measures the time evolution of the current to find the time taken by carriers to drift across the sample. However, in this case it involves the direct injection of charge into the sample via a voltage pulse without the use of a laser. Also unlike TOF it relies on the fact that with this method it is important to sustain a maximum current, the so called space charge limited (SCL) current within the sample. The upper limit of this current is limited by the maximum amount of charge that can be injected into the device due to Coulombic repulsion from the charges already injected into the sample. In order to sustain this maximum SCL current one needs a long voltage pulse to provide an “infinite” reservoir of charge and a zero injection barrier between the work function of the electrodes and HOMO and LUMO layers of the material. A contact that is capable of sustaining this SCL current is called an ohmic contact. Figure 19b and 19c show an ideal theoretical and an experimental DI transient graphs respectively.

In section 9.3 we will discuss the effects of excited states on transport properties of carriers. One effective method to generate such excited states is to apply an offset bias prior to any transport measurement, as shown in figure 19a. By applying an offset bias carriers of opposite polarity are injected into the sample resulting in the generation of excited states.

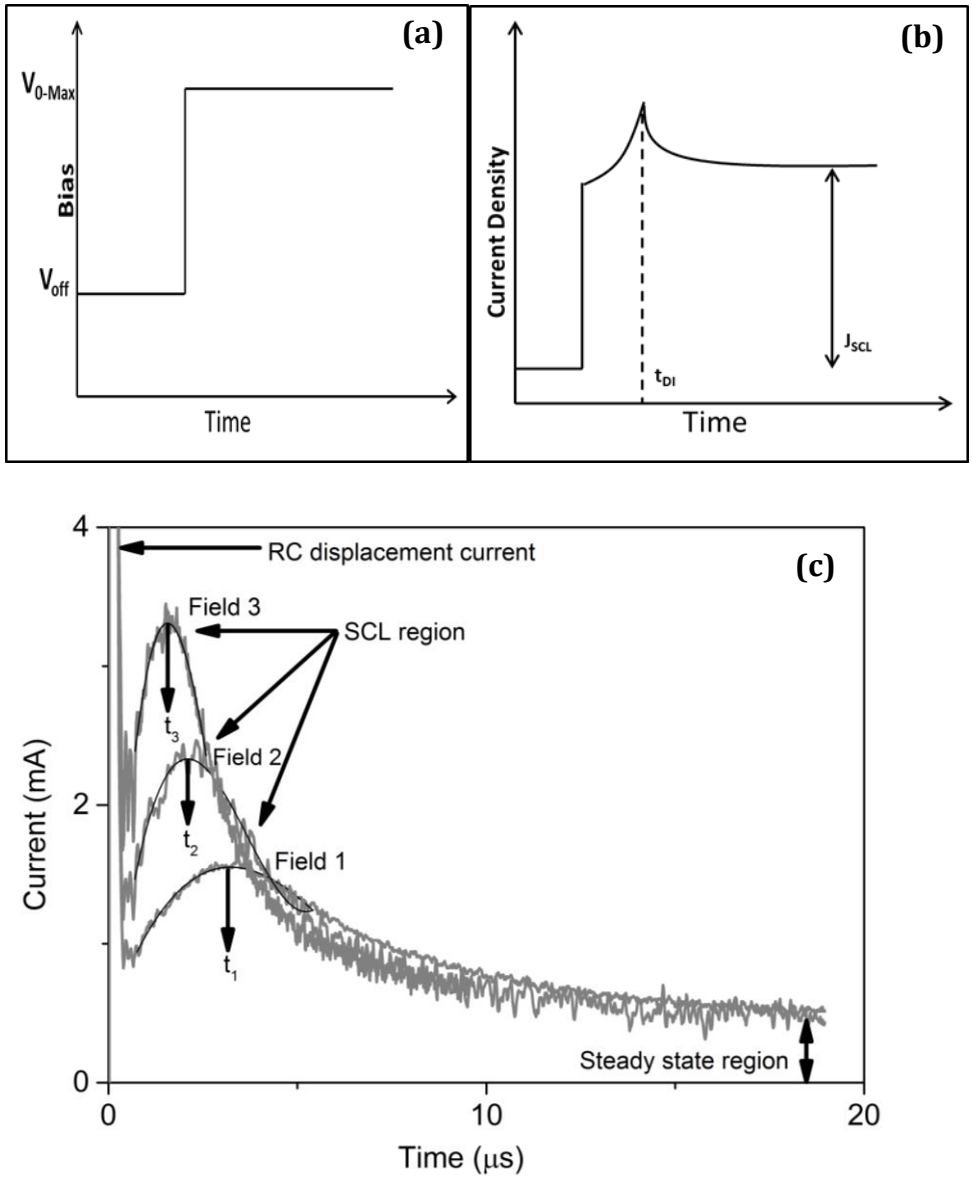

Figure 19. (a) Represents the use of offset bias V_{off} to generate excite states. (b) Representation of an ideal DI current. (c) illustrates typical experimental DI transients at different fields. Field 3 > Field 2 > Field 1. The corresponding transit times were found by differentiating the fitted peaks.

The transient current signal in an ideal system with no traps and ideal ohmic contacts as shown figure 19b, consists of three components. First is the Space Charge Limited (SCL) Current region. This is the useful part of the signal and is related to the ohmic nature of the injecting electrode in which a

maximum current is sustained within the sample. The peak represents the space charge transit time and corresponds to the arrival of the first carriers to the counter electrode. The reason for this behaviour is the non-uniformity of the electric field as the first sheet of charge carriers traverses the sample. There will be an additional electric field component generated by the carriers on top of what has already been applied. This results in a sharp increase in the electric field as more charge is injected into the sample which produces a peak until the carriers are extracted from the counter electrode.

The second component is the system's response after time t_{DI} and it corresponds to the extraction of carriers from the counter electrode resulting in a decrease in current density. This fall in current density continues until the rate at which the current is injected into the sample equals the rate at which it is extracted thus producing a steady state current. This corresponds to the third component of the graph. In an ideal system where no traps are present the peak occurs at approximately ($1.2 \times J_{SCL}$).

Experimentally however it is impossible to get such a 'cusp-like' DI transient. Our system would always produce some degree of diffusion broadening due to the presence of traps in the device. Some typical experimental DI transients corresponding to various electric fields are shown in figure 19c. Just like the ideal case we see the typical peak and the steady state region, however in both cases the two features do not quite resemble the ideal case. We can see that the peak is no longer a sharp 'cusp-like' shape, but is now broadened and that J_{SCL} can no longer be represented by (J_{peak} / 1.2), in fact J_{peak} is much greater than $1.2 \times J_{SCL}$, for example in figure 19c we can see that at field 3 the peak occurs around 3.5mA, at least 3 times

greater than the SCL current. This is clear evidence of trapping and is discussed further in section 9.4.

The non-uniformity of the electric field means that one can no longer use Eq. (5) to determine the mobility as t_{DI} is not a true representation of the transit time. However, further analysis have shown that assuming a trap free device, the space-charge-free transit time is given by $t_{DI} = 2(1 - e^{-1/2})t_{trans} \approx 0.786\ t_{trans}$ [65-66]. t_{trans} represents the experimental DI transit time used to calculate the true transit time of the carriers (t_{DI}).Thus $\mu = \frac{0.786\ d^2}{Vt_{DI}}$.

Another distinct feature of the experimental DI transient is the RC response of the circuit. This is due to the fact that the sample itself acts as a capacitor and needs a finite time to charge/discharge. One needs to take care when measuring transient currents using DI as a wrong combination of R and C can easily engulf the transit time. The width of the RC response is inversely proportional to the thickness of the sample, while the transit time is proportional to the thickness. This effectively means that there will always be a limit to the sample thickness. Hence unlike TOF this method can be very challenging when testing devices which are made with certain procedures such spin coating as there is very little control over the material thickness at the growth stage.

3.2.1 Bias Selection

Device biasing is paramount for measuring charge transport properties in organic semiconductors at the presence of excited states. Thus careful attention must be given to the choice of biases used. The objective is it to provide a constant stream of long lived excitons within the semiconductor so that injected polarons of particular type can readily interact with the excitons already present in the device. The strength of this interaction can then be determined by measuring the average mobility of injected carriers for a specified $V_{off}/V_{0\text{-}max}$ combination as shown in figure 16a. In other words $V_{0\text{-}max}$ is the dependent variable and V_{off} is the independent variable. The choice of V_{off} is predominantly limited by the maximum value of applied electric field, i.e. $V_{0\text{-}max}$. The maximum applied $V_{0\text{-}max}$ for a typical ITO/TPD(NPB)/Al structure of 500nm thick is in the range of 10-11V. A higher $V_{0\text{-}max}$ normally results in device breakdown. Thus the choice of V_{off} should be within this range. V_{off} should be chosen such that ($V_{0\text{-}max}$ - V_{off}) is a high as possible. This will ensure a suitable range for $V_{0\text{-}max}$ measurements. As the same time V_{off} should be large enough to provide a suitable concentration of exciton generation. This optimal condition can be identified by measuring the I-V characteristics of the device. Further details of the exact choice of V_{off} are provided in section 9.3.

Another objective of device biasing is to provide a varying concentration of excitons and to measure their effect on mobility of incoming polarons. This can be accomplished by varying the value of the applied bias and keeping the total value of applied $V_{0\text{-}max}$ constant. For example for 2V

offset bias, V_{off}=2V and $V_{0\text{-}max}$=8V, or for a 4V offset bias, V_{off}=4V $V_{0\text{-}max}$=6V. By increasing V_{off} a higher concentration of holes and electrons is injected into the device resulting in higher probability of exciton generation.

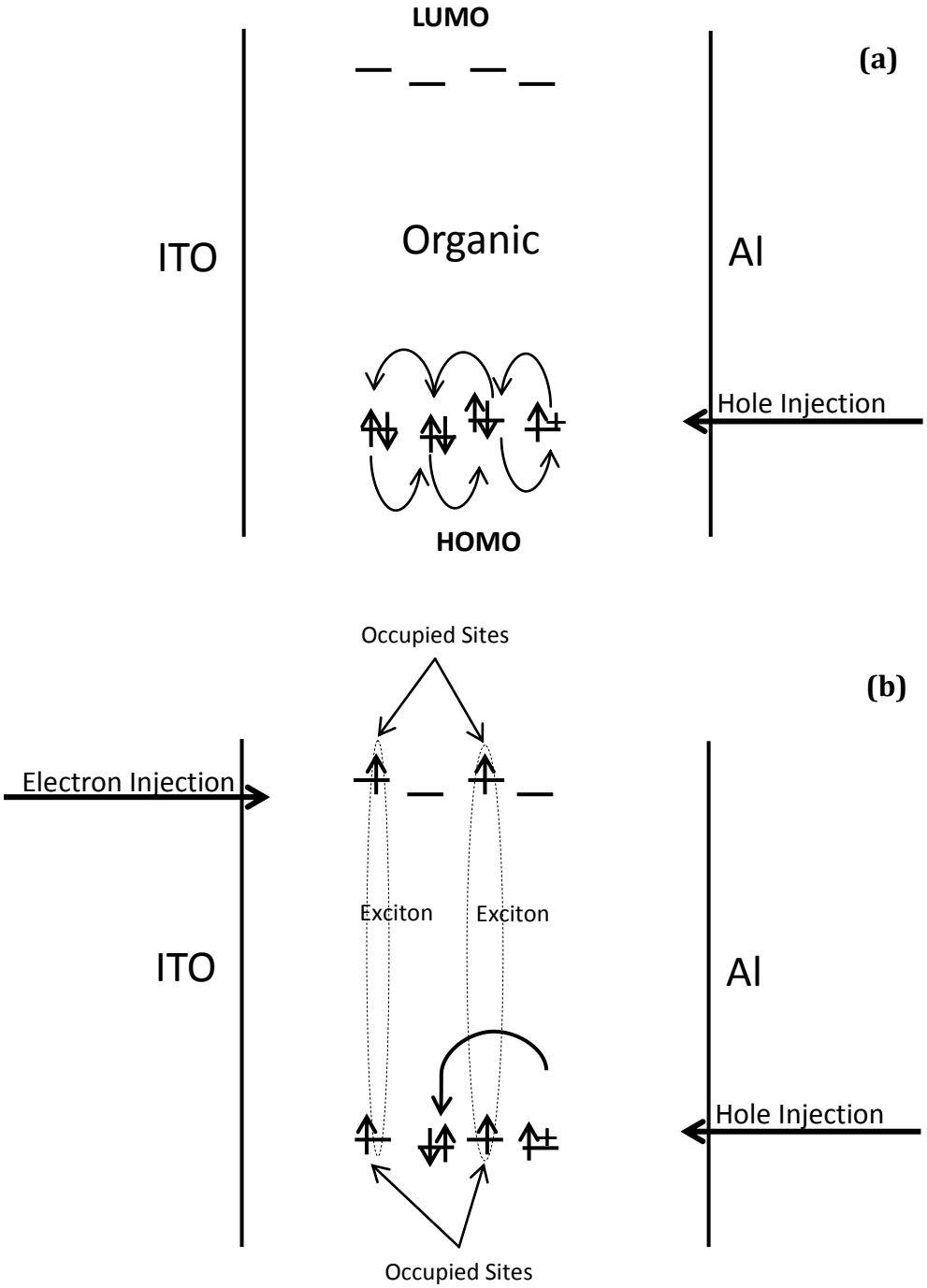

Figure 20. Schematic representing the transport of carriers with no exciton generation (a) and including exciton generation (b) as a result of offset bias. In (b) the polaron requires to overcome the excitonic barrier to hop onto the next available site.

The two experimental arrangements described provides us with a plaform to measure the effect of excitons on free charge carriers as a function of various experimental parameters such parameters such as temperature or magnetic field dependence.

3.3 Mott-Gurney Approach to Mobility

The Mott-Gurney approach to mobility is very similar to DI. The organic material is sandwiched between to ohmic electrodes and charge is injected into the bulk from one of the contacts. The excess charge generates a space charge region which opposes the total electric field applied to the sample. The induced space charge will reduce the total electric field at the injecting contact to zero when the excess charge is of the order of the capacitatively stored charge between the electrodes. Once this condition is met the SCL current can be described by Eq. (9). This maximum current (SCL) is limited by the maximum amount of charge that can be injected into the semiconductor, due to coulombic repulsion of charges already present in the sample.

$$j_{SCL} = \frac{9}{8}\frac{\varepsilon_0 \varepsilon \mu V^2}{d^3} \quad \textbf{(9)}$$

ε_0 and ε represents permittivity of free space and permittivity of material respectively. μ is carrier mobility, V and d are the voltage and sample thickness. This equation is known as the Mott-Gurney equation and allows the calculation of carrier mobility by measuring the current-voltage characteristics of the bulk. Note the quadratic dependence of the current with voltage. This

condition must be met for accurate mobility measurement and is based upon three assumptions:

- The presence of single type carriers. Injected charge carriers can either be p-type or n-type and not both.
- The existence of a constant dielectric permittivity ε .
- Electrodes used as contacts must be ohmic.

As discussed in section 3.2 without the use of an ohmic contact we cannot sustain an “infinite” reservoir of charge carriers in the semiconductor thus the quadratic relationship of $j_{SCL} \propto V^2$ would not hold.

3.4 Field Effective Transistor (FET) Characteristics

The mobility of an organic material can also be determined using a FET arrangement[67]. Figure 21 represents typical FET characteristics and arrangement. In this method the source and drain electrodes enable the source-drain current I_{SD} to be measured as a function of the gate voltage (V_g), applied perpendicularly to the gate insulator. The organic layer is insulated from the gate by a dielectric layer typically consisting of aluminum or silicon oxides. Organic dielectrics are also commonly used, specially for ‘top gate’ devices. Applying a voltage between the source and the drain (V_d) results in the current increasing with V_d and V_g. The mobility of carriers in the linear regime of the transistor is determined by Eq. (10).

$$\mu = \frac{L}{WC\ (V_g - V_T)} \frac{I_d}{V_d} \qquad \textbf{(10)}$$

C is the capacitance of the gate dielectric, W and L are the width and length of the conducting channel respectively. V_T is the threshold voltage at which the current starts to rise. The FET mobility is determined by charge carriers moving within a thickness of a few nanometers at the organic-dielectric interface. Hence the dielectric constant of the gate insulator has a significant impact on carrier mobility. For example mobility measurements of Ruberene crystals decreases with increasing dielectric constant[68] due to polarization effects produced across the interface.

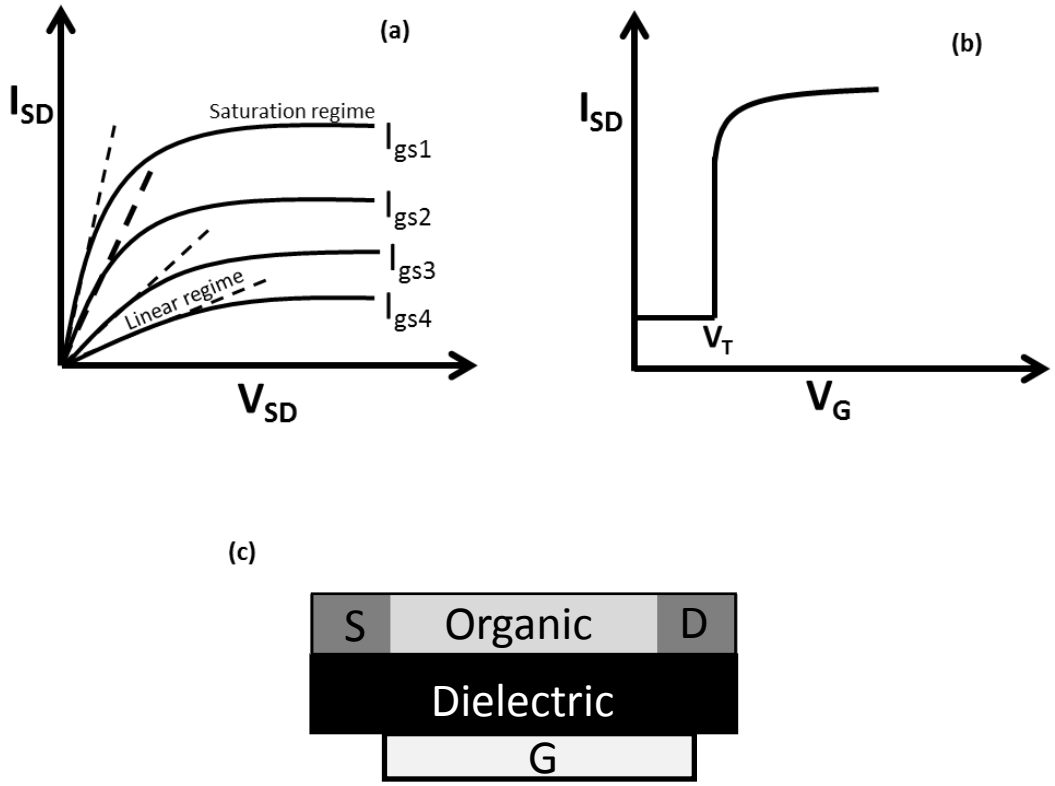

Figure 21. Illustration of typical FET characteristics (a) showing the behaviour of source-drain voltage-current at various gate-source voltages. $I_{gs1} > I_{gs2} > I_{gs3} > I_{gs4}$. (b) represents source drain current against gate voltage, illustrating the threshold position, V_T. (c) shows a schematic arrangement of a typical FET used for mobility arrangement.

4.0 Sample Preparation

4.1 Cleaning and Etching Procedures

Samples are prepared on ITO substrates with typical resistivity of ~20Ω/□. Prior to material deposition, substrates undergo a rigorous cleaning process in the following order:

1. Scrubbed with detergent and distilled water for 5 minutes
2. 20 minute sonication in detergent/distilled water solution
3. 3 × 5 minute sonication in distilled water only
4. 3 × 5 minute sonication in acetone
5. 3 × 5 minute sonication in chloroform

Once cleaned substrates proceed to the etching process to produce the desired lithographic pattern. This is achieved by spin coating a layer of photo-resist on the surface of the ITO at 7000 RPM for approximately 1 minute. The substrates are then exposed to UV light for a further minute via a mask with a particular pattern (see figure 22a). The next step in this process is to submerge the substrates into a solution of sodium hydroxide (NaOH) developer to remove any photo-resist that has been exposed to UV light. The ratio of NaOH and distilled water is 1:3. It is important to dilute the sodium hydroxide with distilled water as concentrated NaOH can damage the photoresist pattern entirely. The substrates are then placed into an etching solution consisting of 48% hydrochloric acid, 2% nitric acid and 50% distilled water at a constant temperature of 48°C for approximately 2 minutes. This particular step etches away any remaining ITO to form the correct pattern for

the anode electrode. The substrates are then given a final sonication bath in acetone to remove the photo-resist that is protecting the anode.

Once the etching is complete it is important for the substrates to undergo the entire cleaning process again (process 1-5) as the etching procedure would contaminate the substrates. Substrates are then oxygen plasma treated for 5 minutes to remove any unwanted molecular residuals on the surface of the ITO. The substrates are then immediately transferred to the vacuum chamber of the evaporation system for material deposition.

4.2 Device Fabrication

Material deposition is performed via the process of vacuum sublimation. Substrates are loaded into the evaporation system via a two-stage process. They are first inserted into a small vacuum chamber acting as a load lock. The load lock is then pumped down and once the pressure is similar to that of the main chamber, the main chamber valve is opened and the substrate is then inserted into the main vacuum chamber. Figures 22b and 14c show a schematic of the source arrangements. Typical load lock and main chamber pressures are in the range of 10^{-7} mbar.

Inside the main chamber there are 4 alumina crucibles for organic sublimation and 2 additional titanium di-boride metal sources for aluminum deposition. Adjusting the power to each crucible typically controls the evaporation, and a thickness film monitor provides feedback on the rate of evaporation. Once the desired rates are reached the main shutter separating the sources and the substrate is opened and evaporation takes place.

Evaporation rates are usually in the range of 2-3 Å/s for single layer TPD devices and consisted of 0.5 Å/s for $Ir(piq)_3$ and 10 Å/s for TPD during co-evaporation processes. Metal deposition usually starts at around 1 Å/s for 100Å, thereafter increasing to 10 Å/s for the remaining 400Å. This deposition arrangement is important to ensure good interface conductivity between the organic and the metal. 0.5μm of TPD is first deposited followed by 0.05μm of Al. It is important for the organic to be minimally exposed to the Al evaporation as the heat from the Al source can degrade the organic. Once the Al electrode is deposited the sample is then returned to the load lock ready for DI or TOF measurements.

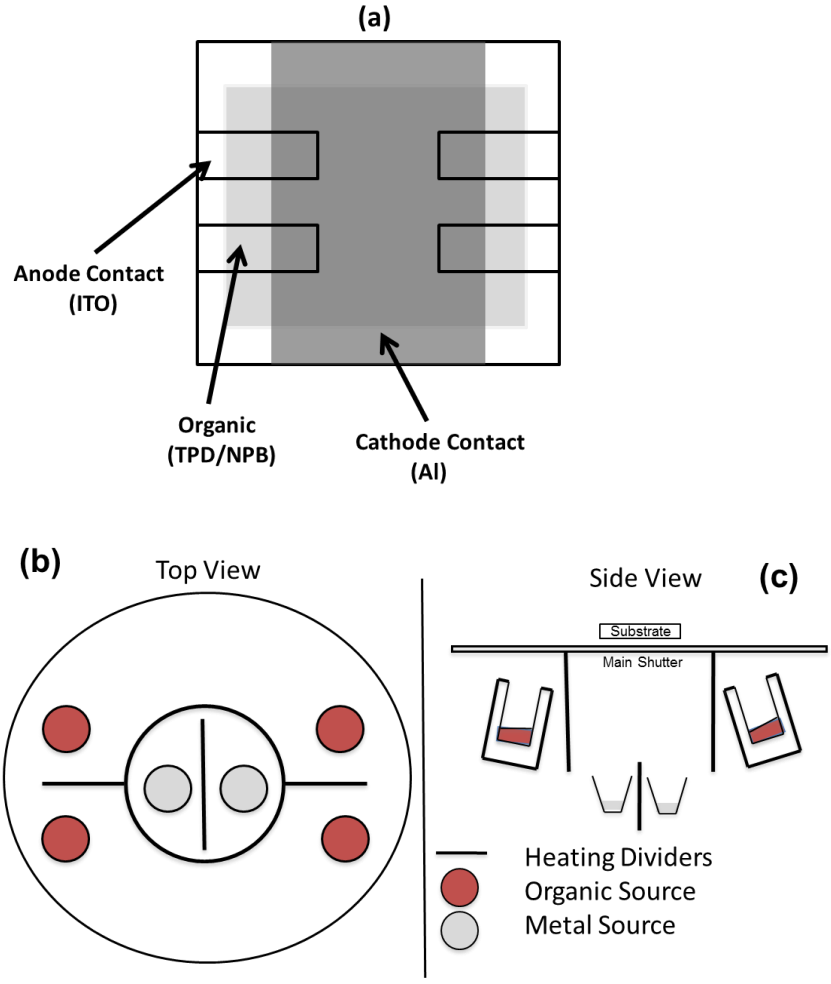

Figure 22. (a) Typical substrate used representing the lithographic pattern. (b) and (c) illustrate the heating source arrangements within the evaporation chamber.

5.0 Charge Transport Models

In general charge transport in organic semiconductors are grouped into two categories, the Gaussian Disorder Model and the Holstein Polaron Model. The Gaussian Disorder Model deals with disordered systems where no clear lattice configuration can be seen while the Polaron Model characterizes crystalline structures with specific lattice constants. The organic materials so far tested in this thesis (NPB and TPD) fall under the disordered category. Other hybrid models representing systems that are not completely disordered or completely crystalline have also been proposed. This section aims to give an overview of each model and some of their advantages and limitations. Particular emphasis is given to the Gaussian Disorder Model as it is the main model used to analyze the results in subsequent sections.

5.1 Gaussian Disorder Model

5.1.1 Miller-Abraham hopping rate

The behaviour of charge transport in most disordered organic semiconductors can be explained in relation to the Gaussian Disorder Model (GDM), developed by Bässler and co-workers[69-70]. The main feature of this model is its ability to replicate the so called Poole-Frenkel type carrier mobility seen in many disordered systems[71-72] .

Bässler assumes that the site energies within an amorphous organic system are distributed according to a Gaussian distribution, and that charge

carriers can hop between localized sites according to a Miller-Abraham's rule[73] shown in Eq. (11).

$$\mathrm{K}_{ij} = \nu \exp(-2\gamma R_{ij}) \begin{cases} \exp\left(-\dfrac{\varepsilon_j - \varepsilon_i}{k_B T}\right) & \varepsilon_j > \varepsilon_i \\ 1 & \varepsilon_j < \varepsilon_i \end{cases} \quad \textbf{(11)}$$

Eq. (11) is shown in its general form with respect to a crystalline lattice. K_{ij} is the hopping rate between sites i and j, and ν represents the attempt-to-escape frequency. The jump distance between sites i and j is R_{ij} normalized to the intersite distance, a, i.e. the lattice constant and γ characterizes the electronic coupling between adjacent sites. k_B, T and ε corresponds to the Boltzman's constant, temperature in Kelvin and site energies respectively

In the absence of a lattice constant in amorphous materials, the intersite distances are not spherically symmetric. Hence, the overlap parameter, $2\gamma R$, is usually replaced by Σ representing a Gaussian distribution of spatial disorder. Experimental values show that Σ is usually greater than 1.5[74]. In the presence of an applied electric field, the site energies in Eq. (11) can be expressed as $(-\varepsilon r E)$, where r is a vector connecting the centre of two sites, E is the applied electric field vector and ε is the electronic charge. Note that from Eq. (11) a jump upwards in energy is supported by $k_B T$ and a jump downwards is 1 and is independent of the electric field.

In addition to Σ, energetic disorder, σ, should also be accounted for within the system. This is usually represented by attributing each site with an energy ε, picked randomly from a Gaussian distribution given by Eq. (12).

$$Q(\varepsilon) = \frac{1}{\sqrt{2\pi\sigma^2}} \exp\left(-\frac{\varepsilon^2}{2\sigma^2}\right) \quad \textbf{(12)}$$

Note that the disorder parameter (σ) is technically the standard deviation of the Gaussian graph and can be used to calculate the width of the distribution. Experimental values of σ are in the range of 50-150meV[75]. By replacing ε with Σ in Eq. (12) we can also represent the variation of intersite distances as a Gaussian distribution.

5.1.2 The model

Once the parameters of the Miller-Abraham equation are determined and the disorder parameters are set, Monte Carlo simulations are used to derive an empirical expression for the charge carrier mobility as a function of electric field (E) and temperature (T). For Σ > 1.5 a universal law for charge carrier mobility as expressed by Bässler [69] is shown in Eq. (13).

$$\mu(T,E) = \mu_0 \exp -\left(\frac{2\sigma}{2k_BT}\right)^2 \exp\ C_0\sqrt{E}\left(\left(\frac{\sigma}{k_BT}\right)^2 - \Sigma^2\right) \quad \textbf{(13)}$$

In this equation the mobility μ_0 is the hypothetical mobility at zero field and infinite temperature and C_0 is a numerical constant. The remaining parameters have their usual meanings. A schematic representation of this equation is shown in figure 23.

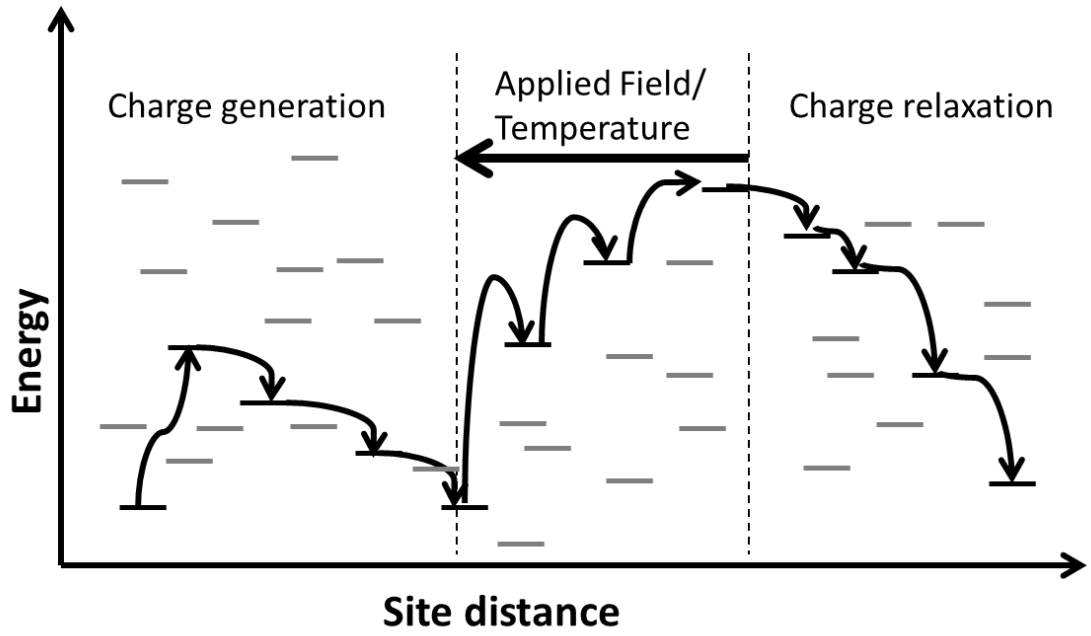

Figure 23. Schematic representation of the GDM model showing the generation and transportation of charge and the dispersion of the energetic sites.

In this equation C_0 is calculated to be 2.9x10^{-4} cm/V$^{1/2}$ for a lattice constant of 0.6nm, which is typically observed in molecular crystals. From Eq. (13) the following conclusions can be drawn:

- The relaxation of charge carriers starting at an arbitrary point within the DOS exhibit a logarithmic decay law and tend to decay towards the tail of the DOS.
- The natural log of the mobility is directly proportional to the square root of the electric field ($\ln \mu \propto \sqrt{E}$), for fields greater than 10^5 V/cm. This is a particularly powerful derivation as it explains the typical Poole-Frenkel type behaviour experienced by most organic disordered materials.
- The mobility increases with temperature, which is again a very common feature seen in amorphous organic semiconductors.

5.1.3 Extrapolation of GDM Parameters

GDM parameters can easily be extracted via a poole-frenkel plot ($\sqrt{E}$ versus $\ln \mu$) of mobility data obtained from experiment. Figure 24 gives a schematic of a typical poole-frenkel plot parametric in temperature.

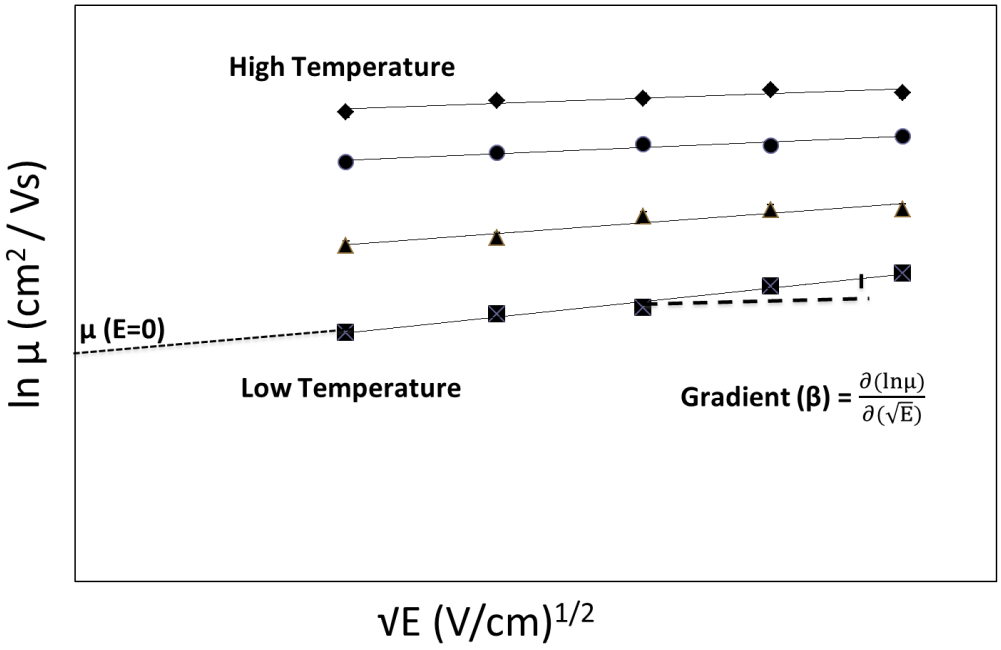

Figure 24. Poole-Frenkel plot for calculating $\mu(T, E = 0)$ for various temperatures.

From Eq. (13) when $E = 0$, the equation reduces to:

$$\mu(E = 0) = \mu_0 \exp -\left(\frac{2\sigma}{3k_B T}\right)^2 \quad \textbf{(14)}$$

Or

$$\ln \mu(E = 0) = \ln \mu_0 - \left(\frac{2\sigma}{3k_B T}\right)^2 \quad \textbf{(15)}$$

Hence, the mobility (μ) at $E = 0$ is simply the y intercept of each of the temperature graphs. Furthermore we can now determine μ_0 and σ via a plot of $\ln \mu(E = 0)$ versus $1/T^2$ as shown if figure 25.

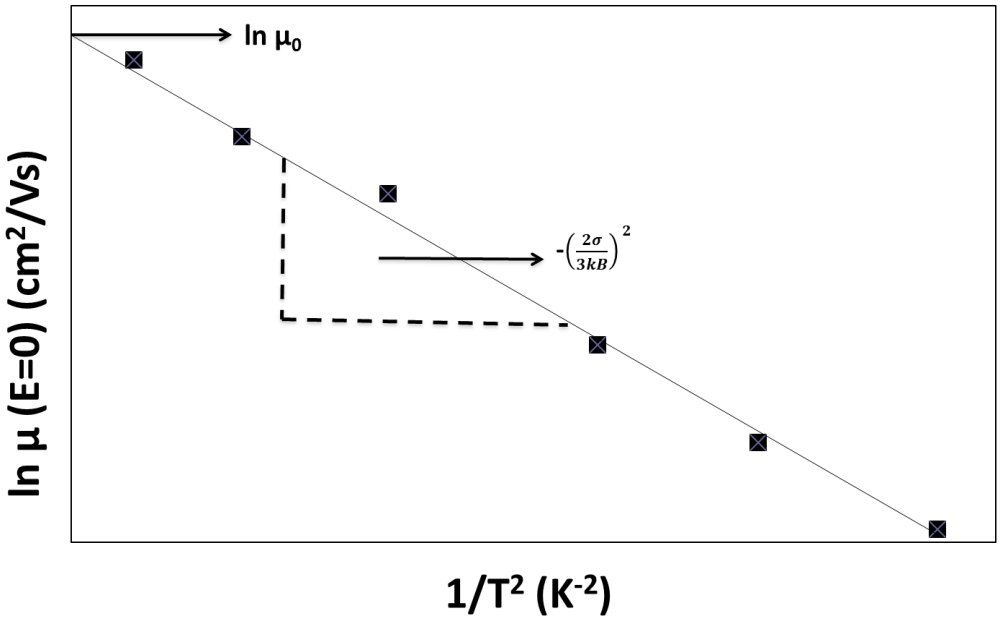

Figure 25. Typical plot of zero field mobility for calculating the energetic disorder (σ).

From figure 25 the gradient of the line corresponds to $-\left(\frac{2\sigma}{2k_BT}\right)^2$ and the y intercept refers to $\ln(\mu_0)$. In order to find the remaining parameters, Σ and C_0 we take the natural log of Eq. (13):

$$\ln(\mu) = \ln(\mu_0) - \left(\frac{2\sigma}{2k_BT}\right)^2 + C_0\sqrt{E}\left(\left(\frac{\sigma}{k_BT}\right)^2 - \Sigma^2\right) \quad \textbf{(16)}$$

And differentiate with respect to $\sqrt{E}$:

$$\frac{\partial \ln(\mu)}{\partial(\sqrt{E})} = -\Sigma^2 C_0 + C_0\left(\frac{\sigma}{k_BT}\right)^2 \quad \textbf{(17)}$$

From Eq. (17) we can see that $\frac{\partial \ln(\mu)}{\partial(\sqrt{E})}$ is simply the gradient (β) of our original poole-frenkel plot in figure 25. Thus a plot of $\frac{\partial \ln(\mu)}{\partial(\sqrt{E})}$ against

$\left(\frac{\sigma}{k_B T}\right)^2$ would typically yield a straight line where by the remaining parameters can be computed as shown in figure 26.

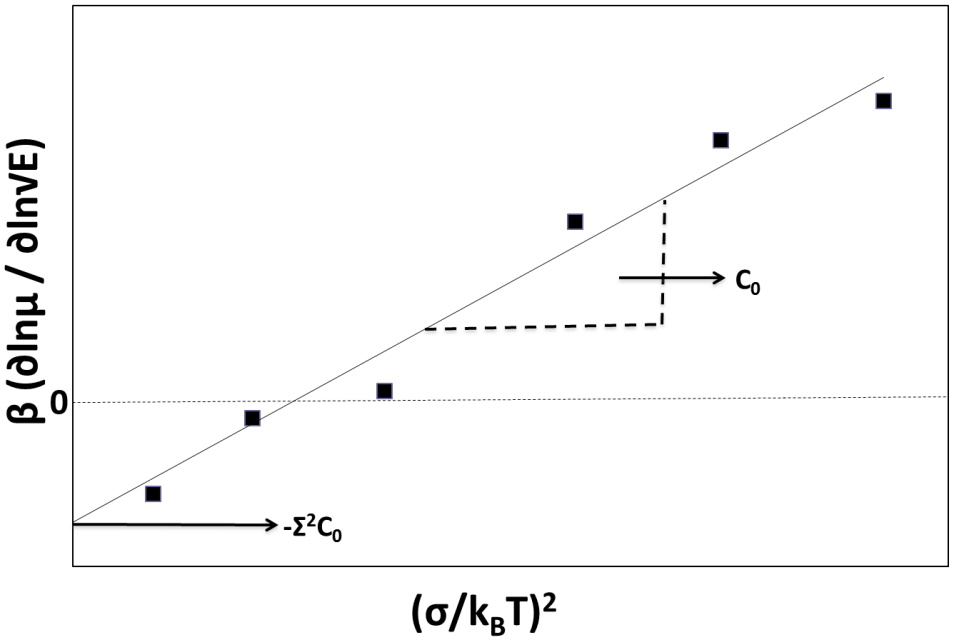

Figure 26. A typical plot of β vs $\left(\frac{\sigma}{k_B T}\right)^2$. Here the y intercept corresponds to $-\Sigma^2 C_0$ and the gradient to C_0.

5.1.4 Limitations of GDM

One of the main limitations of GDM is the deviation from the Pool-Frenkel type behaviour for fields less than 10^5 V/cm. This comes about as the empirical formula developed for carrier mobility in Eq. (13) is derived from simulations of the Miller-Abraham's hopping rate and only illustrates a linear relationship with $\sqrt{E}$ for fields greater than 10^5V/cm. This is to the contrary to what is seen from experimental data where the mobility typically exhibits a Poole-Frenkel law down to fields of $8\text{x}10^3$ cm^2/Vs[76]. Such a discrepancy occurs due to the independence of each energetic site, i.e. it is assumed that

there is no correlation or coupling between adjacent sites. Such an assumption is not entirely true as there is usually some level coupling between neighboring sites. This phenomenon is discussed in greater detail section 7.1 with respect to the Correlated Disorder Model.

Another limitation of this model is the lack of direct experimental proof for the Gaussian distribution of σ . The only justification comes from the shape of the absorption bands. Although experimental and simulated results are in good agreement, one needs to be cautious when modeling this parameter, as there seems to be no clear consensus behind such a choice. The same argument applies to the spatial disorder.

One other drawback of the GDM is that it's based on the assumption of perfectly pure materials. In reality achieving such a high level of purity is very difficult and inevitably all systems will have some degree of impurity, leading to the formation of traps. Charge carriers are susceptible to these traps and it has been shown that carrier density can also have an impact on the overall mobility[57]. Such a phenomenon is not accounted for in the GDM and can potentially be crucial when modeling for systems with a high level of trapping.

5.1.5 Summary of GDM

Figure 27 illustrates the different processes involved to obtain carrier mobility with the GDM model. We first assume a perfect crystal with specific lattice constant. Spatial and energetic disorder parameters are then added as a function of a Gaussian distribution. Monte Carlo simulations are then used to simulate the different pathway scenarios that

a carrier can take under a variety of temperatures and electric fields. The current transient that is produced as a result of a moving carrier is then used to calculate the mobility. Such a derivation is very useful to experimentalist investigating the transport properties of disordered organics. The mobility of carriers as a function of T and E can easily be measured and comparison between theory and experiment can be made.

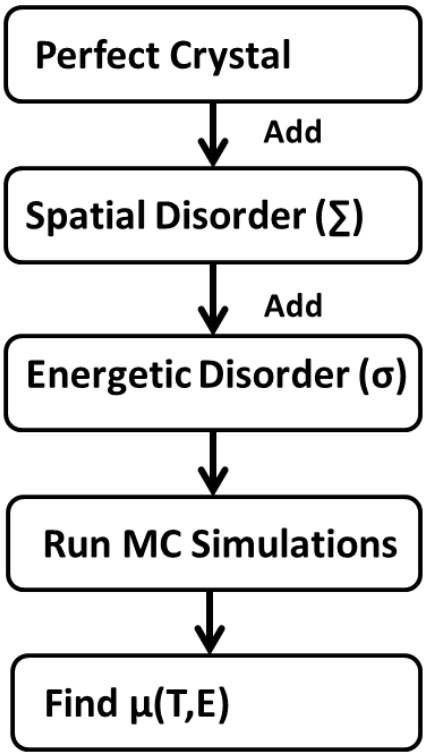

Figure 27. Summary of the processes involved to obtain carrier mobility with respect to the Gaussian Disorder Model.

6.0 Polaron Model

The Polaron approach characterizes carrier transport in crystalline organic materials where a distinct lattice constant can be observed. In this model the mobility of charge carriers depends on the degree of intermolecular and intramolecular forces as opposed to energetic and spatial disorder. The latter can be related to the change in molecular structure upon addition or removal of a charge while the former corresponds to the strength of chemical bonds within individual molecules. Extensive research in this field has shown that intramolecular forces are the dominant feature in organic crystals. Hence understanding this parameter is key when modeling charge transport in ordered organics.

6.1 Electron-Phonon Coupling

Electron-phonon coupling can be seen as a form of intramolecular effects. Once an exciton is created it is thought to rapidly couple with localized lattice vibrations (phonons), resulting in the formation of a localized polaron state. This phenomenon is usually referred to as electron-phonon coupling and manifests itself as polaron binding energy. Quantum chemical calculations show that typical polaron binding energies in organic molecular crystals range from 50meV to 200meV[77].

The most detailed transport theories for predicting the effects of electron-phonon coupling are those based on Holstein's Polaron Model

(HPM). In this model the total mobility of a system is expressed as a sum of tunneling mobility (μ_{tun}) and hopping mobility (μ_{hop}) as shown in Eq. (18).

$$\mu_{total} = \mu_{tun} + \mu_{hop} \quad \textbf{(18)}$$

μ_{tun} refers to mobility with respect to electronic coupling (the transfer integral) whilst μ_{hop} represents electron-phonon contributions. A mathematical representation of Holstein's model is given in Eq. (19)[78-79].

$$\mu(T, E \rightarrow 0) \propto \exp\left(-\frac{E_p/(2-j)}{k_B T}\right) \quad \textbf{(19)}$$

In this equation, j is the electronic transfer matrix, i.e. the electronic coupling. E_p is the polaron binding energy and the rest of the parameters have their usual meanings. The term $E_p/(2-j)$ corresponds to the compromise between tunneling of a charge carrier and thermally activated hopping transport. If j is large compared to E_p, the carrier does not feel any lattice deformation, hence the polaronic effects become negligible and charge transport is solely diffusive. On the other hand if $E_p >> j$, hopping is the main mode of transport due to a high level of electron-phonon coupling.

The relative contributions of each effect are shown graphically in figure 28 as a function of temperature dependent mobility. For weak electron-phonon couplings, the mobility solely depends on the tunneling effects and displays a band like temperature dependence ($\mu \propto T^{-n}$, where $n > 0$). This effect is usually observed in crystalline inorganic semiconductors where the electronic coupling between adjacent sites are the dominant feature. For intermediate electron-phonon couplings, mobility is band-like at low temperatures, but starts to exhibit hopping contributions at higher

temperatures. On the other extreme, for strong electron-phonon couplings three distinctive regimes are observed. At low temperatures ($T << T_1$), the mobility is band-like. As the temperature increases the hopping term starts to dominate and the mobility exhibits a crossover from band-like to hopping transport. At very high temperatures ($T > T_2$) the thermal energy of the system would be greater than the binding energy of the polaron, hence the polaron dissociates resulting in a free charge carrier.

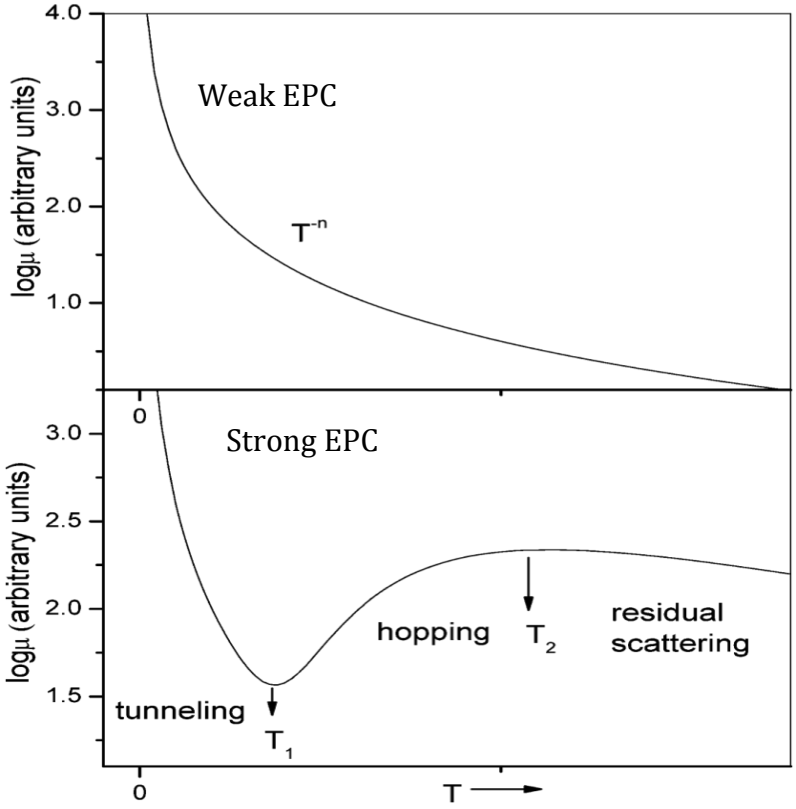

Figure 28. Temperature dependence on carrier mobility predicted by the Holstein polaron model for cases of strong and weak electron-phonon coupling (EPC).

6.2 Summary of the Polaron model

Figure 29 illustrates the processes involved to obtain the carrier mobility using Holstein's polaron model. Similar to the GDM model we start with a perfect lattice and we add or remove an electron. This will produce lattice deformation which can be measured as current fluctuations producing time transients that allow carrier mobility to be measured. The degree of lattice deformation depends on the dominance of electron/phonon and electronic coupling. Just as with the GDM model the ability to theoretically predict the mobility of carriers as a function of T and E is very useful as it is a parameter that can be easily measured experimentally.

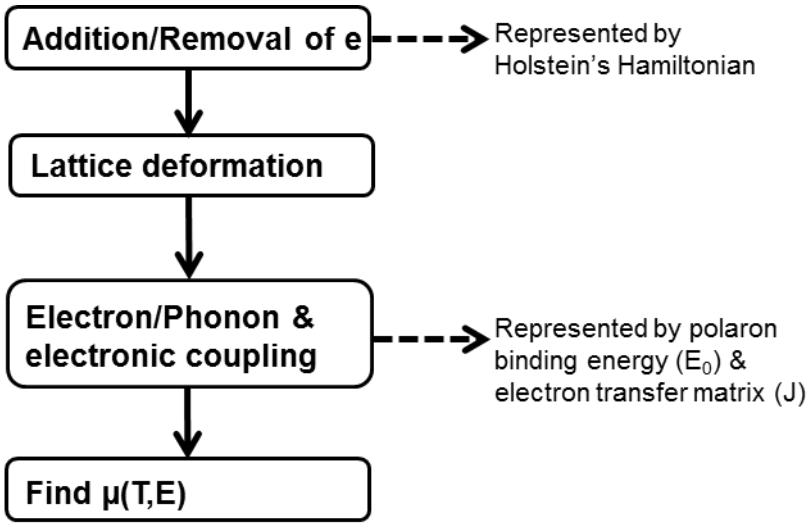

Figure 29. Summary of the processes involved to obtain carrier mobility using Holstein's polaron model

6.3 Limitations of the Polaron Model

The polaron model assumes perfect crystalline structures. In practice most crystalline materials have some level of disorder and this should be accounted for in the model. One approach is by assuming that the energies for polaron and disorder induced hopping motion is additive as shown in Eq. (20).

$$\mu(T, E \to 0) = \exp\left(-\frac{E_p/(2-j)}{k_B T}\right)\exp\left\{-\left(\frac{2\sigma}{3k_B T}\right)^2\right\} \quad \textbf{(20)}$$

Differentiating Eq.20 with respect to $1/T$ shows that temperature dependent activation energy is required.

$$\frac{\partial \ln(\mu/\mu_0)}{\partial(1/T)} = (E_p/2) + \left(\frac{8\sigma^2}{9k_B T}\right) \quad \textbf{(21)}$$

Energetic disorder in Eq. 21 is derived from the Miller-Abraham hopping rate discussed in section 5.1.1 It neglects any polaron coupling and hence polaron contributions are only treated as perturbations[80].

A more comprehensive approach is proposed by Fishchuk[81] via the Effective Medium Theory (EMT). However this approach does have its limitations as well and is discussed in greater detail in section 7.2.

Another limitation is the model's difficulty to differentiate between tunneling effects and hopping motion when the available temperature interval is small. Although figure 28 shows a clear transition from tunneling to hopping, differentiating between these two effects are very difficult at small temperature margins. Over the years there have been many attempts to distinguish between these two effects. One approach that has shown considerable

interest is via the adiabatic small polaron hopping model developed by Daven Emin[82]. It is based upon the fact that the intersite distances are sufficiently small to allow adiabatic carrier motion, hence carrier jumps are independent of intersite distance. The difficulty with such models is that most are theoretical models based on crystalline inorganic systems with limited experimental evidence.

7.0 Other Proposed Models

GDM and the Polaron model seem to be the two main dominant models for describing charge transport in organic systems. However, depending on the mobility results obtained from various groups, a range of other models have been proposed. Most, can be regarded as an offshoot from the models discussed in sections 5 and 6. This section aims to briefly discuss these models and some of their limitations.

7.1 Correlated Disorder Model (CDM)

CDM can be seen as a hybrid system between GDM and the Holstein's Polaron model. Gartstein and Conwell showed that depending on the value of the disorder, there will always be a weak correlation between neighboring sites[83]. Further analysis by Dunlap, Kenkre and Novikov managed to incorporate this correlation within the GDM[84]. The essence of this model is effectively identical to the GDM except for the inclusion of site correlations (σ_d), which corresponds to dipolar disorder within the system, and Γ, which

is the equivalent of Σ in the GDM. R is the hopping distance. One example of this type of behaviour can be seen in PFO[54]. CDM in its general form is shown in Eq. (22).

$$\mu(T,E) = \mu_0 \exp\left(-\frac{3\sigma}{5k_BT}\right)^2 \exp\left\{C_0\sqrt{\frac{eER}{\sigma_d}}\left[\left(\frac{\sigma_d}{k_BT}\right)^{\frac{3}{2}} - \Gamma\right]\right\} \quad \textbf{(22)}$$

7.2 Effective Medium Theory (EMT)

EMT can be regarded as an extension to the GDM by taking into account the effect of impurity or charge trapping within the system[85-86]. In this approach, two adjustments are made to the original GDM. The first is the introduction of another disorder parameter (σ_t) representing a Gaussian distribution of charge traps within the material. The second is the averaging of the Miller-Abraham jump rates in the presence of an electric field, effectively assigning an average intersite distance. One limitation of this model is that it is only valid for low concentrations of traps[85].

7.3 Los Alamos (LA) approach

The LA model can be seen as another hybrid model. In GDM a single σ parameter is assigned to a disordered system. In the LA approach Yu and co-workers[87-88] proposed a variation of σ depending on the temperature. The main difference between this approach and the GDM is the $1/T$ dependence on temperature as compared to $1/T^2$ in GDM. However, this model also

seem to lack some solid experimental evidence as shown by Kreouzis and co-workers[26]. This is particularly evident for materials that are partially ordered. In some instances, at low temperatures, a very weak field dependence or even negative field with respect to mobility has been observed[87].

8.0 Ambipolar Behaviour of NPB and TPD

8.1 Introduction to Ambipolar Transport

In some organic semiconductors, both electrons and holes can be injected and transported with similar mobilities, an effect known as ambipolar charge transport. Ambipolar transport materials are becoming increasing popular in organic semiconductors. An ambipolar OLET would allow the electron-hole balance as well as the location of the recombination zone between source and drain to be tuned by the gate voltage, hence improving the quantum efficiency of light emission per injected charge. As discussed in more detail in section 8.2, ambipolar charge transport arises as a result of matching the energetic barriers of the work functions of the electrodes and the HUMO and LOMO layers of the organic.

One of the most popular ambipolar materials used in the literature is Phthalocyanines (Pcs) and its derivatives. They have been used in solar cells, optical limiters, and photoconductors with mobilities in the range of 0.11 cm^2/Vs[89]. Derivatives of Pcs have electronic levels that can be shifted in a wide range by appropriate substitution with electron-withdrawing ligands, with heteroatoms, or with electron-withdrawing substituents like chlorine or fluorine

atoms to their outer rings[90]. Recently it has been shown that PCBM has also ambipolar transport characteristics[91].

One method of adjusting the energy levels of organics is through doping or by incorporating thin layers of other organics within the semiconductor structure. However this method can significantly impact the I-V characteristics of OLEDs or the source/drain current for OFETs and OLETs. For some polymers however this limitation can be solved. Research by Cambridge group have shown that ambipolar transport in PPV[92] can be achieved by including a thin layer of BCB in the structure. The idea is that BCB can act as charge traps between the interface of the electrode and the organic leading to the formation of interface dipoles and the reduction of electron injection barriers in the structure.

TPD is also another material that is extensively used OLED structures and can possess ambipolar properties despite the fact that it is widely regarded as hole transporter. Campbell *etal* have shown that by measuring the I-V characteristics of a device constituting of ITO/TPD/AL[15], we can observe some measure of light output. Although the transport characteristics of the carriers involved were not studied in great detail, it provides evidence that there must be some level of electron/hole injection within the device. Transport properties of TPD and their efficiencies in transporting electrons are further studied in section 8.3. Strong ambipolar behaviour has also been reported in P3HT by the Imperial group, with room temperature mobilities of 3×10^{-4} cm^2 V^{-1} s^{-1} and 1.5×10^{-4} cm^2 V^{-1} s^{-1} for electrons and holes respectively[24].

8.2 Why Study Ambipolar Behaviour of NPB and TPD?

The experimental work in this thesis mainly revolves around two widely used organic materials, NPB and TPD. Both have been exclusively labeled as hole transport (HT) layers in the literature and are extensively used in a variety of different structures, be it in OLEDs[2], OPVs[6] or FETs[11].

Whether materials are labeled HT or electron transporters (ET) comes about as a result of the energetic barrier between the HOMO and LUMO of such materials and the work function of the electrodes. For example in a typical ITO/TPD/Aluminium hydroxyquinoline (Alq_3)/Al OLED, the energetic barrier between the LUMO of TPD and the work function of the ITO is approximately 2.3eV. It is assumed that a large energetic barrier is sufficient to stop electron injection into the structure. As a result extensive charge transport models have been developed to predict the behaviour of holes in such materials ignoring completely the effect of electrons.

This chapter predominantly aims to look at the intrinsic transport properties of such materials irrespective of the injection barriers. An extensive overview of the transport properties of both holes and electrons in NPB and TPD and an analysis using the GDM model are presented. We show that in addition to the energetic barrier, a thorough understanding of the intrinsic behaviour of such materials is paramount for modeling the transport properties of such materials.

8.3 Early Evidence of Ambipolar Behaviour in Unipolar Devices

It can be shown that OLEDs fabricated from solely HT layers such as ITO/TPD/Al can produce light emission with current/voltage luminescence characteristics similar to that of a classic HT/ET OLED. Figure 30 shows current voltage and electroluminescence characteristics of a single 500nm TPD layer with ITO anode and aluminum cathode. We can clearly see that the emission follows the IV characteristic of the device. The ability to detect light emission is a testament to the fact that there must be some excitons formed within the HT layer, that they radiatively decay, and for excitons to be formed there must be some level of electron injection in the system. Hence the next logical step is to investigate the transport behaviour of both electrons and holes within such “traditional” HT materials.

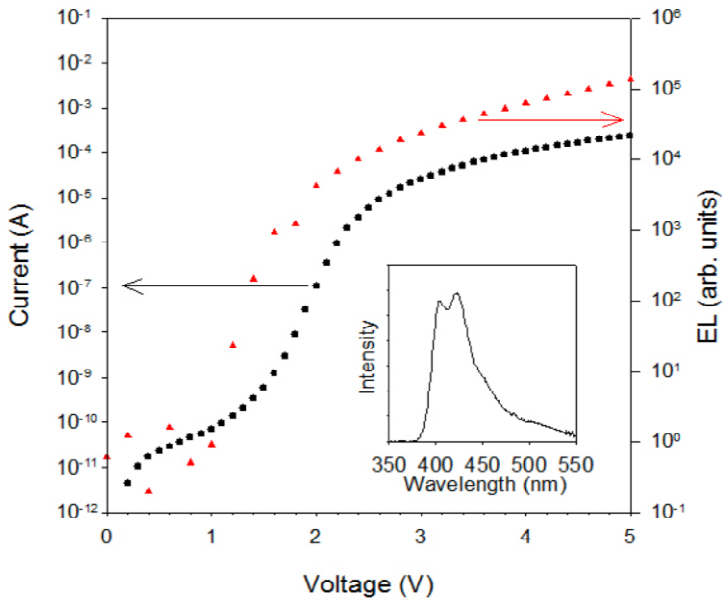

Figure 30. Current, Voltage and electroluminescence characteristics of a single layer (500nm) TPD device. Inset shows electroluminescence spectrum of the device.

8.4 TOF Photocurrents

Transport properties of electrons and holes in NPB and TPD were obtained by measuring the absolute mobility of the respective carriers via the TOF technique. Experiments for electron and hole mobilities were carried out on a single ITO/organic (600nm)/Al (50nm) sample fabricated via vacuum sublimation.

8.4.1 Hole and Electron Photocurrents in NPB

Figure 31 shows typical room temperature photocurrent transients for electrons and holes in NPB. Figures 31a and 31b demonstrate the low dispersion nature of NPB hole photocurrents at varying bias and illustrate the expected scaling for the transit time. For example for a 600nm sample the hole arrival time is increased from 1.03μs at 167kV/cm to 2.17μs at 100kV/cm. The thickness dependent arrival times show a similar trend. For example from figure 31b we can see results from two NPB samples of 600nm and 1200nm produced from the same batch of material. When a constant electric field of 75kV/cm is applied we see an increase in the hole arrival time from 0.95us for the thinner sample to 1.75μs for the thicker sample, as would be expected for holes traversing the entire thickness.

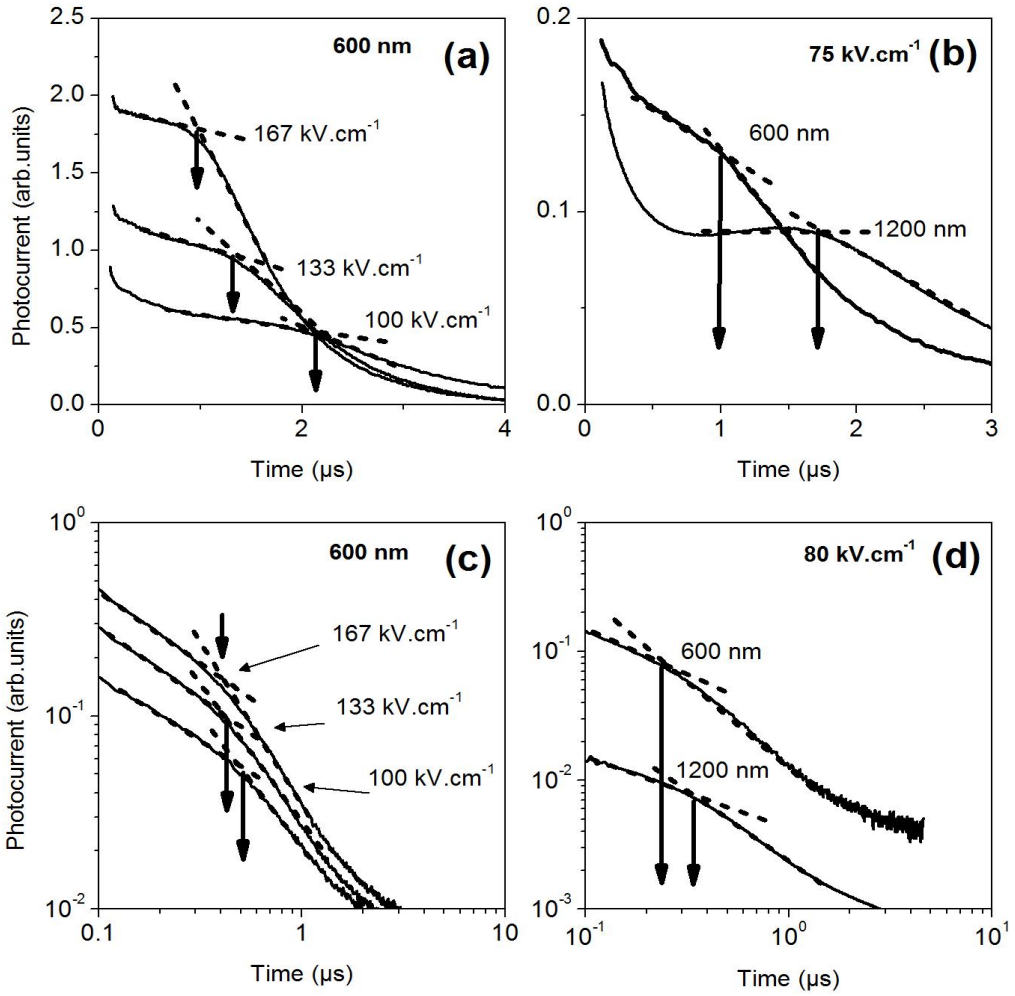

Figure 31. Typical photocurrent transients for NPB at room temperature. Panels (a) and (b) are hole transients and (c) and (d) are electron transients. The transit time is indicated by an arrow for each photocurrent.

Figure 31c illustrates the dispersive nature of the electron photocurrent transients in NPB for varying electric fields. Arrows on the double logarithmic plot show the inflection point arrival time and again show the expected scaling with respect to electric field. For example from 0.30μs at 167kV/cm to 0.48μs at 100kV/cm. Figure 31d shows the thickness dependent arrival time for electrons in NPB at constant electric field (80kV/cm). Again, similar to holes, there is an increase in the arrival time for thicker sample, from 0.28μs in 600nm to 0.38μs in 1200nm.

8.4.2 Hole and Electron Photocurrents in TPD

Just as the case of NPB, similar behaviour can be observed in TPD. We can see from figure 32 the expected scaling of the arrival time with both electric field and thickness. For example figure 32a illustrates the arrival times of hole photocurrents with respect to electric field and shows an increase from 0.52μs at 29kV/cm to 0.81μs at 18kV/cm. An increase in hole arrival time also observed with varying thickness as shown in figure 32b, from 0.95μs for the 500nmsample to 1.75μs for the 1700nm sample.

The electron photocurrent also scales as expected with electric field from 0.73μs at 110kV/cm to 0.93μs at 55kV/cm as shown in figure 32c. Similar to the hole case we can also see an increase in the arrival time for electrons in TPD for a constant electric field of 110kV/cm with respect to thickness as demonstrated in figure 32d, from 0.73μs (500nm sample) to 15.4μs (1700nm sample).

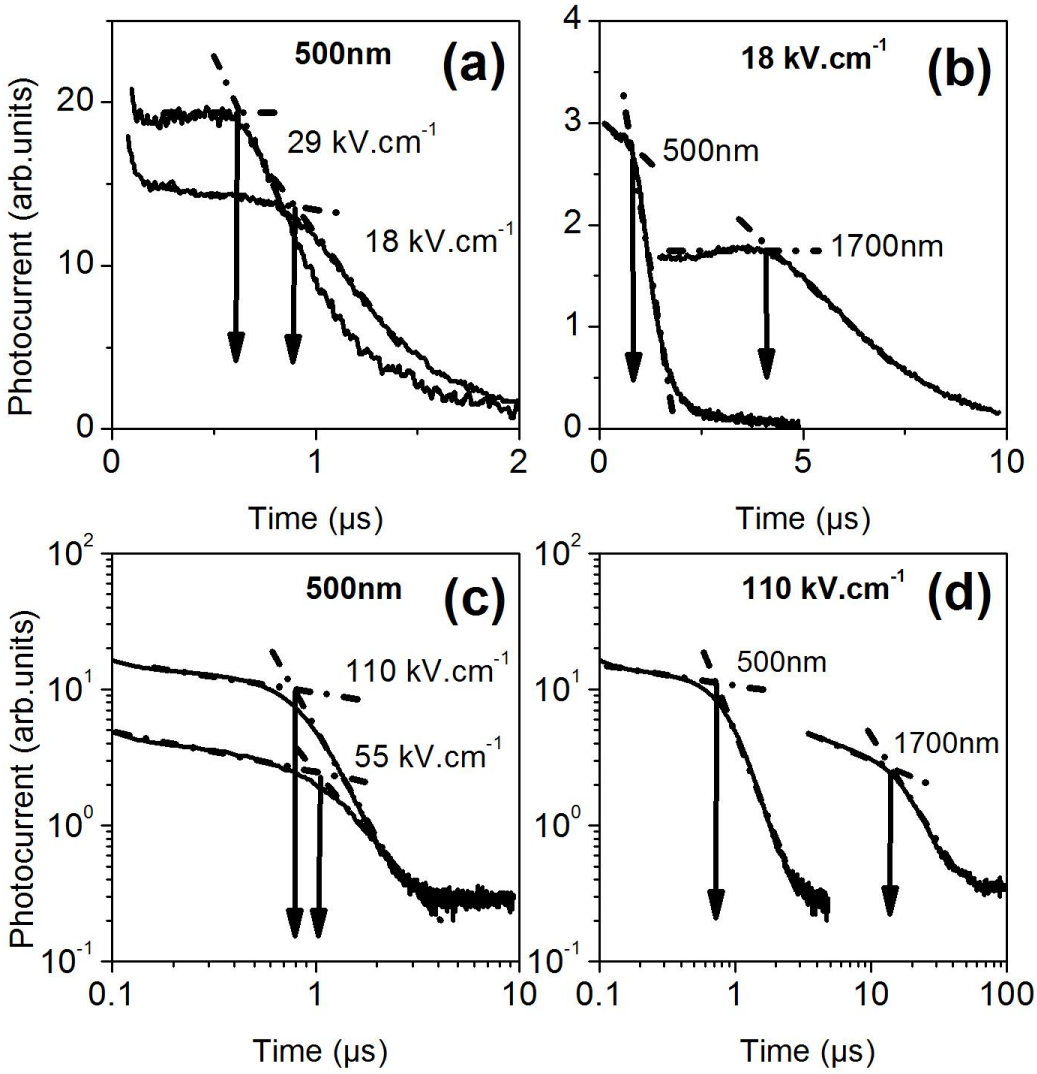

Figure 32. Typical photocurrent transients for TPD at room temperature. Panels (a) and (b) are hole transients and (c) and (d) are electron transients. The transit time is indicated by an arrow for each photocurrent.

8.5 Elimination of Space Charge Effects

As discussed in section 3.1.6, it is important to ensure that the photocurrents observed are free of any space charge effects. The presence of any space charge effect will alter the resultant electric field within the sample, which can distort the arrival times of our carriers leading to inaccurate mobility measurements.

There are generally two methods that can be used to avoid this effect. The first is through simple observation and the second is through numerical integration. The method of observation can be particularly useful for non-dispersive photocurrents where a flat plateau is observed such as hole transport in NPB and TPD. An upward slope on the flat region of the graph indicates that there is an excess of charge injected into the device resulting in a non-uniform electric field across the sample. This can be adjusted by using a variety of neutral density (ND) filters to reduce the intensity of the laser. This is a very robust method of identifying space charge effects in non-dispersive photocurrents, however it does not provide any quantitative value to determine the intensity of such an effect.

Another approach which is adopted throughout the course of this thesis is the numerical integration method. Integrating the current with respect to time photocurrent transients directly provides us with the total charge generated in the system. The results can then be compared to the charge stored capacitatively in the sample calculated via $Q = CV$ at each electric field. If the photocurrent charge is significantly less than the capacitive charge then we can say the transients are free of any space charge effects. If the

photogenerated charge is higher, then just as the previous method, ND filters are used to reduce the laser intensity. The process is repeated until the value of the photogenerated charge is lower than the capacitive charge. Typical charge values range from 10^{-11} to 10^{-10} C, depending on the applied electric field with a corresponding capacitive stored charge of 10^{-10}-10^{-9}C.

8.6 Investigation into Electron and Hole Charge Traps

The presence of charge traps caused through material impurities or defects in both materials can potentially cause major irregularities to mobility measurements. Thus it is important to investigate and minimize this effect. A technique known as immobile space charge neutralization is used to neutralize the effects of any trapping. This consists of repeated illumination of the sample with earthed electrodes. The first single photocurrent obtained after charge neutralization is then compared to an average of 256 pulses. For holes no measurable change in the photocurrent was observed. For electrons, however, a small decrease in photocurrent was observed suggesting the presence of some charge traps.

In order to measure any deep traps present, the electron mobility of NPB and TPD at room temperature for fields of 100 to 160kV/cm are evaluated using both average and single pulse photocurrents. The high fields are chosen to provide the best signal to noise ratios of our pulses. Significant trapping would alter the internal electric field within the sample resulting in major differences between single pulse obtained mobilities and averaged pulse obtained mobilities. Effectively deep trapping can be regarded as a form

of space charge. Results obtained are within 5% agreement for electron mobility using single pulse and average pulses, which demonstrate the effect of this type of space charge is negligible and that the majority of the electrons traverse the whole sample without significant deep trapping.

8.7 Analysis of Results

The ambipolar nature of NPB and TPD can be investigated via a thorough analysis of mobility values obtained for holes and electrons under a variety of different conditions such as varying electric field and temperature. This section provides a summary of all the mobility results obtained and aims to define the ambipolar nature of these two materials via the Gaussian Disorder Model (GDM).

8.7.1 Extrapolation of GDM Parameters

Figure 33a presents the measured hole mobility in a 600nm NPB sample versus the square root of the electric field ($E^{1/2}$) for a range of temperatures. Figure 33b shows the corresponding electron mobility values obtained from the same sample. For each temperature clear Poole-Frenkel type behaviour can be observed for both types of carriers, that is each data set lies approximately along a straight line. Similar results are seen in hole and electron behaviour in TPD as shown in figures 33c and 33d.

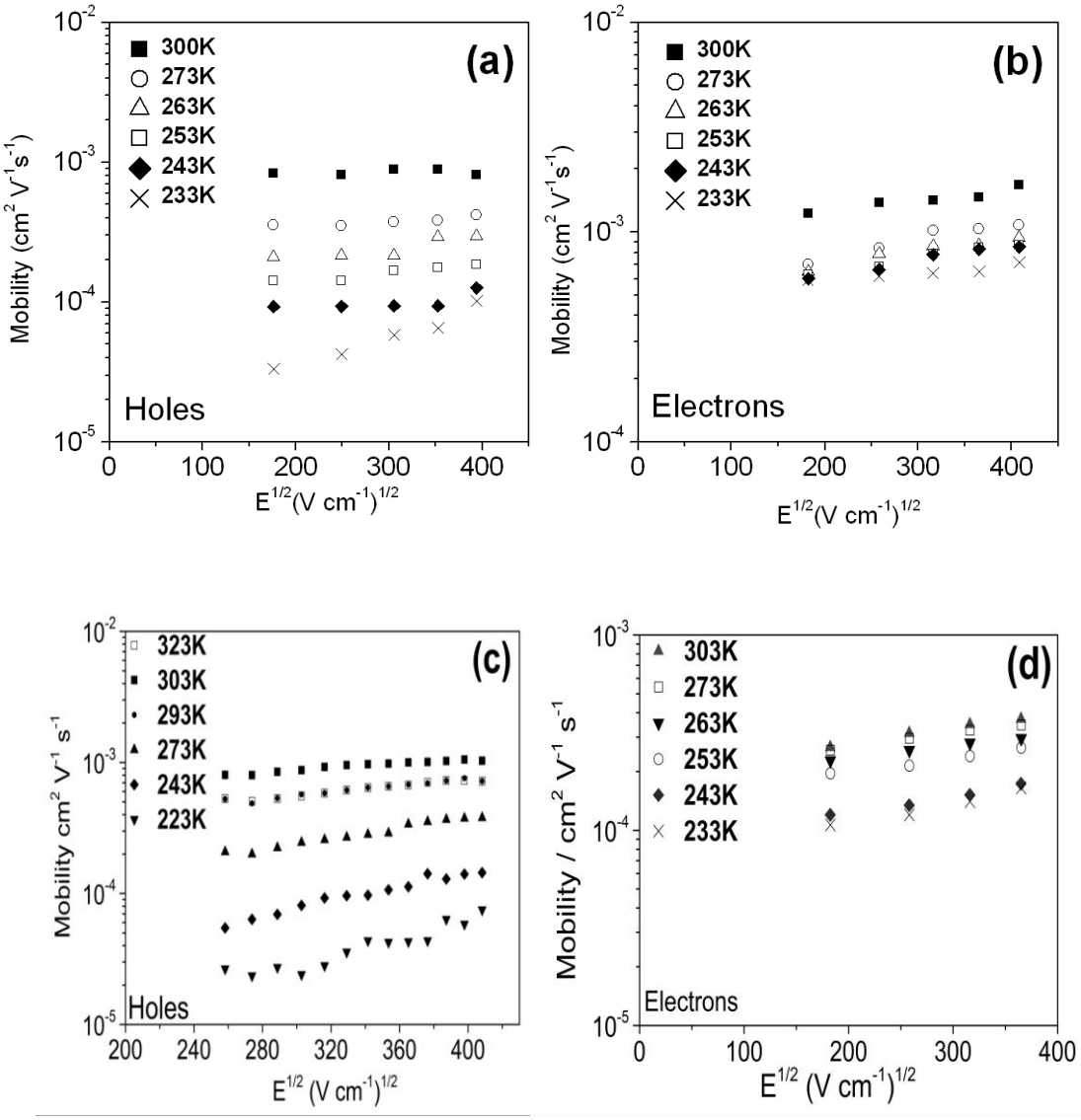

Figure 33. Poole-Frenkel plots of the measured hole (a) and electron (b) mobility obtained in NPB. Hole and electron mobilities in TPD are shown in figures (c) and (d) respectively.

Extrapolation of energetic disorder (σ) and zero field mobility (μ_0) can be obtained from a plot of $\ln \mu(E=0)$ as a function of T^{-2} as shown in figure 34 where the derivative of the fit corresponds to the energetic disorder (σ) and the y-axis intercept to μ_0.

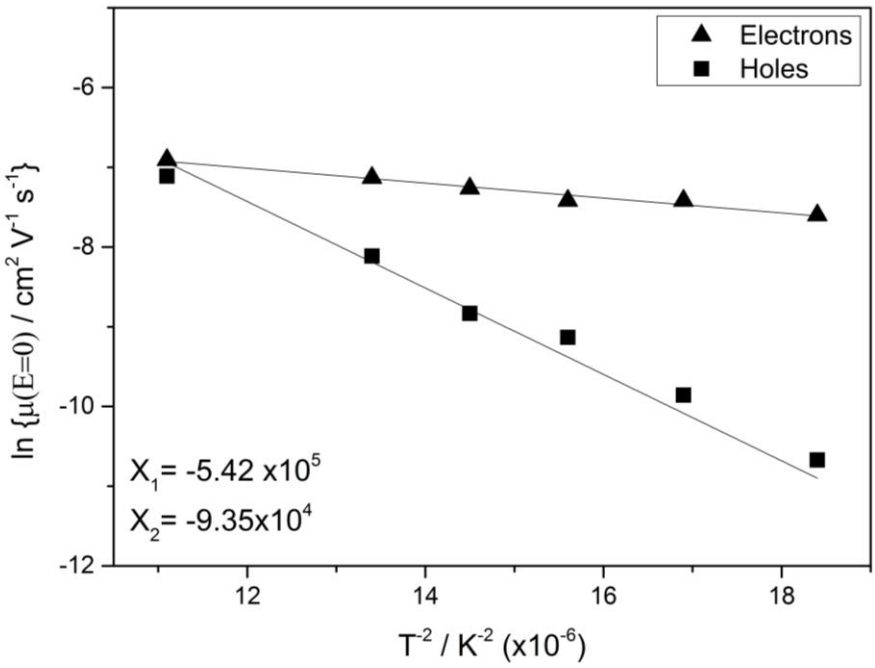

Figure 34. Extrapolation of energetic disorder for holes and electrons in NPB via logarithm of zero field mobility, $\ln \mu(E=0)$ vs T^{-2} plots. X_1 and X_2 represent the gradients of the plots for holes and electrons respectively.

Hence from figure 34 we have:

$$\left(\frac{2\sigma}{3k_B}\right)^2 = 5.42 \times 10^5 \qquad \text{Holes} \qquad \textbf{(23)}$$

$$\left(\frac{2\sigma}{3k_B}\right)^2 = 9.35 \times 10^4 \qquad \text{Electrons} \qquad \textbf{(24)}$$

Thus:

$$\sigma_{Holes} = 95\ meV$$

$$\sigma_{Electrons} = 39\ meV$$

A similar analysis is carried out for TPD as shown in figure 35.

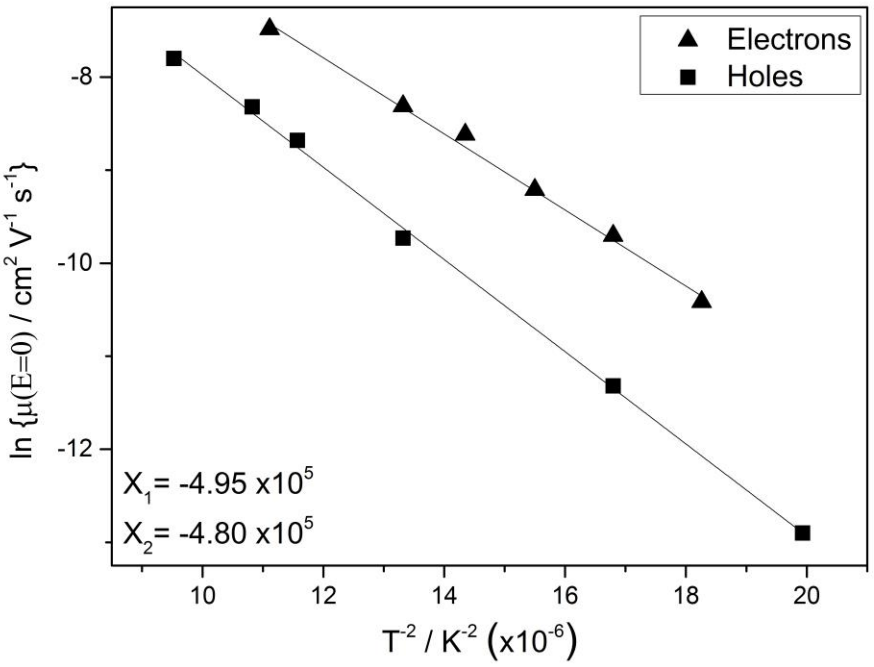

Figure 35. Extrapolation of energetic disorder for holes and electrons in TPD via logarithm of zero field mobility $\ln\ \mu(E=0)$ vs T^{-2} plots. X_1 and X_2 represent the gradients of the plots for holes and electrons respectively.

$$\left(\frac{2\sigma}{3k_B}\right)^2 = 4.95 \times 10^5 \qquad \text{Holes} \qquad \textbf{(25)}$$

$$\left(\frac{2\sigma}{3k_B}\right)^2 = 4.80 \times 10^5 \qquad \text{Electrons} \qquad \textbf{(26)}$$

Hence:

$$\sigma_{Holes} = 90\ meV$$

$$\sigma_{Electrons} = 89\ meV$$

The value of μ_0 is calculated from the y-intercepts in figures 34 and 35. Hence for electrons and holes in NPB it is calculated to be $2.2\text{x}10^{-3}$ cm^2/Vs and $3.2\text{x}10^{-1} cm^2/Vs$ respectively. And for TPD μ_0 = $5.5\text{x}10^{-3}$ cm^2/Vs for electrons and $1.8\text{x}10^{-1}$ cm^2/Vs for holes.

Values for the spatial disorder (Σ) and empirical constant (C_0) are obtained via a plot of $\frac{\partial \ln(\mu)}{\partial(\sqrt{E})}$ versus $\left(\frac{\sigma}{k_B T}\right)^2$ that is from the slopes of the mobility data shown in figure 36. For holes in NPB, Σ = 12.2 and C_0 = 4.9 x 10^{-4} $(cm/sV)^{1/2}$. For holes in TPD, Σ and C_0 are evaluated as 2.6 and 6.0x10^{-2} $cm/V^{1/2}$ respectively (figure 37). Extrapolation of Σ and C_0 for electrons in both materials are not computed due unacceptable high scatter in the $\frac{\partial \ln(\mu)}{\partial(\sqrt{E})}$ versus $\left(\frac{\sigma}{k_B T}\right)^2$ plot as shown in figures 38 and 39. This comes as no surprise given the very small variation in slope with temperature.

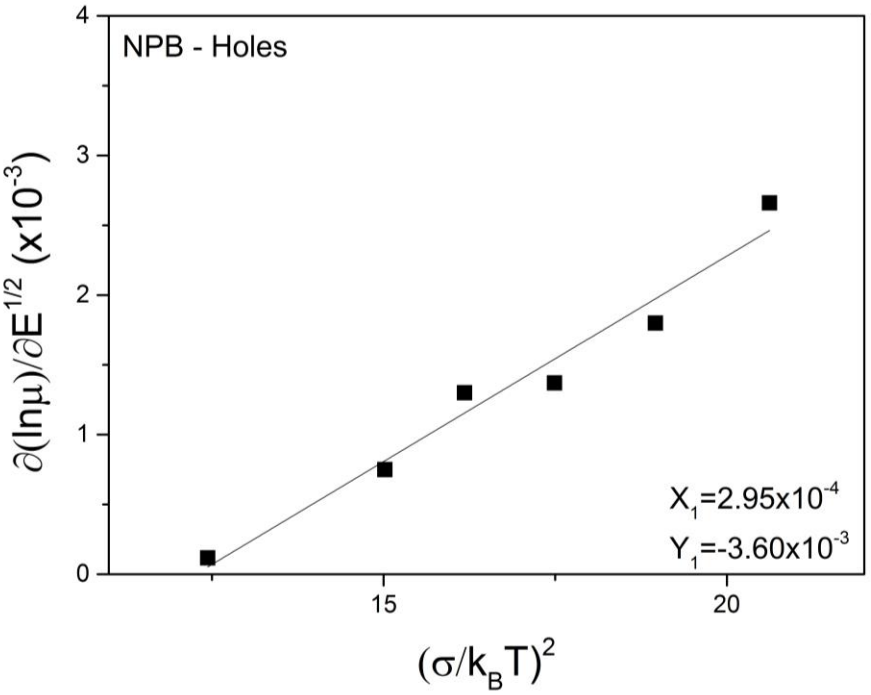

Figure 36. Extrapolation of Σ and C_0 for holes in NPB via plots of $\frac{\partial \ln(\mu)}{\partial(\sqrt{E})}$ versus $\left(\frac{\sigma}{k_B T}\right)^2$. X_1 and Y_1 represent the gradients and the y-intercept respectively.

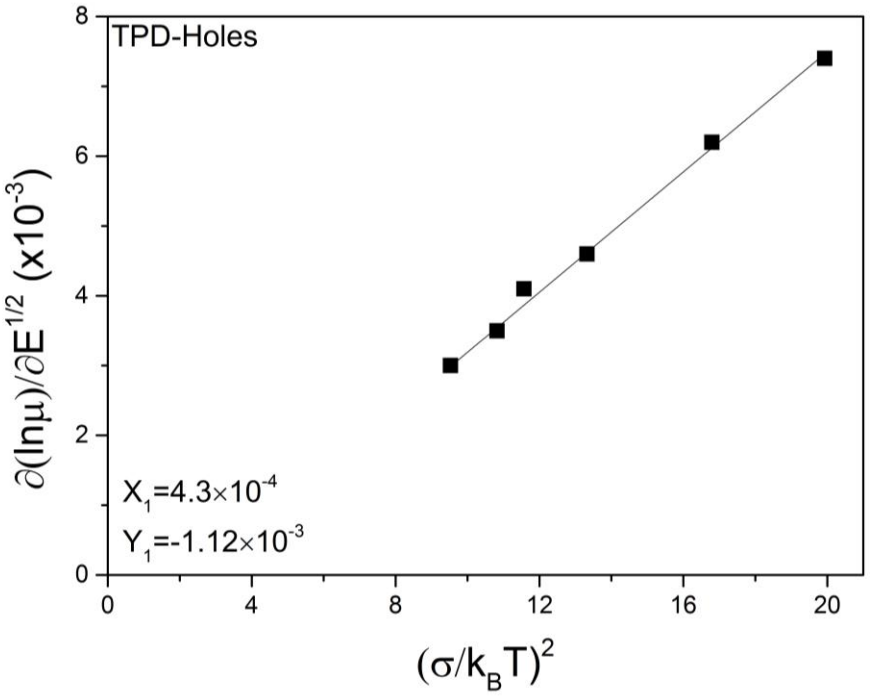

Figure 37. Extrapolation of Σ and C_0 for holes in TPD via plots of $\frac{\partial \ln(\mu)}{\partial(\sqrt{E})}$ versus $\left(\frac{\sigma}{k_B T}\right)^2$. X_1 and Y_1 represent the gradients and the Y intercept respectively.

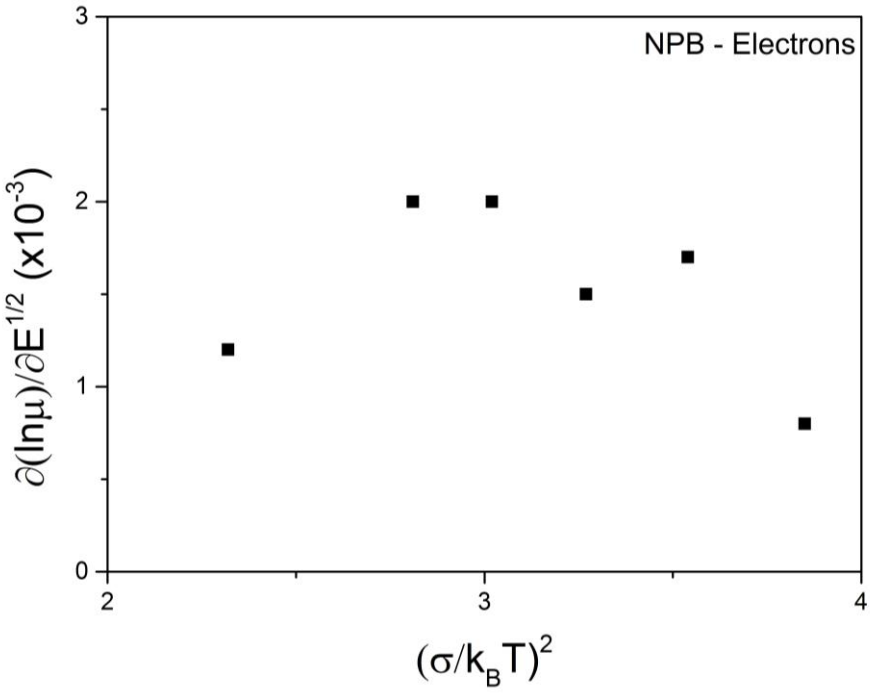

Figure 38. Plots of $\frac{\partial \ln(\mu)}{\partial(\sqrt{E})}$ versus $\left(\frac{\sigma}{k_B T}\right)^2$ for electrons in NPB illustrating the high scatter data.

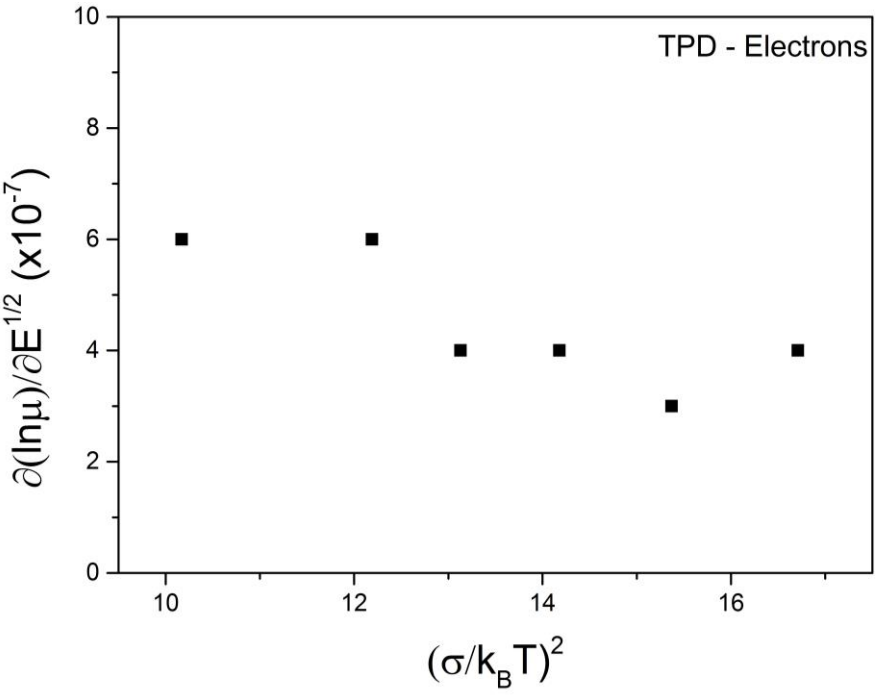

Figure 39. Plots of $\frac{\partial \ln(\mu)}{\partial(\sqrt{E})}$ versus $\left(\frac{\sigma}{k_B T}\right)^2$ for electrons in TPD illustrating the high scatter data.

Table 1. Summary of GDM parameters for holes and electrons in TPD and NPB

	Energetic Disorder (meV)	Spatial Disorder	Zero field Mobility ($cm^2\ V^{-1}s^{-1}$)	C_0 $(cm/sV)^{1/2}$
Holes	$\sigma_{NPB} = 95$ $\sigma_{TPD} = 90$	$\Sigma_{NPB} = 12.2$ $\Sigma_{TPD} = 2.6$	$\mu_{NPB} = 3.2\times10^{-1}$ $\mu_{TPD} = 1.8\times10^{-1}$	NPB = 4.9 TPD = 10.7
Electrons	$\sigma_{NPB} = 39$ $\sigma_{TPD} = 89$	N/A	$\mu_{NPB} = 2.2\times10^{-3}$ $\mu_{TPD} = 5.5\times10^{-3}$	N/A

8.8 Analysis and Discussion of Results

8.8.1 Dispersive Photocurrents and Energetic Disorder

The mobility values for TPD and NPB can be understood by examining the interplay between the dispersive nature of the photocurrents and the energetic disorders calculated. All values for energetic disorder in NPB and TPD are in good agreement with those reported in the literature for typical organic materials, typically ranging from 30meV to 150meV[69]. The lower electron energetic disorder in NPB, compared to holes indicates a narrower width of the DOS of the LUMO. This suggests that the sites that are available to electrons are more densely packed than the ones that are available to holes. At low temperatures there is a large difference between the mobility of holes and electrons in NPB. For example from figure 33 at 233K the mobility of electrons is approximately an order of magnitude higher compared to holes, from 2.8×10^{-5} cm^2/Vs for holes and 5.1×10^{-4} cm^2/Vs for electrons. At high temperatures however the difference between electron and hole mobilities become less noticeable. This effect can clearly be seen from figure 34 where the gap between the mobility value for electrons and holes become narrower with increasing temperature. For example at high temperatures the mobilities are almost equal. This indicates that at low temperatures the energetic disorder has a more dominant effect on mobility and explains why at such temperatures we observe higher electron mobilities compared to holes. With each temperature increase the effect of energetic disorder becomes less significant as the energetic barriers experienced by the carriers becomes narrower.

We also see a very dispersive behaviour of electrons in NPB compared to TPD as characterized by the pre-transit slopes of the photocurrent in figure 40.

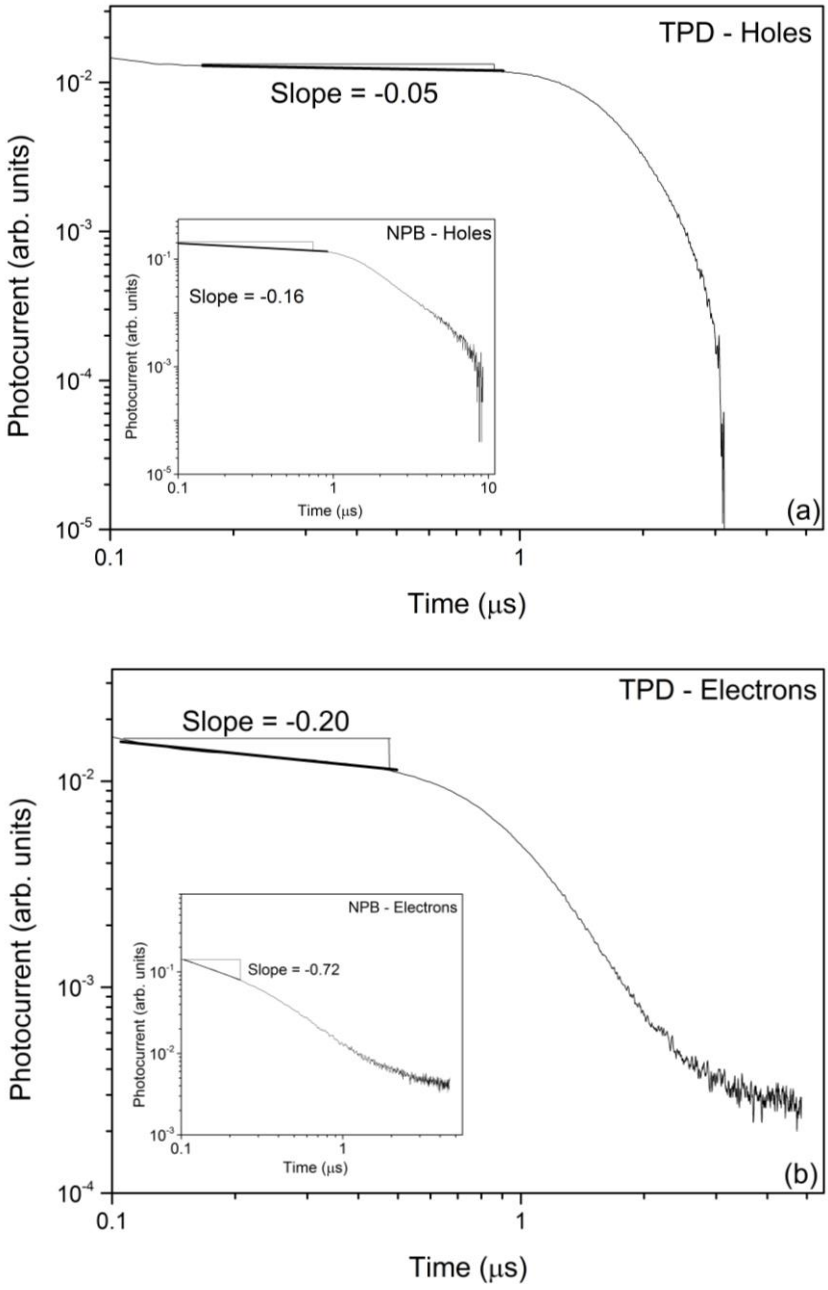

Figure 40. Double logarithmic plots of hole (a) and electron (b) photocurrents in TPD and NPB at room temperature for a constant field of 8.3kV/s. By calculating the pre-transient slopes of each graph we can compare the level of dispersion of the carriers in the respective materials.

Both materials possess similar mobility behaviour with varying temperature. For holes the effect of increasing the temperature has two consequences.

The first is that there is an increase in the absolute value of the mobilities, as would be expected from an increase in the drift velocities of the carriers.

The second observation is that there is a decrease in field dependence mobility for each temperature rise. A similar trend is observed for electrons except that there is seemingly no decrease in field dependence with temperature. This suggests that the electron transport environment is different to that experienced by holes. The difference in transport environment is consistent with the increased dispersion in electron photocurrents compared to holes. For dispersive transport, as in the case of electrons, the average drift velocity decreases with time, a typical feature of a dispersive photocurrent. However, for non-dispersive behaviour a clear flat plateau is observed indicating that the carriers posses a constant drift velocity as a function of time over the region of interest. The fact that the two carriers have very different transport behaviour within the same device comes as a surprise and provides further indication that the transport environment within the LUMO and HOMO of the material must be very different. It was expected that due to the dispersive nature of the electrons, the overall electron mobility would be significantly lower than holes but in fact we see that the electron mobility to be slightly higher. This observation was also surprising but is again consistent with the lower energetic disorder that we get for electrons.

With regards to μ_0 there is a significant difference in the values for electron and holes in both NPB and TPD (see table 1). Such a difference is due to the fact that they are derived by extrapolation of the $\mu(E = 0)$ versus T^{-2} plots to infinite temperature. Thus a small error in the slope can give a large change in μ_0.

8.8.2 Electron-Hole Rearrangement

For the GDM analysis to be valid we need to ensure that there are no electron-hole recombination and/or electron-hole rearrangement within the bulk and that the mobilities measured are solely due to electrons or holes traversing the sample. These two phenomena can be investigated by observing the shape of the photocurrents in both materials. Electron-hole rearrangement can occur if the materials were doped due to impurities throughout the bulk. In this case a hole rearrangement when measuring electron mobility one would expect an electron photocurrent signal to decrease linearly with time where the arrival time would be indicated by the intercept to zero current. One would not obtain a sharp inflection point arrival time as shown by the electron photocurrents. Furthermore if the holes were simply rearranging themselves, the measured mobility would be that of holes and we would not obtain the different temperature dependence of electron and hole mobility as shown in figure 33.

A similar argument can be applied to electron rearrangement when measuring hole mobility except that in this case we can also see a flat plateau

for the hole photocurrents before a sharp drop in the inflection point arrival time.

8.8.3 Electron-Hole Recombination

In the case of electron-hole recombination within the sample (either near the illuminated electrode or within the bulk) this would result in a net negative charge (from the dopant carriers) after a single laser pulse. This would also be the case if electrons or holes where trapped before reaching the counter electrode. This can be observed in systems where there is significant carrier trapping resulting in the reduction of the photocurrent obtained with subsequent laser pulses due to increased space charge effects. We have carefully looked and eliminated this effect in section 3.0. Furthermore the arrival times for both electrons and holes increases with increasing sample thickness. If the carriers where recombined in the bulk, the distance to the counter electrode should not alter the shape of the photocurrent decay. Thus given these points we can discount bulk hole and electron doping and safely attribute the photocurrents to single charge carriers traversing the sample.

9.0 Role of Excited States and Trap Filling on Charge Transport in TPD

9.1 Introduction

The previous chapter presented a comprehensive charge transport analysis of two of the most widely used organic materials in the literature. We showed that under normal operational electric fields, electrons and holes can be injected into the fabricated device and that both materials can transport charge particles with similar mobilities. We also discussed that for a typical conventional hole transport OLED device such as TPD, electroluminescence can be detected, which is testament to the fact that excitons must be present within these traditionally “hole transport” layers. Thus the next logical step is to investigate the effects of such excitons on the charge transport properties of the dominant carriers. This chapter predominately aims to examine the effects of the concentration of excited states on the overall mobility behaviour of the carriers under investigation. Unlike the previous chapter, when excited states could have been generated as a result of an applied bias, as in the case of dark injection or using a laser, as in the TOF technique, in this chapter we will focus on generating and manipulating the concentration of excited states prior to any mobility measurement. Results obtained are analysed via the GDM model and compared to the results in the previous chapter were no ‘artificially’ generated excited states were present.

9.2 Generation of Excited States via Offset Bias

We proceed by fabricating a 600nm TPD device (ITO(20nm)/TPD(600nm)/Al(50nm)) via the vacuum sublimation process discussed in chapter 2. The device is then set up in a dark injection experimental arrangement and a constant offset bias (V_{off}) along with a voltage step (V_0) is applied. Applying an offset voltage prior to a voltage step generates the excited states required for our experiment. Altering V_{off} will then provide a mechanism to change the concentration of excited states in the sample. This effect can be clearly observed by comparing the dark injection transient graphs, using measured bias, V_0, with non-zero offset. Figure 41 shows a series of dark injection transients with varying V_{off} on a 600nm TPD sample. At V_0=10V we can clearly see that by increasing V_{off} we also increase the transit time of the carriers, in some cases by more than 40%. This corresponds to a reduction of the mobility of the carriers.

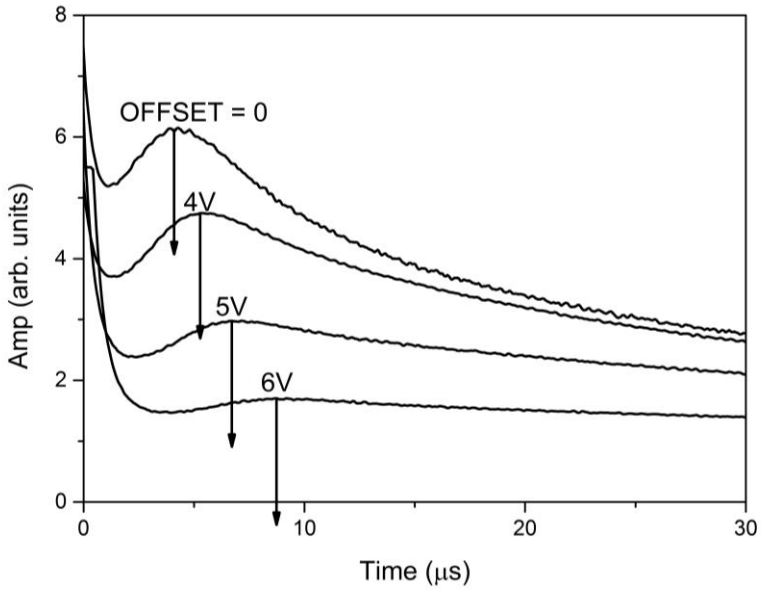

Figure 41. Dark Injection transients for various offset biases for a 600nm TPD sample. V_0 is 10V in all cases.

This effect can be attributed to the creation of excited states in the sample acting as shallow traps to incoming carriers. Although some of the offset bias might be used to fill indigenous charge traps that are already present in sample due to material impurities, the fact that we see a continuous decrease in mobility can be associated to the generation of excited sates. This effect has been studied theoretically in the literature by Agranovich *et al*[93]. They showed that in organic molecular crystals, a triplet exciton and a free charge carrier can form a stable two-particle bound state and depending on the binding energy of the system, the exciton can act as shallow traps to incoming carriers with trap energies of the order of 10-100meV.

Although statistically a combination of singlets and triplets are generated as a result of V_{off}, we assume that most carriers encounter triplets as they have much longer life times compared to singlets.

9.3 Defining the Value of V_{off}

For experiments where V_{off} is constant and V_0 is varied, a suitable V_{off} value is chosen such as to provide sufficient carrier injection of both polarities. A large V_{off} will ensure that enough triplets are generated resulting in higher probability of triplet interaction with incoming carriers. However, it should also be noted that an arbitrarily large value of V_{off} would also limit our V_0 value. A typical 600nm TPD sample such as the one used for this experiment can withstand electric fields up to approximately 1.7×10^5 V/cm or a 10 -11V bias across the sample. Higher electric fields often result in device breakdown. Thus an optimal V_{off} value must be chosen so that to ensure enough triplet

generation whilst at the same time provide a suitable V_0 window to make our measurements. To define this optimal point a thorough understanding of the IV characteristics of the device is required. Figure 42 shows the IV properties of four diodes on a single substrate under test at room temperature.

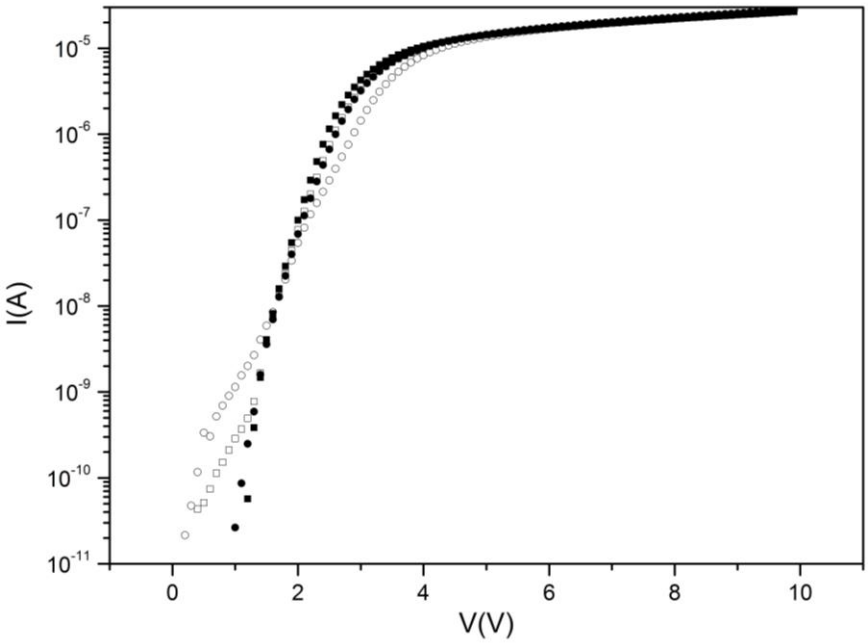

Figure 42. Room temperature IV characteristics of four diodes on a typical 600nm TPD sample.

As shown from figure 42, there is a sharp rise in the current for voltages of up to approximately 3V to around 10μA. Subsequent rises in voltage will only have marginal increases in the current relative to the initial rise. Thus choosing V_{off} as 3V is a reasonable compromise. Its current is of the same order of magnitude as the current at maximum voltage (10V) whilst at the same time it provides a large enough window for our V_0 measurements, i.e. 7V. Hence we can now use V_{off} to conduct mobility measurements in a variety of different settings to investigate the effects of excited states on carrier mobility.

9.4 The Presence of Energetic Traps

Materials presented in this thesis are always subject to some degree of energetic traps which capture and thereby immobilise the injected carriers. The material under test, whether NPB or TPD, will always possess some level of impurity or oxidation that leads to the appearance of traps. Thus it is important to have a general perspective to the number of traps that are present in the system and determine the degree of dependence of the mobility on energetic traps.

Figure 43 shows two dark injection transient currents at room temperature for a 500nm TPD sample for long and short (inset) time scales. The applied electric field is 180kV/cm.

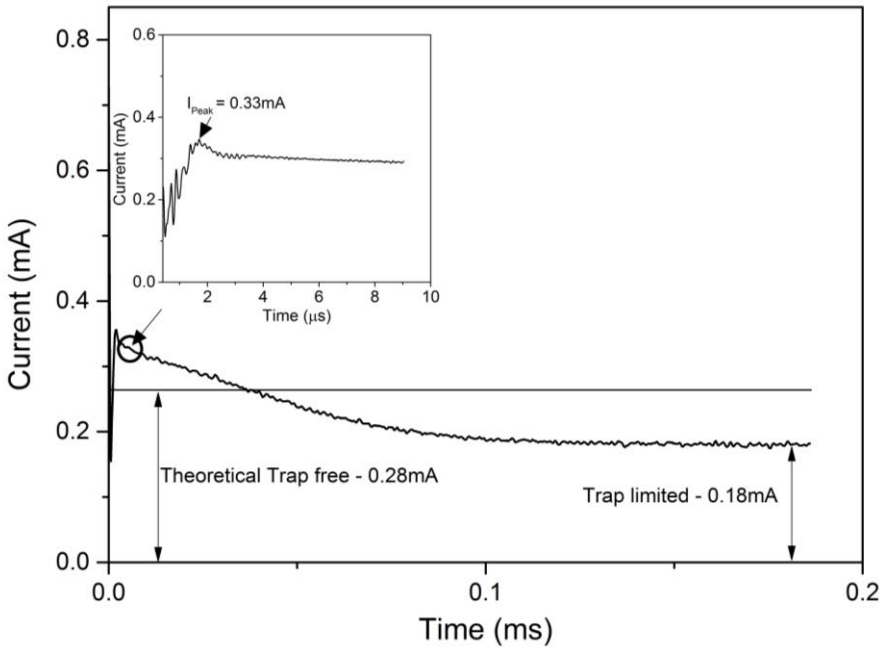

Figure 43. Dark Injection transient of a 500nm TPD sample at a field of180kV/cm for long and short (inset) time intervals.

As shown in section 3.2, in an ideal system with no traps present the DI peak occurs at (1.2 × Trap Free Space Charge Limited (SCL) Current). Hence from figure 43 the theoretical trap free steady state current occurs at 0.28mA (0.33/1.2). The presence of traps will inevitably reduce the current to below this theoretical steady state value. The experimental steady state current will now correspond to the trap limited current, i.e. 0.18mA. Thus by computing the ratio of the trap limited current (I_{TL}) to the trap free current (I_{TF}) we can evaluate the percentage of free carriers encapsulated in the system:

$$\theta = \frac{I_{TL}}{I_{TF}} = \frac{0.18\ mA}{0.28\ mA} = 0.64 \qquad \textbf{(27.1)}$$

Hence:

$$\%\,Traps\ = (1 - 0.64) = 0.36\ = 36\,\% \qquad \textbf{(27.2)}$$

It is important to note that for this value to hold we assume that the current contributing to the DI peak is free from any traps. Experimentally this is impossible to achieve. The fact that we see a peak with a particular width instead a cusp-like shape as discussed in section 3.2 shows that the DI peak will never be free of any traps. However, this provides a reasonable estimate for the fraction of trapped carriers in our system. In fact, in a system with no traps present the peak will occur at a higher current value which shows that our calculation is an underestimate to the actual number of traps present. Thus almost certainly the actual fraction of trapped carriers present is much greater than 36%. Nevertheless this value shows that more than a third of the total carriers in our system are trapped. Thus it is important for any charge transport models to include the effects of such traps. It is also equally important to note that hopping sites are effectively traps by nature. The only

difference between hopping sites and trap sites is their energy. It is assumed that trap energy sites are deeper in nature resulting in the capture of carriers and reducing their drift velocity thus contributing to the diffusion broadening of the transients.

9.5 Effect of Constant Offset on Carrier Mobility for varying V_0

Figure 44 illustrates the mobility ratio of the hole carriers in TPD, that is the ratio of the mobility of carriers with offset to mobility without offset for a 600nm TPD sample, i.e:

$$MobilityRatio = \frac{\mu(OFFSET \neq 0)}{\mu(OFFSET = 0)} \quad \textbf{(28)}$$

The results are shown as a function of V_0 parametric in temperature and the offset bias as discussed earlier is chosen as 3V.

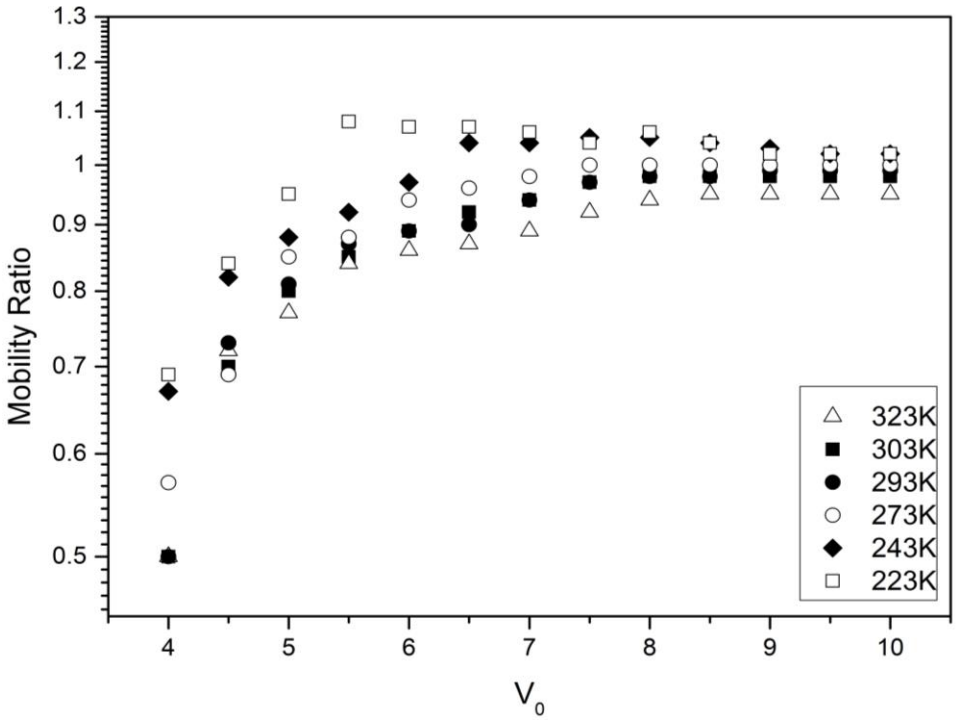

Figure 44. Hole mobility ratio ($\mu_{off}/\mu_{no\text{-}off}$) for a 600nm thick TPD sample for a constant offset of 3V parametric in temperature.

The graph can be categorized into three main features. The first is the relatively large drop in mobility at low V_0 values. The second feature is the convergence of mobility ratio to 1 at high fields irrespective of temperature. And the final observation is the apparent increase of mobility ratio at a given V_0 with decreasing temperature. All these effects can be explained by analysing the total charge distribution in the system, the interplay of charge traps and triplets as a function of temperature and electric field and also by comparing the GDM parameters of Mobility results with and without offset.

9.5.1 Mobility Ratio for Low V_0 Values

It is evident from figure 44 that the presence of excited states has a profound impact on the mobility of the carriers in particular at low electric fields. For example the drop in mobility at 4V is anything between 50 to 69% depending on the temperature. This effect however, becomes less evident with increasing electric field. Such a large drop in mobility can be investigated by analysing the energetic disorder in the system for results with a 3V offset and those of without any offset. The TPD sample that is used for offset measurements is the same as the one in section 8.0. The zero offset mobility results are shown in figure 33c in section 8.7.1 and the results for offset bias are presented in this chapter. Figure 45 shows a summary of the measured mobilities for the 600nm TPD sample under test with a 3V offset bias.

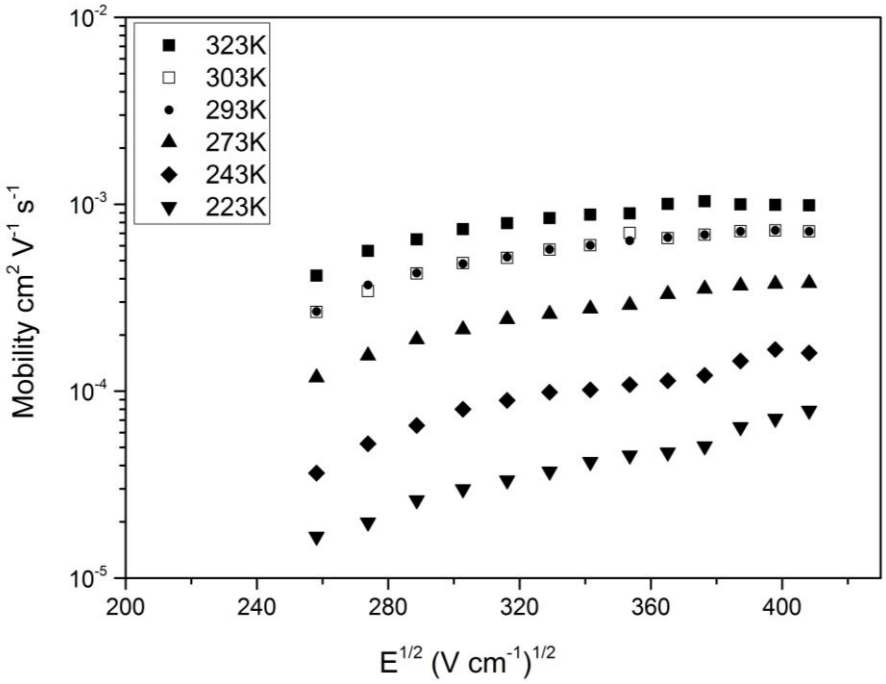

Figure 45. Poole-Frenkel plots of the measured hole mobility in TPD for with offset = 3V

Just as in figure 33, the results exhibit a clear Poole-Frenkel type behaviour, that is for each temperature the mobilities lie approximately on a straight line. Figure 46 illustrates a plot of $\ln \mu(E=0)$ (zero field mobility) versus T^{-2} for each temperature in figure 45. X_1 represents the slope of the graph from which the energetic disorder is calculated.

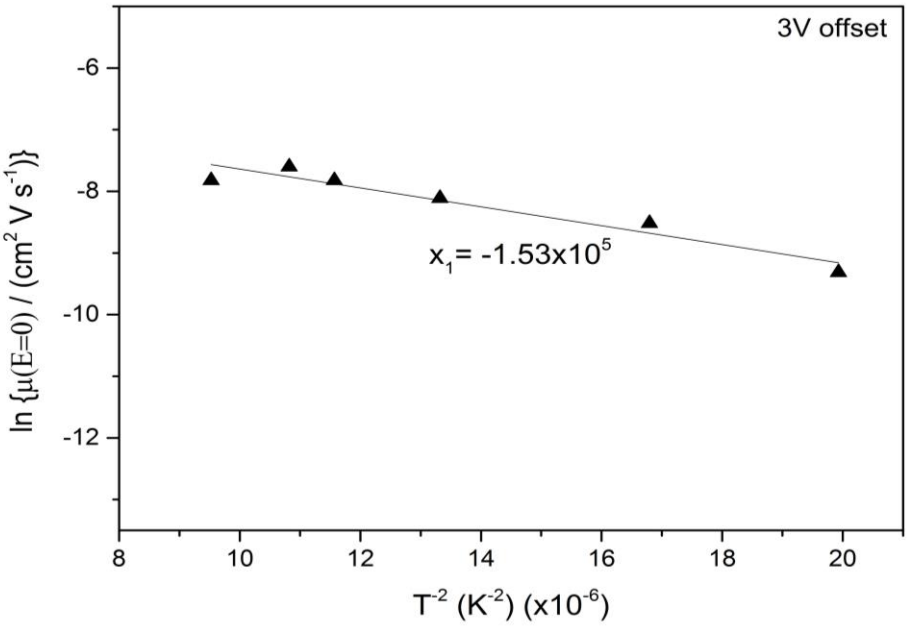

Figure 46. Extrapolation of energetic disorder for holes in TPD via plot of T^{-2} vs mobility. X_1 represents the gradient of the plot for holes with 3V offset bias.

Thus we have:

$$-\left(\frac{2\sigma}{3k_b}\right)^2 = -1.53 \times 10^5 \qquad \textbf{(29)}$$

Hence:

$$\sigma_{off} = 50.6meV$$ With 3V Offset

From the previous chapter we computed a value of 95meV for the energetic disorder with no offset. This corresponds to a drop of approximately 47% when a 3V offset bias is applied. Assuming a Gaussian distribution of energetic sites, this result shows that when an offset bias is applied the standard deviation of the distribution of energetic sites becomes smaller, effectively narrowing the width of the Gaussian as shown in figure 47. This narrowing suggests that some sites are occupied by incoming carriers when a 3V offset is applied, that is that the offset carriers are used to fill some of the energetic traps in the bulk. Thus the effect of applying a prior offset is twofold.

The first is an increase in mobility as a result of trap filling and the other is the reduction of mobility due to triplet/carrier interaction. The swing in mobility in either direction depends on the dominance of each process.

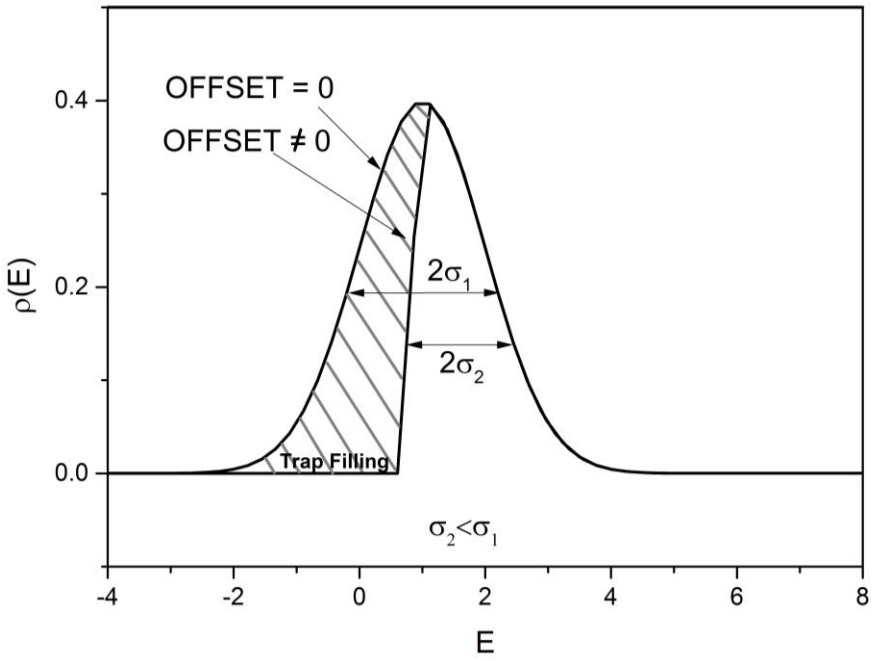

Figure 47. Schematic illustration of the effect of offset on the distribution of energetic sites. A 3V offset results in trap filling (shaded area) narrowing the width of the Gaussian.

To understand the effect of triplets on polarons it is important to examine the different scenarios that might occur when a charge carrier encounters a triplet excited state. A detailed analysis of triplet/polaron interactions is given by Song *et al*[53] whereby they proposed that depending on the spin of the incoming carrier a number of different processes could occur as shown in figure 48.

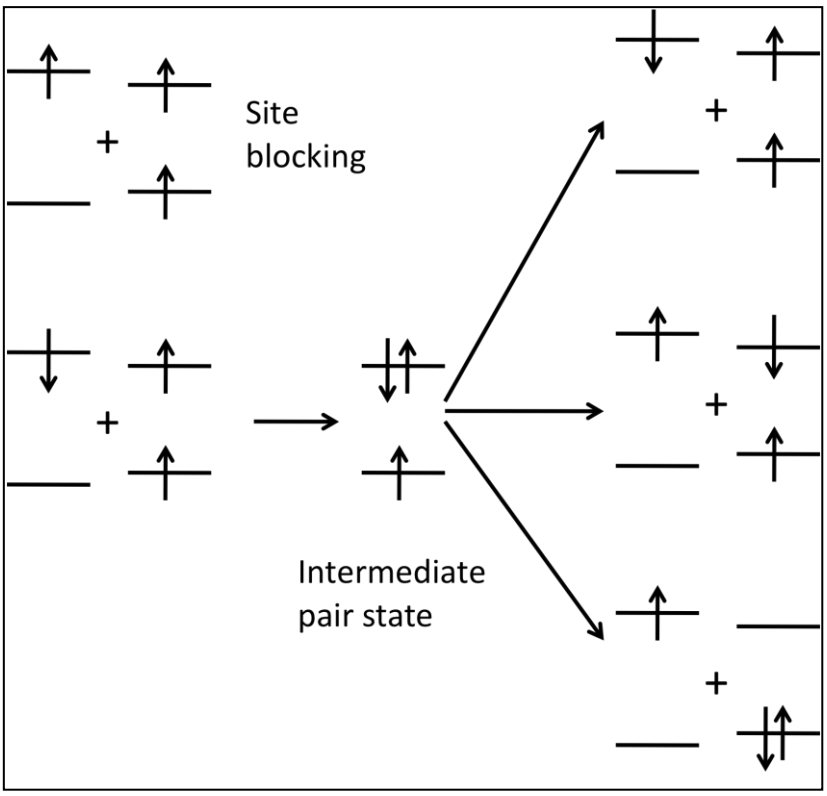

Figure 48. Triplet polaron model. Illustration of the different pathways a carrier can take when encountering a triplet excited state.

The first scenario is the site blocking effect. If the carrier has the same spin as the carriers forming triplet state, then the carrier will either get trapped through the formation of charge Frenkel exciton as proposed by Agranovich[93] or it must find alternative routes to traverse the sample.

The second scenario is when the polaron has the opposite spin to the carrier forming the triplet state. In this case a number of possibilities can occur. The polaron can either depart the molecule leaving behind a triplet or there can be an exchange in spin angular momentum of the carrier and the triplet, leaving behind a singlet and a polaron with a spin state opposite to when it started.

It is important to note that in both circumstances either site blocking or interaction between polaron and triplet, the result would be a reduction in mobility. It is evident from figure 44 that the dominant process at low electric fields is the triplet/carrier interaction as a significant drop in mobility is observed. This effect however is reduced rapidly with increasing voltage.

The increase of electric field will result in an increase in the total charge within the sample during measurement and subsequently raising the probability of triplet/carrier interaction (see section 9.5.3 for further analysis). However, although this effect should ordinarily result in the decrease in mobility, we see quite the opposite. There is a systematic rise in the mobility ratio with each voltage step. This effect is discussed in more details in the next section by analysing the drift velocity of carriers as a function of temperature and electric field.

9.5.2 Convergence of the Mobility Ratio to Unity

Considering figure 44, after the initial mobility drop at 4V there is a rapid rise in the mobility ratio at 4.5V for all temperatures. For example at 323K we see a rise of more than 20%. A similar trend can be observed for the other temperature measurements. We can also observe that the rate of increase of mobility ratio decreases with increasing V_0 irrespective of temperature such that at high electric fields (from approximately 8V-10V) the ratio tends to converge to approximately 1. This suggests that the absolute mobility of carriers is almost identical in both cases and that applying an offset bias will have almost no effect on the incoming carriers. This comes as no surprise as there is a significant increase in the average drift velocity (v_d) of carriers with increasing electric field as shown in figure 49. In hopping transport, increasing v_d with increasing electric field is explained by more sites becoming energetically available and any energetic barriers are lowered by an applied field. This implies enhanced de-trapping. If we apply an offset, the enhanced de-trapping due to an increase in electric field can overcome any triplet trapping effects. Thus any carrier slowing as a result of site blocking or singlet generation will quickly be overcome by a rise in the average drift velocity of the carriers with increasing electric field. Eventually the electric field will be so high that the presence of triplets would be insignificant and most carriers can de-trap and traverse the sample without significant obstruction. It should be noted that the convergence of mobility ratio is not exactly 1. If we were to evaluate the average mobility ratio for all the temperature data at V_0 = 10V we will get a value of 0.99. Given an overall error of 3% this value is in

line with a mobility ratio of 1. It is however interesting to note the calculated average without any error is slightly lower than 1. This suggests that although the effect of triplet/carrier interaction is significantly lowered, it not eliminated entirely. There would still be some minority carriers that would get immobilised as a result of triplet/carrier interaction.

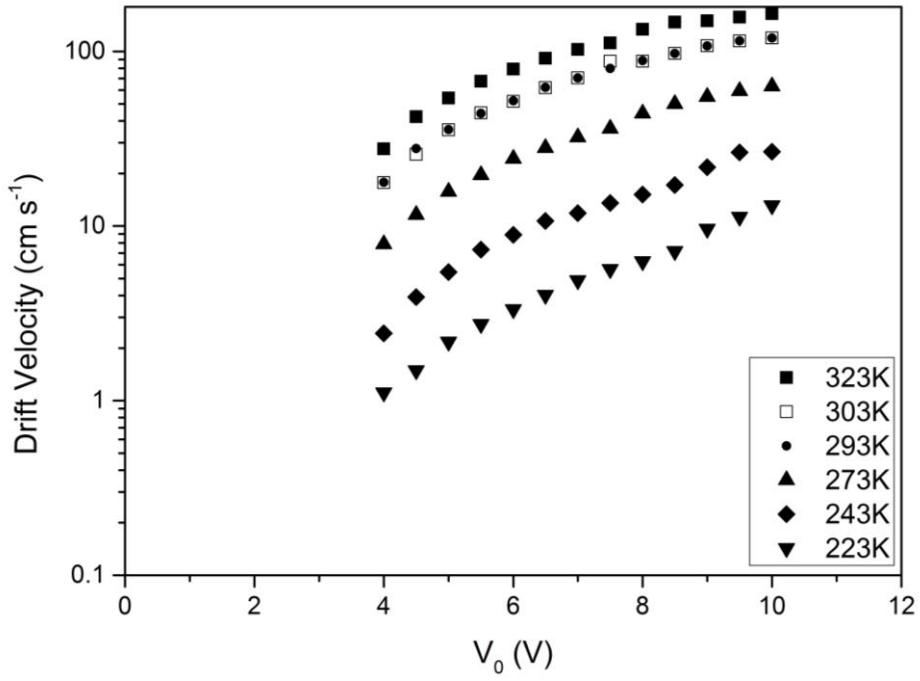

Figure 49. Drift velocity of hole carriers in 600nm TPD sample with 3V offset.

9.5.3 Upward Shift in Mobility Ratio with Respect to Decreasing Temperature

Another feature of the results is the apparent upward shift of mobility ratio with respect to decreasing temperature. Figure 50 demonstrates clearly this upward trend by the mobility ratio measured using a fixed offset (3V) at different bias versus temperature.

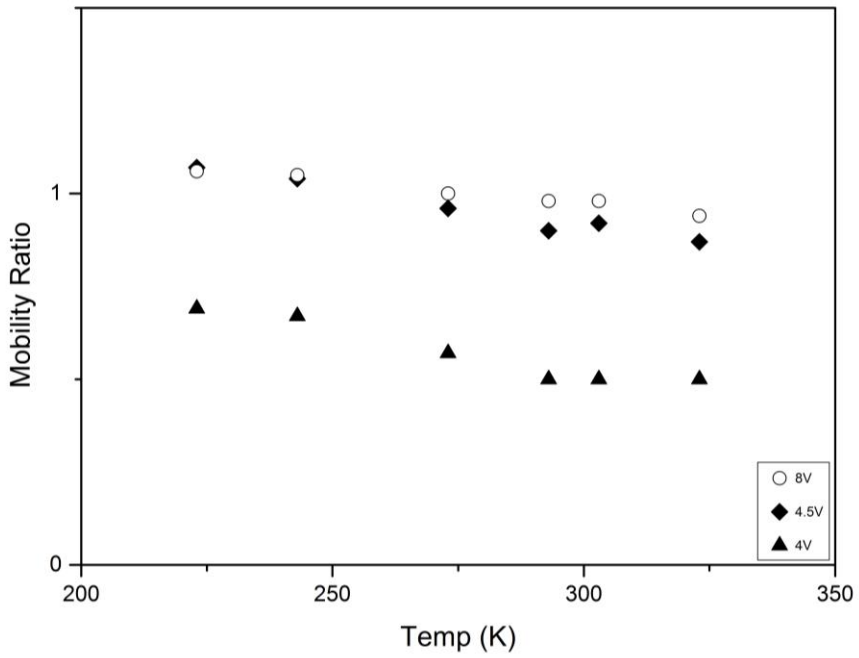

Figure 50. Mobility ratio plot as a function of temperature for various V_0 values, showing the dependence of mobility ratio on temperature.

Figure 50 can be interpreted as a more pronounced trap filling effect as the temperature in lowered, i.e. as traps are filled by the offset bias the resulting mobility ratio increases. This phenomenon can be analysed by computing the total charge density in the device for each temperature. Figure 51a shows the total charge density at each voltage measurement for each temperature value. The total charge is derived by measuring the steady state

current (from DI transients) through the device for each temperature and multiplying the current value by the corresponding transit time of the carriers. This will provide the total charge in the device in terms of coulombs. Hence diving that value by (electronic charge × volume) will give us the total number of carriers in the device per unit volume.

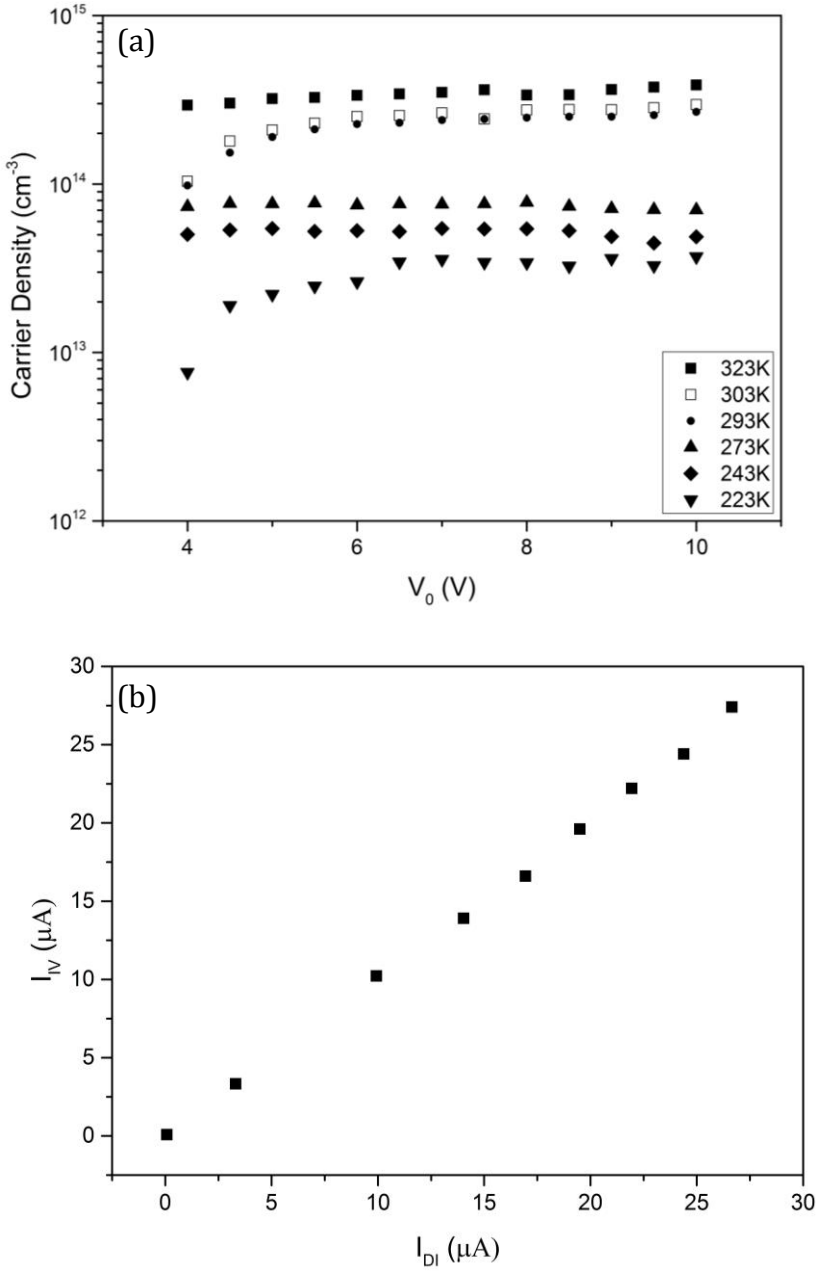

Figure 51. (a), Illustration of total charge density with 3V offset as a function of V_0 and (b), comparison of current recorded from direct IV measurements and DI transients at room temperature.

We assume that the DI steady state transients resemble the true IV nature of the device. To ensure that this is indeed the case we recorded a series of direct IV measurements of our device at room temperature for various biases and compared the results to the corresponding DI steady state currents, as shown in figure 51b. There is almost a perfect linear relationship between the two sets of data indicating that current from DI transients is almost identical to the current measured from direct IV measurements.

We can see from figure 51a that the total charge in the device increases with applied temperature. For example for low temperatures i.e. 223K to 273K the total number of carriers is approximately an order of magnitude smaller (~ 10^{-13} - 10^{-14} /cm^3) compared to higher temperatures at 293K, 303K and 323K. The charge density resulting from any bias decreases with decreasing temperature. For lower temperatures the majority of carriers due to V_{off} (for a given trap density) will fill in charge traps leaving behind fewer carriers to form triplets. Thus there is an upward shift in mobility ratio with decreasing temperature as more traps are filled and fewer triplets are formed. For example, in figure 44 at 233K the mobility ratio exceeds the 100% threshold at 5.5V before tending to 1 for higher fields. This overshoot is clear evidence of trap filling as there is a significant rise in mobility with offset. It is important to note that even at low temperatures such as 233K the mobility ratio also converges to 1 at high electric fields. As discussed earlier an increase in electric field (V_0) would also result in a rise in total charge in the device. Thus an increase in charge carriers would subsequently increase the probability of triplet/polaron interaction resulting in a decrease in mobility with electric field.

9.6 Effect of Varying Offset on Carrier Mobility

In the previous section we discussed the effect of a constant offset on charge carrier mobility. The next logical step is to reverse the experiment and investigate the effects of keeping V_0 constant and varying V_{off}. The sample under test is the same 600nm TPD sample that was used in section 9.5 and the mobility values are evaluated by the same dark injection method discussed in section 3.2. Figure 52 shows the mobility ratio as a function of offset bias ranging from 0.2V to 7V for various temperature measurements. V_0 is always kept at 10V.

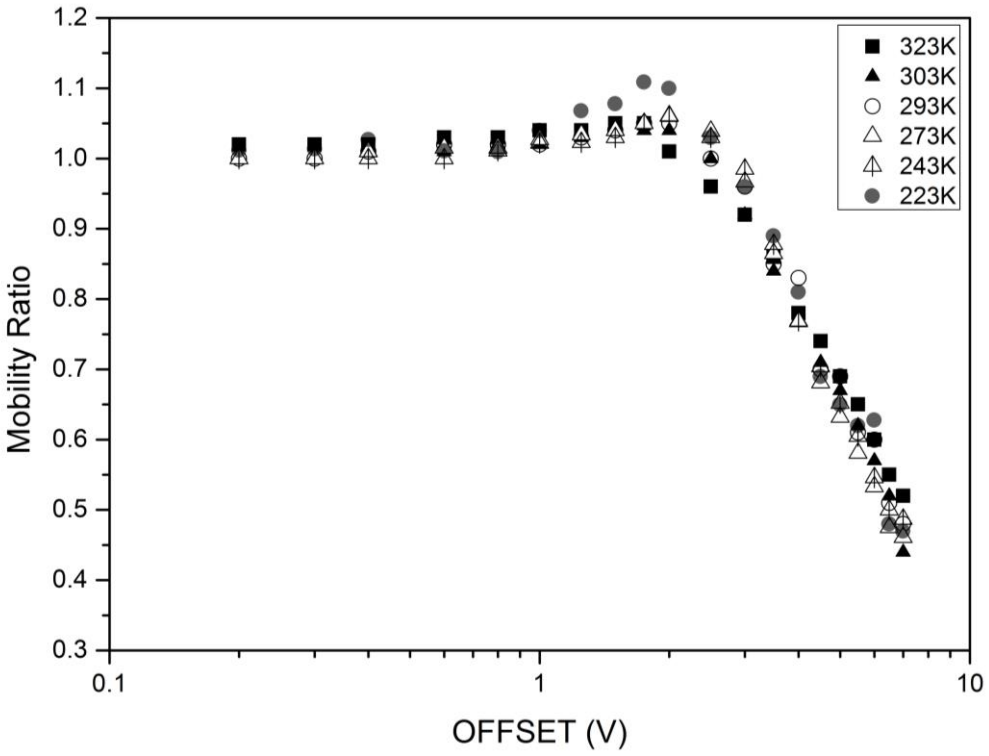

Figure 52. Hole mobility ratio ($\mu_{off}/\mu_{no\text{-}off}$) for a 600nm thick TPD sample for varying offset values parametric in temperature. V_0 is always kept at 10V.

From figure 52 we can see two distinctive features occurring. The first is the gradual increase of mobility with V_{off} until approximately 2V specially at low temperatures. The second feature is the sudden drop in mobility for offset values above 2V. Similar to the analysis on the previous section such an effect can be explained in terms of the interplay of triplet/polaron interaction and trap filling.

9.6.1 Mobility Rise for Offset Values up to 2V

The steady rise of the mobility ratio for offset values of up to 2V can be attributed to the effect of trap filling in the system. With every increase in V_{off} more charge carriers are injected into the device prior to any mobility measurement. These fill an increasing number of energetic traps, resulting in a rise in mobility. Similar to the constant offset case, this effect becomes more apparent with decreasing temperatures. For example in figure 52, at 233K the mobility ratio peaks at 1.12 at 1.8V before starting to fall whereas at 323K, it peaks at 1.03 at 1.8V before converging to 1 at higher fields.

9.6.2 Mobility Fall for Offset Values Above 2V

The other feature of figure 52 is the sudden drop of mobility for offset values above 2V. The contribution of offset to trap filling seems to saturate at 2V and any further increase in V_{off} would only increase the concentration of triplets in the device resulting in a fall in mobility values. It should be noted that ambipolar injection in the device is always present however there will be

an imbalance of carrier injection depending on the magnitude of V_{off}. This imbalance of injection of carriers suggests that at voltages up to approximately 2V the concentration of electrons is too low to generate any measureable triplet effect, hence the trap filling effect becomes dominant. At V_{off} values above 2V, electron injection becomes more apparent and would result in an increased triplet population. Thus triplet-polaron interaction becomes the more dominant factor in defining carrier mobility.

9.7 Conclusions

In this chapter we have shown the effects of applying both varying and constant offset on the mobility of holes in a 600nm TPD sample. We have shown that an offset bias has a clear effect on the mobility of the carriers. Furthermore we have quantitatively attributed such changes in mobility to the interplay between triplet/polaron interaction and trap filling by analysing the data with respect to the GDM model, the concentration of traps and the distribution of charge in the device. We showed that in the case where a constant 3V offset is applied, the energetic disorder for holes in TPD decreases by approximately 47% from 95meV without offset to 53mev with offset. This narrowing of the DOS with an offset bias is consistent with trap filling. At high temperatures triplet/polaron interactions are the dominant feature and at low temperatures trap filling is the dominant mechanism for determining carrier mobility. A schematic of the interplay of these process is shown in figure 53.

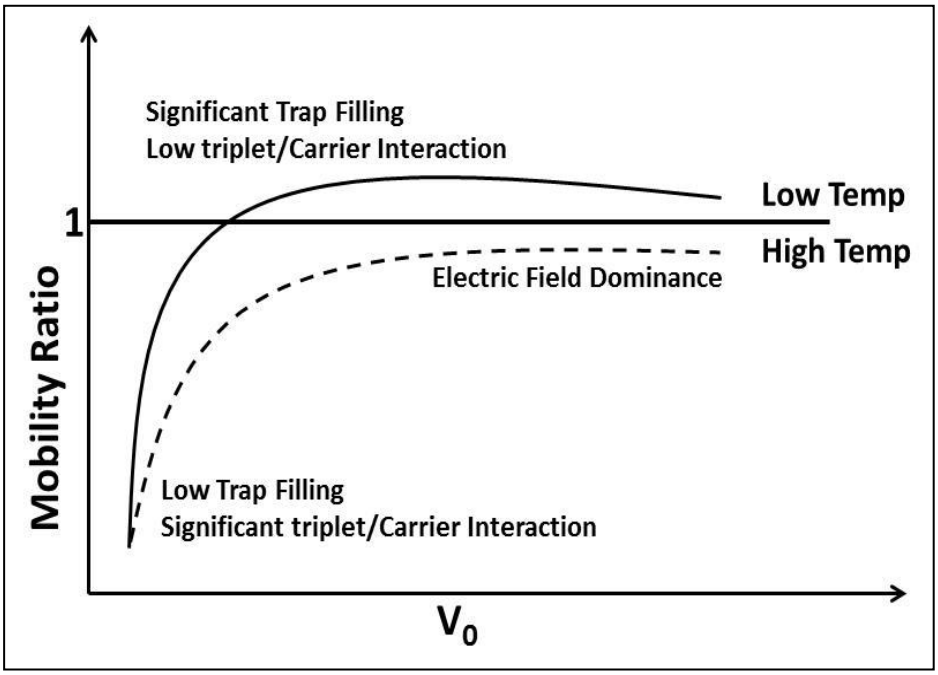

Figure 53. Schematic representation of the different processes determining the mobility ratio in TPD as a function of V_0 for a constant offset.

We also showed the effect of a varying offset on the mobility ratio. As the offset bias is increased we see an enhanced mobility ratio at low bias especially for low temperatures. Such behaviour is consistent with the constant offset results and is further evidence to the fact that at low temperatures trap filling is the dominant mechanism for determining the mobility ratio. Once the offset exceeds the 2V threshold there is a rapid reduction in mobility as a result of ambipolar injection, thus enhancing the triplet/carrier interaction. A schematic of these processes is shown in figure 54.

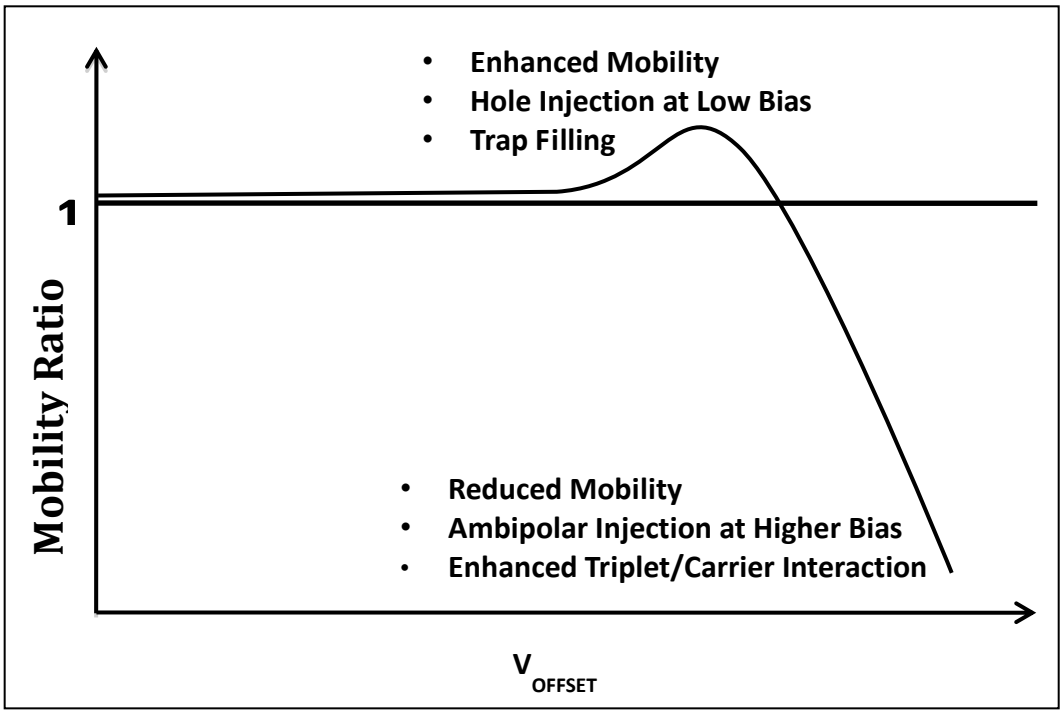

Figure 54. Schematic representation of the different processes determining the mobility ratio in TPD as function of V_{OFFSET} for a constant V_0.

This analysis is also consistent with the triplet/polaron interaction model discussed in section 9.5.1. We can attribute the effect of the reduction of mobility at low electric fields to site blocking. Where the spin of the hole is the same as the spin of the hole in the exciton, the hole cannot hop onto that site and site blocking occurs, thus reducing the mobility. As the electric field is increased the triplet blocking barrier can be overcome resulting in higher mobility ratios.

In the case where the carriers have an opposite spin to those forming the triplets we still expect a reduction in mobility as result of exchange of spin angular momentum at the intermediate state. Just as site blocking, the expected rise in mobility with electric field can be related to the increase in the

average drift velocity of carriers where any loss in energy is compensated by an increase in drift velocity.

10.0 Phosphorescence Effects on Transport Properties of Organics

In pure organic compounds, emission from a triplet state is usually forbidden due to quantum mechanical selection rules. However, when a triplet emitter is incorporated into the structure, emission from the triplet excited state is possible via mixing of the singlet and triplet states as discussed in section 1.4. Triplets generated in a bulk system such as the one under test will have its unpaired electrons occupy the energy levels of both the organic and the metal complex. Thus each electron is subject to a different degree of spin-orbit coupling. As a result the total angular momentum of each electron (S_1 and S_2) precess at a slightly different rate and hence the magnitude of the combined angular momentum vector (S_1+S_2) will fluctuate between 0 and 1, thus the initial triplet will start oscillating between a triplet and singlet state. This mechanism is illustrated schematically in figure 55 and it can happen as a result of a phase change and/or spin flip of one of the electrons involved in the process. In OLED devices this can lead to greater device efficiencies as it allows radiative decay from triplets in the form of phosphorescence. The effect of this phenomenon is discussed further in this section by studying the transport properties of a typical TPD device (ITO/TPD/Al) doped with small amounts of an iridium complex, iridium-tris(1-phenyl-isoquinolinato-C2,N), $Ir(piq)_3$.

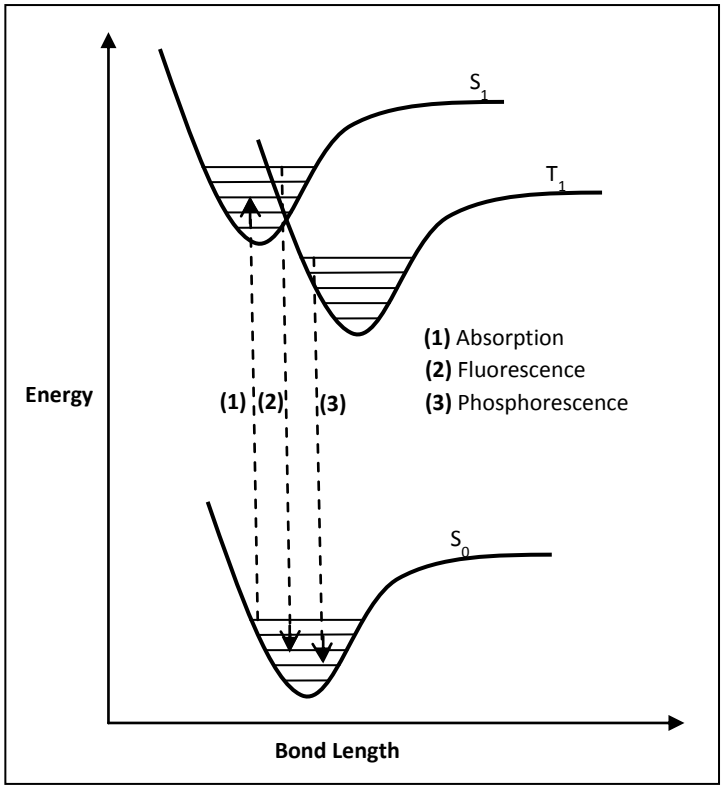

Figure 55. Schematic representation of phosphorescence illustrating singlet/triplet transitions.

Preparation of the device occurred in the manner described in section 4.0 by co-evaporating $Ir(piq)_3$ and TPD with a ratio of 1:100 respectively so that the final device thickness was 0.55μm. It should be noted that when evaporating, careful attention must be given to the thickness calibration of the Iridium complex as only very small amounts are involved and a small drift in the deposition rate measured can potentially have a significant impact on the device composition. The mobility of hole carriers is then measured using DI as a function of offset voltage. The results of this along with those from a nominal 0.5μm TPD without $Ir(piq)_3$ are shown figure 56. The DI mobility measurement pulse (V_0) is 5.5V in both cases.

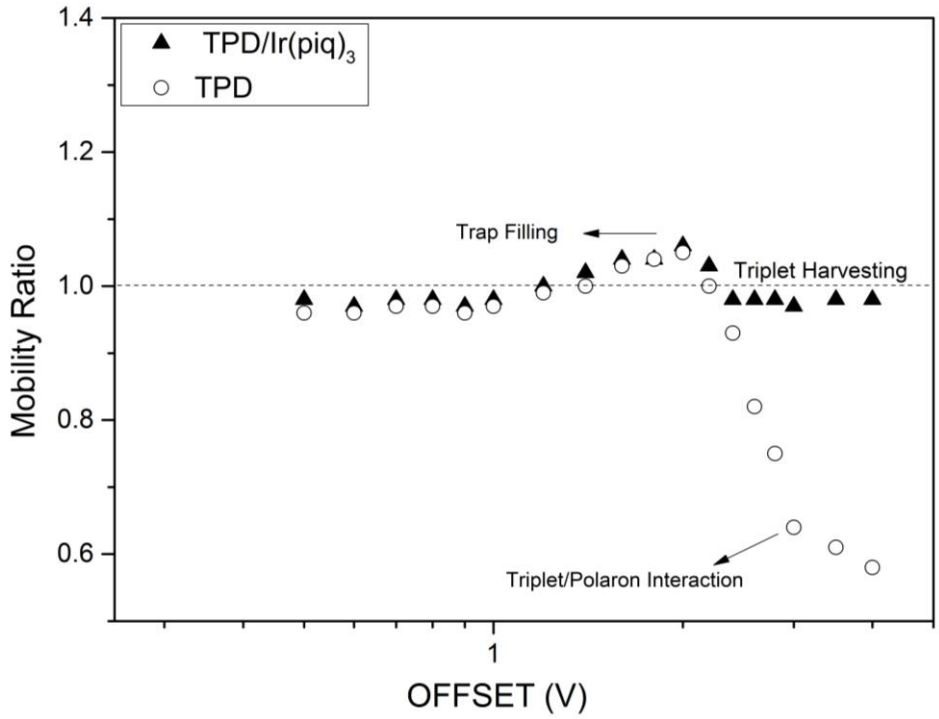

Figure 56. Hole mobility ratio ($\mu_{off}/\mu_{no\text{-}off}$) as a function of offset voltage for a plain TPD and TPD/ $Ir(piq)_3$ sample. V_0 = 5.5V.

Although figure 56 shows mobility ratios, the overall mobility values for $Ir(piq)_3$ without any offset are some 30% lower compared to a TPD sample without any $Ir(piq)_3$. This reduction in mobility is expected as $Ir(piq)_3$ molecules act as charge traps limiting the overall drift velocity of the carriers.

We can see that figure 56 resembles the results shown in figure 52 (section 9.6). The only major difference is the flat response of the $Ir(piq)_3$ device after the initial rise from 1V to approximately 2V. This comes as no surprise as any triplets created, as a direct result of the offset bias will quickly be quenched due to the presence the triplet emitter, resulting in a greatly reduced triplet population. Thus the effect of site blocking becomes almost negligible above 2V. Thus by incorporating a phosphorescence complex into our original TPD structure we can almost 'switch off' the triplet/polaron

interaction effect so that the mobility would mainly be dependent on the distribution of traps and by the degree to which they can be filled. It should be noted however that the mobility ratio with the triplet emitter incorporated is just below the 1. This is due to the fact that triplet-polaron interaction processes are not entirely diminished. Triplets are not quenched in their entirety, there will always be some small probability of triplets present and hence triplet blocking.

This provides further evidence that the presence of excited states can have a profound impact on the mobility of carriers. However, just as discussed in section 9.0, equally important is the effect of trap filling. Careful attention must given to this mechanism as the effect of triplet/polaron interaction only becomes evident after the traps are filled.

11.0 Typical Experimental Errors in Mobility Results

All mobility measurements in this thesis are repeated at least 3 times with different samples. For each sample the mobility for each temperature, V_0 and V_{off} is recorded and a mean for all the results calculated. The mean for each category of results is then compared to the original mobility value and the error computed. For example if the mobility of a particular sample at 233K and 4V with no offset is 4.1×10^{-4} cm^2/Vs, and the average mobility for this particular arrangement is calculated as 4.6×10^{-4} cm^2/Vs, then the error on this particular group of results is approximately 11% $\left(\frac{4.1\times10^{-4} - 4.6\times10^{-4}}{4.6\times10^{-4}}\right)\times100$ or

4.1±0.5 $\times 10^{-4}$ cm^2/Vs. For all the mobility results measured the errors calculated for each category rarely exceeded the 3% threshold. In many cases results from various samples could be superimposed on top each other with the only factor differentiating between them being the background noise.

12.0 Conclusion and Further Work

12.1 Conclusion

In general one can conclude that the concept of charge transport in organic semiconductors has gone through a rapid transition over the last ten years alone. Today, one can see that the efforts of different research groups around the world have become more focused and collective in a specific direction. For example, the study of magnetic field effects on the excitonic processes within an organic device has gained considerable interest in recent years.

The prospect of organic materials particularly within the fields of solar cells and light emitting diodes are very promising indeed. Nevertheless, despite all the breakthroughs, there remain many more questions that need to be answered if organic semiconductor were to compete effectively with their inorganic counterparts.

Throughout the course of this thesis we have presented four studies for which we analyzed in detail the charge transport properties of two of the most widely used organic materials in the literature, NPB and TPD. We showed that electrons can be injected into a “traditionally” hole transport layer OLED under normal operating conditions and that they can be transported just as well as

holes with mobility values in the range of 10^{-4}-10^{-3} cm^2/Vs. This was a significant result as it explains why we get light output from an OLED device that solely consists of a hole transport material. We concluded that there must always be some degree of excitonic behaviour taking place in these conventional hole transporters otherwise we would not observe a light output. The results also showed that in order for us to label a material as hole or electron transporter, we should also take into consideration the intrinsic properties of the material in addition to the respective energy levels of the material and electrodes.

We then went further and discussed the effect of excited states on charge carriers. We showed how one can generate excited states by applying a prior offset bias and how it can be used to test their effect on carrier mobility. Two experiments were conducted. The first involved measuring the mobility ratio of hole carriers in TPD as a function of electric field with a constant offset bias for a range of temperatures. The second was very similar except that the electric field used for transport measurement was kept constant whilst varying the offset bias. In both cases we concluded that the presence of excited states has a major effect on the mobility of carriers and the strength of this effect depends on the temperature and electric field. We showed that at low electric fields and high temperatures site blocking due to triplet excited states is a dominant mechanism for determining carrier mobility whereas at lower temperatures and intermediate electric fields we associated the high mobility ratios to the dominant effect of trap filling. We also concluded that the convergence of the mobility ratios to 1 is due to the high electric field effect such that any carrier trapping due to triplet-carrier

interaction would swiftly de-trap due to the increase of electric field. This was an important milestone as we elucidated the interplay between carrier-exciton interaction and trap filling. We showed that the swing in mobility of either direction depends on the dominance of each effect.

The final part of this thesis focused on the effect of incorporating a phosphorescent complex in the TPD on the overall mobility ratio when an offset bias is applied. We showed that by doping our TPD device with $Ir(piq)_3$, we would completely change the concentration of triplets in the device due to intersystem crossing. We demonstrated how the mobility ratio remained unchanged with offset bias when a TPD device is doped with 1% of $Ir(piq)_3$. This is also an important result as it not only provides evidence for the effect of excited states on carrier mobility but also assists in providing a method to tune the concentration of triplets in a device in a manner that suits us best. We can see that once the effect of triplets is removed due to the presence of a triplet emitter the hole mobilities return to their pre-offset values.

Thus we can conclude that a thorough understanding of ambipolar carrier transport in such materials where they have historically been labeled as hole transport layers is essential, not only for improving the fundamental understanding of charge transport in the materials but also more crucially in device models. This thesis has provided a comprehensive overview and the hope is that future work in this area would incorporate some of the ideas mentioned in the previous chapters.

12.2 Further Work

12.2.1 Analysis of Trap Densities

In section 9.0 we showed how the presence of excited states affects the mobility of carriers. We illustrated how an increase in the number of triplets can be related to a decrease in carrier mobility. This was shown by analyzing and quantifying the total distribution of charge in the device. Although the concentration of triplets increases with applied V_0 above turn on, it would be interesting to directly quantify the of number triplets present in the bulk with each offset bias and temperature. This will provide us with a direct relationship between the number of triplets present and the total charge in the system by measuring the ratio of the two. Thus, we will be able to relate a particular ratio to a specific mobility behaviour and test to see if we get similar effects in other disordered organic materials.

One way of evaluating the instantaneous concentration of triplets with respect to offset bias is to calculate the number of singlets present in the bulk. This can be done by using an integrating sphere and a sensitive detector to measure the light output of the device. The light output could then be directly related to the number of singlets present, which could easily be converted into triplet concentration. For example for a light output of 0.1nW and assuming that the emitted photons are monochromatic with an energy of 3eV corresponding to 420nm and a singlet lifetime of 10ns the singlet concentration would be approximately in the range of 10^6 singlets/cm^3. Thus assuming that the triplet lifetime is three orders of magnitude greater than the singlet lifetime, then we have a triplet concentration of: $10^6 \times 10^3 = 10^9$ triplets/cm^3.

12.2.2 Electron Mobility in the Presence of Excited States

Although we have demonstrated that in the case of NPB and TPD they both possess similar electron and hole mobility, we have not shown how an offset bias can affect their electron mobility. The reason for this is the large energetic barrier between the LUMO of the organic and the work function of the Al electrode, approximately 2eV for each material[94]. Thus injecting into the LUMO of TPD or NPB would require a very large electric potential which would result in device breakdown. One possible solution could be by physically altering the energy levels of the electrodes by selecting conductors that have similar work functions to the LUMO of the organic, for example using calcium as a conductor for both electrodes can be a possibility. Calcium has a work function of 2.9eV[94] and it matches closely that of the LUMO of TPD and NPB. However such an arrangement will most likely lead to very low hole injection thus restricting the number of excited states generated.

Another possible solution that could take into account the effect of offset is a combination of TOF and offset bias as shown in figure 57. Applying first a forward bias will generate the required excited states and at some time $t=t_{V0}>0$ a reverse bias would be applied to provide the required V_0 for the mobility measurement. The laser pulse would then be applied a short time (t_s) after t_{V0} such that $t_{V0} - t_s$ is short enough for any triplet response but at the same time long enough avoid interacting with the RC response of the circuit.

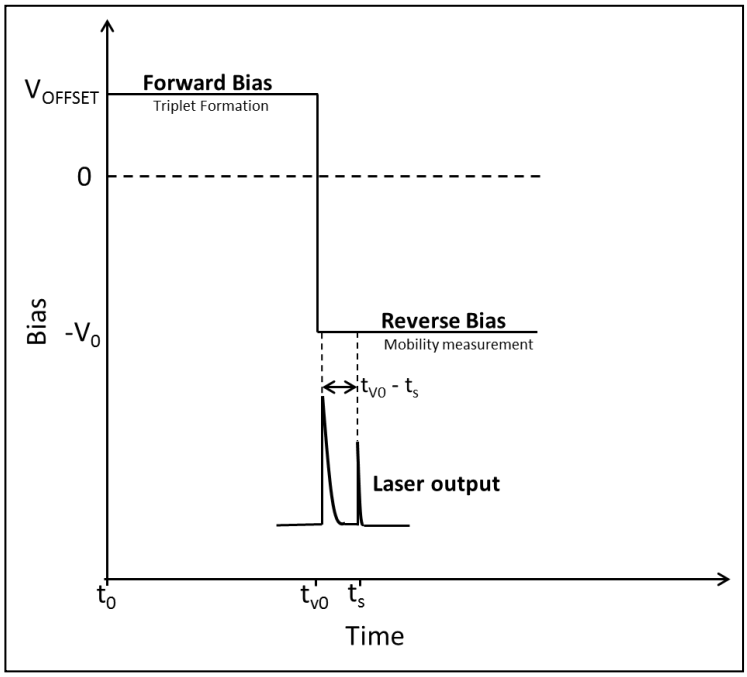

Figure 57. TOF arrangement for measuring electron mobility with offset

Ideally the effects of excited states on electron mobility behaviour should be very similar to holes as they possess similar mobilities. However, as we have also shown, the energetic disorder for electrons and holes are not always identical specially in the case of NPB where we calculated 39meV and 95meV for electrons and holes respectively. This suggests that they experience slightly different transport environments, perhaps they encounter different trap exposures. Thus it would be interesting to see in what shape and form excited states would impact the electron transport behaviour in TPD, NPB and potentially other materials with similar chemical structures.

12.2.3 Analysis of Trap Energies and Distributions

At present very limited work has been carried out in the literature to analyze charge traps in disordered organics. Most of the work in this area is focused on crystalline structures with well-defined lattice constants[94] where charge transport is considered to be ballistic rather than localized hopping behaviours. Reference to energetic traps in disordered organics usually fall into two categories: shallow and deep traps. The distinction between the two is made by analyzing the trap energies and its effect on carrier mobility. It is not unreasonable to say that almost all organic semiconductors would have some degree of traps that would most likely have an effect on the transport properties of the material. This was clearly demonstrated numerically in section 9.4. Thus a comprehensive trap analysis for both the type of traps that are present and also their distribution within the bulk is crucial. This way we can make a direct comparison between the trap energies and their distribution with triplet concentration and carrier drift velocities.

12.2.4 Magnetic Field Effects on Transport Properties of Organics

The presence of magnetic fields can have a profound effect on the excitonic processes within organic devices. This effect has been studied in some detail in recent years, however very little attention has been given to their effect on the transport properties of the carriers under test. In 2010 Song *et al* showed how the hole mobility of an ambipolar TPD device can increase by 10% with an applied 500mT field[52]. They successfully concluded that for

this effect to occur there must be a presence of excited states in the material as delocalized carriers are not susceptible to magnetic field effects. Thus it would be interesting to expand this work further to study the effects of magnetic fields with respect to varying offset bias and temperature. It has been shown that an applied magnetic field can change the spin configuration of triplets resulting in three known excitonic processes, 1), Triplet-Triplet annihilation, 2), Triplet quenching and 3), Intersystem crossing. The presence of any of these effects will have a profound impact on carrier mobility. Thus a comprehensive analysis of magnetic field effects on carrier mobility can provide even further detail on the different types of excitonic behaviours in organic devices.

References

[1] W. Helfrish, W. G. Schneider, Recombination Radiation in Anthracene Crystals*Phys. Rev. Lett.* **1965***,* 14, 229

[2] C. W. Tang, S. A. VanSlyke, Organic electroluminescent diodes, *Appl. Phys. Lett.* **1987,** 51, 913

[3] C. W. Tang, Two-layer organic photovoltaic cell, *Appl. Phys. Lett*. **1986,** 48, 183

[4] J. J. M. Halls, K. Pichler, R. H. Friend, S. C. Moratti, and A. B. Holmes, Exciton diffusion and dissociation in a poly(p-phenylenevinylene)/C_{60} heterojunction photovoltaic cell, *Appl. Phys. Lett*. **1996**, 68, 3120

[5] P. Peumans, A. Yakimov, S. R. Forrest, Small molecular weight organic thin-film photodetectors and solar cells, *J. Appl. Phys.* **2003**, 93, 3693

[6] J. J. M. Halls, C. A. Walsh, N. C. Greenham, E. A. Marseglia, R. H. Friend, S. C. Moratti, A. B. Holmes, Efficient photodiodes from interpenetrating polymer Networks, *Nature* **1995,** 376, 498

[7] C. J. Brabec, N. S. Sariciftci, J. C. Hummelen, Plastic Solar Cells, *Adv. Func. Mater.* **2001**, 11, 15

[8] W. U. Huynh, J. J. Dittmer, A. P. Alivisatos, Hybrid Nanorod-Polymer Solar Cells, *Science,* **2002**, 295, 2425

[9] U. Bach, D. Lupo, P. Comte, J.E. Moser, F. Weissoertel, J. Salbeck, H. Spreitzer, M. Graetzel, Solid-state dye-sensitized mesoporous TiO_2 solar cells with high photon-to-electron conversion efficiencies, *Nature,* **1998,** 395, 583

[10] Christoph Waldauf, Pavel Schilinsky, Jens Hauch, Christoph J. Brabec, *Thin Solid Films*, Production Aspects of Organic Photovoltaics and Their Impact on the Commercialization of Devices, **2004**, 451, 503

[11] G. Horowitz, Organic Field-Effect Transistors, *Adv. Mater.* **1998,** 10, 365

[12] M. Shtein, J. Mapel, J. B. Benziger, S. R. Forrest, Effects of film morphology and gate dielectric surface preparation on the electrical characteristics of organic-vapor-phase-deposited pentacene thin-film transistors, *Appl. Phys. Lett.* **2002,** 81, 268

[13] H. Klauk, M. Halik, U. Zschieschang, G. Schmid, W. Radlik, W. Weberm, High-mobility polymer gate dielectric pentacene thin film transistors, *J. Appl. Phys.* **2002,** 92, 5259

[14] T.Q. Nguyen, R.Y. Yee, B.J. Schwartz, *J.* Photochem. Photobiol. Solution processing of conjugated polymers: the effects of polymer solubility on the

morphology and electronic properties of semiconducting polymer films, *A: Chem.* **2001,** 21, 144

[15] A. J. Campbell, D. D. C. Bradley, J. Laubender, M. Sokolowski, Thermally activated injection limited conduction in single layer N,N′-diphenyl-N,N′-bis(3-methylphenyl)1-1′-biphenyl-4,4′-diamine light emitting diodes, *J. Appl. Phys.***1999**, 86, 5004

[16] M. S. Xue and Q. Guo, Layer-by-layer growth of polar MgO(111) ultrathin films, *J. Chem. Phys*. **2007**, 127, 054705

[17] S. Barth, P. Müller, H. Riel, P.F. Seidler, W. Rieß, H. Vestweber, and H. Bässler Electron mobility in tris(8- hydroxy-quinoline)aluminum thin films determined via transien electroluminescence from single- and multilayer organic light-emitting diodes, *J. Appl. Phys.* **2001**, 89, 3711

[18] M. Pope, C. E. Swenberg, Electronic Processes in Organic Crystals and Polymers, **1999**, *Oxford University Press*,

[19] C.D. Dimitrakopoulos, P.R.L. Malenfant, Organic Thin Film Transistors for Large Area Electronics, *Adv. Mater.* **2002**, 14, 99

[20] S.K. Park, T.N. Jackson, J.E. Anthony, D.A. Mourey, High mobility solution processed 6,13-bis(triisopropyl-silylethynyl) pentacene organic thin film transistors, *Appl. Phys. Lett.* **2007**, 91, 063514

[21] A.R. Murphy, J.M.J. Fréchet, Organic Semiconducting Oligomers for Use in Thin Film Transistors, *Chem. Rev.* **2007**, 107, 1066

[22] M. Morana, M. Wegscheider, A. Bonanni, N. Kopidakis, S. Shaheen, M. Scharber, Z. Zhu, D. Waller, R. Gaudiana, C. Brabec, Bipolar Charge Transport in PCPDTBT-PCBM Bulk-Heterojunctions for Photovoltaic Applications, *Adv. Funct. Mater*. **2008**, 18, 1757

[23] X. Yang, J. Loos, S.C. Veenstra, W.J.H. Verhees, M.M. Wienk, J.M. Kroon, M.A.J. Michels, R.A.J. Janssen, Nanoscale Morphology of High-Performance Polymer Solar Cells, *Nano Lett.*, **2005**, 5, 579,

[24] S. A. Choulis, Y. Kim, J. Nelson, D. D. C. Bradley, M. Giles, M. Shkunov, I. McCulloch, High ambipolar and balanced carrier mobility in regioregular poly(3-hexylthiophene), Appl*. Phys. Lett.* **2004,** 85, 17

[25] S. Barard, M. Heeney, L. Chen, M. Cölle, M. Shkunov, I. McCulloch, N. Stingelin, M Philips, T. Kreouzis, Separate charge transport pathways determined by the time of flight method in bimodal polytriarylamine*, J. Appl. Phys.* **2009**, 105, 013701

[26] T. Kreouzis, D. Poplavskyy, S. M. Tuladhar, M. Campoy-Quiles, J. Nelson, A. J. Campbell, D. D. C. Bradley, Temperature and field dependence of hole mobility in poly(9,9-dioctylfluorene), *Phys. Rev. B.* **2006**, 73, 235201

[27] Y. Kim, S. Cook, S. A. Choulis, J. Nelson, J. R. Durrant, D. D. C. Bradley, Organic Photovoltaic Devices Based on Blends of Regioregular Poly(3-hexylthiophene) and Poly(9,9-dioctylfluorene-co-benzothiadiazole), *Chem. Mater.* **2004**, 16, 4812

[28] Salvatore Gambino, Ashu K. Bansal, D.W. Samuel, Photophysical and charge-transporting properties of the copolymer SuperYellow, *Org. Electron.* **2013**, 18, 1980

[29] V. Coropcea, J. Corneal, D. A. Da Silva Filho, Y. Olvier, R. Silbey, J. L. Bredas, Charge Transport in Organic Semiconductors, *Chem. Rev.* **2007**, 107, 926

[30] T. Sakanoue, H. Sirringhaus, Band-like temperature dependence of mobility in a solution-processed organic semiconductor, *Nat. Mater*. **2010**, 9, 736

[31] K.K. Tsung, S.K. High temperature carrier mobility as an intrinsic transport parameter of an organic semiconductor, So, *Org. Electron.* **2009**, 10, 661

[32] E.A.Sillinsh, V. Capek, Organic Molecular Crystals: Interaction, Localization, and Transport Phenomena, **1994,** AIP, New York

[33] Y.V. Romanovskii, H. Bassler, Phosphorescence from a ladder-type conjugated polymer in solid solutions at low temperature, *Chem. Phys. Lett*. **2000**, 51, 326

[34] Y.V. Romanovskii, A. Gerhard, B. Schweitzer, U. Scherf, R.I. Personov, H. Bässler, Phosphorescence of π-Conjugated Oligomers and Polymers, *Phys. Rev. Lett*. **2000**, 84, 1027

[35] M. A. Baldo, S. Lamansky, P. E. Burrows, M. E. Thompson, S. R. Forrest, Very high-efficiency green organic light-emitting devices based on electrophosphorescence, *Appl. Phys. Lett.* **1999**, 75, 4

[36] M.A. Baldo, D.F. O'Brien, Y. Yu, A. Shoustikov, S. Silbey, M.E. Thompson, S.R. Forrest, Highly efficient phosphorescent emission from organic electroluminescent devices, *Nature.* **1998**, 395, 151

[37] S. Reineke, K. Walzer, and K. Leo, Reduced efficiency roll-off in phosphorescent organic light emitting diodes by suppression of triplet-triplet annihilation, *Phys. Rev. B.* **2007,** 75, 125328

[38] S. Gong, Q. Fu, W. Zeng, C. Zhong, C. Yang, D. Ma and J. Qin, Solution-Processed Double-Silicon-Bridged Oxadiazole/Arylamine Hosts for High-Efficiency Blue Electrophosphorescence, *Chem. Mater.* **2012**, 24, 3120

[39] G. Grem, G. Leditzky, G. Ullrich, B. Leising, Realization of a blue-light-emitting device using poly(p-phenylene), *Adv. Mater.* **1992**, 4, 36

[40] V.L. Colvin, M.C. Schiamp, A.P. Alivisatos, Light-emitting diodes made from cadmium selenide nanocrystals and a semiconducting polymer, *Nature*. **1994**, 370, 354

[41] F. C. Krebs, S. A. Gevorgyan, J. Alstrup, A roll-to-roll process to flexible polymer solar cells: model studies, manufacture and operational stability studies, *J. Mater. Chem*. **2009**, 19, 5442.

[42] J. Kido, K. Hongawa, K. Okuyama, K. Nagai, White light-emitting organic electroluminescent devices using the poly(N-vinylcarbazole) emitter layer doped with three fluorescent dyes, *Appl. Phys. Lett.* **1994**, 64, 815

[43] T.R. Hebner, C.C. Wu, D. Marcy, M.H. Lu, C. Sturm, Ink-jet printing of doped polymers for organic light emitting devices, *Appl. Phys. Lett.* **1998**, 72, 519

[44] T. W. Lee, J. Zaumseil, S. H. Kim, J. W. P. Hsu, Thermally Assisted Sub-10 fs Electron Transfer in Dye-Sensitized Nanocrystalline TiO_2 Solar Cells, *Adv. Mater.* **2004**, 16, 2040

[45] Y. Athanassov, F. P. Rotzinger, P. Péchy, M. Graetzel, Sensitized Electroluminescence on Mesoporous Oxide Semiconductor Films, *J. Phys. Chem*. B. **1997**, 101, 2558

[46] Z. Zhang, Z. Deng, C. Liang, M. Zhang, D. Xu, Organic light-emitting diodes with a nanostructured TiO2 layer at the interface between ITO and NPB layers, *Displays* **2003**, 24, 231

[47] Y.S. Yao, Q.X. Zhou, X.S. Wang, Y. Wang, B.W. Zhang, Fine tuning of the photophysical and electroluminescent properties of DCM-type dyes by changing the structure of the electron-donating group, *J. Mater. Chem.* **2006,** 16, 3512

[48] M. Cocchi, D. Virgili, V. Fattori, D.L. Rochester, J.A.G. Williams, N∧C∧N-Coordinated Platinum(II) Complexes as Phosphorescent Emitters in High-Performance Organic Light-Emitting Devices, *Adv. Funct. Mater.* **2007**, 17, 285.

[49] J. Luo, Y. Zhou, Z.-Q. Niu, Q.-F. Zhou, Y. Ma, J. Pei, Three-Dimensional Architectures for Highly Stable Pure Blue Emission, *J. Am. Chem. Soc.*129 **2007**, 129, 11314.

[50] Ern, Merrifield, Theory of Magnetic Field Effects on the Mutual Annihilation of Triplet Excitons *PRL*, **1968**, 21, 609

[51] P. Desai, P. Shakya, T. Kreouzis, W. P. Gillin, Magnetoresistance in organic light-emitting diode structures under illumination, *Phys. Rev. B.* **2007,** 76, 235202

[52] J. Y. Song, N. Stingelin, W. P. Gillin, T. Kreouzis, Reduced hole mobility due to the presence of excited states in poly-(3-hexylthiophene), *Appl. Phys. Lett*. **2008**, 93, 233306

[53] R. G. Kepler, Charge Carrier Production and Mobility in Anthracene Crystals, *Phys. Rev.* **1960**, 119, 1226

[54] O. H. Leblanc, Hole and Electron Drift Mobilities in Anthracene, *J. Chem. Phys*. **1960**, 33, 626

[55] H. Bässler, H. Rost, H. H. Horhold, H. Bässler, H. Rost, H. H. Horhold, J. Chem. Phys. 2000, 113, 3802, *J. Chem. Phys.* **2000**, 113, 3802

[56] W.E. Spear, Drift mobility techniques for the study of electrical transport properties in insulating solids, *J. Non-Cryst. Solids 1*. **1969**, 197

[57] S.H. Kang, T. Crisp, I. Kymissis, V. Bulovic, Memory effect from charge trapping in layered organic structures, *Appl. Phys. Lett*. **2004,** 85, 4666

[58] G.G. Malliaras, Y. Shen, D.H. Dunlap, H. Murata, Z.H. Kafafi, Nondispersive electron transport in Alq_3, *Appl. Phys. Lett.* **2001**, 79, 2582

[59] P.M. Borsenberger and D.S. Weiss, M. Dekker, Organic Photoreceptors for Xerography, **1998**, New York

[60] S. Karg, J. Steiger, H. von Seggern, Determination of trap energies in Alq_3 and TPD, *Synth. Met.* **2000**, 111, 277

[61] A. G. Werner, J. Blochwitz, M. Pfeiffer, K. Leo, Field dependence of thermally stimulated currents in Alq_3, *J. Appl. Phys*. **2001**, 90, 123

[62] B. Mollay, U. Lemmer, R. Kersting, R. F. Mahrt, H. Kurz, H. F. Kauffmann, H. Bässler*,* Dynamics of singlet excitations in conjugated polymers: Poly(phenylenevinylene) and poly(phenylphenylenevinylene), *Phys. Rev. B.* **1994**, 50, 10769

[63] G. R. Hayes, I. D. W. Samuel, R. T. Phillips, Polarization dependence of the ultrafast photoluminescence of oriented poly(p-phenylenevinylene), *Phys. Rev. B* **1997**, 56, 3838

[64] H. Scher, E.W. Montroll, Anomalous transit-time dispersion in amorphous solids *Phys. Rev. B.* **1975,** 12, 2455

[65] D. Poplavskyy, J. Nelson, Nondispersive hole transport in amorphous films of methoxy-spirofluorene-arylamine organic compound, *J. Appl. Phys***. 2003**, 93, 341

[66] M. A. Lampert, P. Mark, Current Injection in Solids, *Academic Press*, **1970**, New York

[67] G. Horowitz, Semiconducting Polymers. (eds.: G. Hadziioannou, G. G. Malliaras), **2007**, Wiley-VCH, Weinheim

[68] A.F. Stassen, I.W.R. de Boer, N.N. Iosad, A.F. Morpurgo, Influence of the gate dielectric on the mobility of rubrene single-crystal field-effect transistors, *Appl. Phys. Lett.* **2004**, 85, 3899

[69] H. Bässler, Charge Transport in Disordered Organic Photoconductors a Monte Carlo Simulation, Study *Phys. Status. Solidi. B.* **1993**, 15, 175

[70] D. Hertel, H. Bässler, Photoconduction in Amorphous Organic Solids, *ChemPhysChem*. **2008**, 9, 666

[71] H.H. Fong, K.C. Lun, S.K. Extrinsic Electron Traps in Tris(8-hydroxyquinoline) Aluminium, So, *Chem. Phys. Lett*. **2002**, 353, 407

[72] H. H. Fong, K. Lun, S. So, Jpn. Hole transports in molecularly doped triphenylamine derivative*, J. Appl. Phys.* **2002**, 41, 1122

[73] A. Miller, E. Abrahams, Impurity Conduction at Low Concentrations, *Phys. Rev.* **1960**, 120, 745

[74] I. I. Fishchuk, A. K. Kadashchuk, J. Genoe, Mujeeb Ullah, H. Sitter, Th. B. Singh, N. S. Sariciftci, H. Bässler, Electric field dependence of charge-carrier hopping transport within the random energy landscape in an organic field effect transistor, *Phys. Rev. B*. **2010**, 81, 045202

[75] L. J. A. Koster, Charge carrier mobility in disordered organic blends for Photovoltaics, *Phys. Rev. B*. **2010,** 81, 205318

[76] K. K. Tsung, S. K. So, High temperature carrier mobility as an intrinsic transport parameter of an organic semiconductor, *Org. Electron*. **2009**, 10, 661

[77] S. Raj Mohan, M. P. Joshi, M. P. Singh, Charge transport in disordered organic solids: A Monte Carlo Simulation*Org. Electron.* **2008**, 9, 355

[78] T. Holstein, Studies of polaron motion: Part I. The molecular-crystal model *Ann. Phys.* **1959**, *8*, 325

[79] T. Holstein, Studies of polaron motion: Part II. The “small” polaron, *Ann. Phys.* **1959**, *8*, 343

[80] H. Bässler, P. M. Borsenberger, R. J. Perry, Charge transport in poly(methylphenylsilane): The case for superimposed disorder and polaron effects*J. Polym. Sci. Part B.* **1994**, 32, 1677

[81] I. I. Fishchuk A. Kadashchuk, H. Bässler, S. Nespurek, Nondispersive polaron transport in disordered organic solids, *Phys. Rev. B.* **2003**, 67, 224303

[82] D. Emin. Phonon-assisted transition rates I. Optical-phonon-assisted hopping in solids, *Adv. Phys.* **1975**, *24*, 305

[83] Y. N. Gartstein, E. M. Conwell, High-field hopping mobility in molecular systems with spatially correlated energetic disorder, *Chem. Phys. Lett.* **1995,** 245, 351

[84] D. H. Dunlap, P. E. Parris, V. M. Kenkre, Charge-Dipole Model for the Universal Field Dependence of Mobilities in Molecularly Doped Polymers, *Phys. Rev. Lett.* **1996**, 77, 542

[85] B. Movaghar, M. Grünewald, B. Ries, H. Bässler, D. Würtz, Diffusion and relaxation of energy in disordered organic and inorganic materials, *Phys. Rev.* **1986**, 33, 5545

[86] Z. G. Yu, D. L. Smith, A. Saxena, R. L. Martin, A. R. Bishop, Molecular Geometry Fluctuation Model for the Mobility of Conjugated Polymers, *Phys. Rev.*

Lett. **2000**, 84, 721

[87] Z. G. Yu, D. L. Smith, A. Saxena, R. L. Martin, A. R. Bishop, Molecular geometry fluctuations and field-dependent mobility in conjugated polymers, *Phys. Rev. B.* **2001,** 63, 085202

[88] M. Ikai, S. Tokito, Y. Sakamoto, T. Suzuki, Y. Taga, Highly efficient phosphorescence from organic light-emitting devices with an exciton-block layer, *Appl. Phys. Lett.* **2001,** 79,156

[89] Z. Bao, A.J. Lovinger, A. Dodabalapur, Soluble and processable regioregular poly(3-hexylthiophene) for thin film field-effect transistor applications with high mobility, *Appl. Phys. Lett.* **1996,** 69, 3066

[90] H. E. Katz, Z. Bao, The Physical Chemistry of Organic Field-Effect Transistors, *J. Phys. Chem. B.* **2000,** 104, 671

[91] T. D. Anthopoulos, C. Tanase, S. Setayesh, E. J. Meijer, J. C. Hummelen, P. W. M. Blom, D. M. de Leeuw, Ambipolar Organic Field-Effect Transistors Based on a Solution-Processed Methanofullerene, *Adv. Mater.* **2004**, 16, 2174

[92] J. Zaumseil, R. H.Friend, H. Sirringhaus, Spatial control of the recombination zone in an ambipolar light-emitting organic transistor, *Nat. Mater.* **2006**, 5, 69

[93] V.M. Agranovich, D.M. Basko, K. Schmidt, G.C. LaRocca, F. Bassani, S. Forrest, K. Leo, D. Lidzey, Charged Frenkel excitons in organic crystals, *Chem. Phys.* **2001**, 272, 159

[94] So. Frankly, Organic Electronic: Materials, Processing, Devices and Applications, 1st ed, USA, CRC Press, **2010**